

THE UNIVERSITY OF CHICAGO

SPATIOTEMPORAL CHARACTERIZATION OF NEURAL NETWORK ACTIVITY

A DISSERTATION SUBMITTED TO
THE FACULTY OF THE DIVISION OF THE BIOLOGICAL SCIENCES
AND THE PRITZKER SCHOOL OF MEDICINE
IN CANDIDACY FOR THE DEGREE OF
DOCTOR OF PHILOSOPHY

INTERDISCIPLINARY SCIENTIST TRAINING PROGRAM:
NEUROBIOLOGY

BY
SARITA SRISAI DESHPANDE

CHICAGO, ILLINOIS

AUGUST 2023

To my parents

“Every science begins as philosophy and ends as art: it arises in hypothesis and flows into achievement. “

-William James Durant, The Story of Philosophy (1926)

TABLE OF CONTENTS

LIST OF FIGURES	viii
LIST OF TABLES	ix
ACKNOWLEDGEMENTS	x
ABSTRACT.....	xi
CHAPTER 1: INTRODUCTION.....	1
1.1 Clinical Aspects of Epilepsy	1
1.1.1 Diagnosis	1
1.1.2 Anti-seizure medications and drug resistance	2
1.1.3 Surgical resection	3
1.1.4 Psychiatric comorbidities and epilepsy-related structural changes	5
1.1.5 Seizure classification	6
1.2 Multiscale Recording Modalities.....	7
1.3 Excitation and Inhibition Imbalance	9
1.4 Computational Models in Epilepsy Research	12
1.4.1 Cellular models	12
1.4.2 Population-scale models	14
1.5 Overview of Dissertation	14
CHAPTER 2: SPATIOTEMPORAL SPIKE-CENTERED AVERAGING REVEALS SYMMETRY OF TEMPORAL AND SPATIAL COMPONENTS OF THE SPIKE-LFP RELATIONSHIP DURING HUMAN FOCAL SEIZURES	16
2.1 Summary	16
2.2 Introduction	17
2.3 Results	19
2.3.1 Theoretical model of the spike-LFP relationship	19
2.3.2 Characterization of the spike-LFP relationship in microelectrode arrays.....	21
2.3.3 Application of st-SCA to clinical microelectrode array recordings	23
2.3.4 Visualization of spatial and temporal components of the spike-LFP relationship	26
2.3.5 Quantification of the peak-to-peak distance of spatial patterns	30
2.4 Discussion	33
2.5 Methods.....	38
2.5.1 Patients	38
2.5.2 Signal acquisition and pre-processing	38
2.5.3 st-SCA calculations and signal analysis	39
2.5.4 Spatial filtering	40
2.5.5 Statistics and reproducibility.....	41
2.6 Supplementary Materials	42

2.6.1	The sine cardinal (sinc) function	42
2.6.2	The st-SCA as a unit impulse response	43
2.6.3	Mechanisms involved in focal seizures	45
2.6.4	Supplemental figures and tables	46
CHAPTER 3: THIRD-ORDER MOTIFS ARE SUFFICIENT TO FULLY AND UNIQUELY CHARACTERIZE SPATIOTEMPORAL NEURAL NETWORK ACTIVITY.....		55
3.1	Summary	55
3.2	Introduction	56
3.3	Methods.....	57
3.3.1	Defining triple correlation.....	57
3.3.2	Overview of uniqueness proof.....	59
3.3.3	Summarizing triple correlation with motif classes	59
3.3.4	Controlling for expected contributions.....	60
3.4	Results	61
3.4.1	Application of triple correlation summary	62
3.4.2	Resistance to noise	64
3.4.3	Detecting various spike sequences.....	67
3.4.4	Application to experimental data	69
3.5	Discussion.....	73
CHAPTER 4: INSIGHTS INTO NEURAL NETWORK BEHAVIOR USING 4D ENTROPY: A NOVEL QUANTITATIVE METRIC OF NETWORK ACTIVITY BASED ON TRIPLE CORRELATION.....		78
4.1	Summary	78
4.2	Introduction	79
4.2.1	Methods to characterize neural networks.....	79
4.2.2	Overview of triple correlation approach.....	82
4.3	Methods.....	83
4.3.1	Estimating 4D PDF and computing the 4D entropy	83
4.4	Results	86
4.4.1	Rat cortical cultures: 4D entropy and motif-class spectrum over time	86
4.5	Discussion.....	88
4.5.1	Overview	88
4.5.2	Limitations and future directions	89
CHAPTER 5: MODELING AND CHARACTERIZING EXCITATORY-INHIBITORY NETWORK ACTIVITY DURING HUMAN FOCAL SEIZURES.....		92
5.1	Summary	92
5.2	Introduction	93

5.2.1	Regular-spiking and fast-spiking cell types	93
5.2.2	Overview of spike sorting	94
5.2.3	Defining the phases of the ictal period	95
5.2.4	Overview of triple correlation.....	98
5.3	Methods.....	99
5.3.1	Hodgkin-Huxley formalism	99
5.3.2	Modeling synaptic conductance	100
5.4	Results	101
5.4.1	Stages A-B: Modeling E-I network activity during ictal pre-recruitment	101
5.4.2	Stage C: Simulating excitatory network activity during ictal recruitment	108
5.5	Discussion	110
5.5.1	Overview	110
5.5.2	Limitations and future directions	110
CHAPTER 6: CONCLUSIONS.....		113
6.1	Translational Implications and Future Directions	115
REFERENCES		118
APPENDIX		135
A.1	Application of Triple Correlation to MEA Spiking Activity	135
A.1.1	Rhesus macaque completing an instructed, reach-to-grasp task	135
A.2	Supplemental Materials for Triple Correlation.....	136
A.2.1	Uniqueness of triple correlation for network spiking activity	136
A.2.2	Proof of Theorem 1 (two dimensions)	139
A.2.3	Proof of Theorem 2 (N dimensions)	141
A.2.4	Computing the triple correlation.....	143
A.2.5	Summarizing triple correlation into motif classes.....	145
A.2.6	The number of lag-sign motifs.....	146
A.2.7	The number of motif classes	148
A.2.8	Expected contributions per motif class.....	150
A.2.9	Independent spiking with constant probability (Bernoulli)	152
A.2.10	The number of triplet motifs	152

LIST OF FIGURES

Figure 1.1	Schematics of multi-scale recording modalities, recruited and unrecruited territories, and paroxysmal depolarizing shift	11
Figure 2.1	Mathematical model of the spike-LFP relationship	21
Figure 2.2	Method to compute st-SCA	25
Figure 2.3	STAs in recruited & unrecruited seizure territories.....	29
Figure 2.4	Examples of the st-SCA computation for two patients	30
Figure 2.5	Method to compute 2D st-SCA	32
Figure 2.6	Summary of key findings and clinical/biological implications	36
Figure 2.7	Simulated 1D and 2D sinc functions	43
Figure 2.8	Representative st-SCAs for each patient	46
Figure 2.9	Spatial component of the st-SCAs.....	47
Figure 2.10	Noise estimates of the st-SCA	48
Figure 2.11	STAs based on LFP from recruited & unrecruited territories	49
Figure 2.12	Representative st-SCAs after randomizing spike triggers	50
Figure 2.13	Representative st-SCAs after spatial filtering	51
Figure 3.1	Application of the fourteen motif classes to spike rasters	58
Figure 3.2	Motif-class contributions to the raster's triple correlation	64
Figure 3.3	Detecting synchrony amidst increasing noise	66
Figure 3.4	Detecting motif classes in individual patterns	68
Figure 3.5	Application of triple correlation to rat cultures	72
Figure 3.6	Representative 1-min epochs of rat cortical spike rasters	73
Figure 4.1	The fourteen motif classes from triple correlation	83
Figure 4.2	Overview of method to compute PDF and entropy	85
Figure 4.3	Characterizing network activity of rat cortical cultures over time	87
Figure 4.4	The motif-class spectrum for rat cortical neurons over time.....	88
Figure 5.1	Defining the phases of the ictal period	97
Figure 5.2	The fourteen motif classes generated from triple correlation	98
Figure 5.3	Model of the ictal pre-recruitment period corroborates clinical patterns	103
Figure 5.4	Quantitative network comparison using triple correlation	105
Figure 5.5	Cross-correlation of the phase angle ratios using Hilbert transform	106
Figure 5.6	Effects of adjusting the cross-synaptic weights.....	107
Figure 5.7	Model of the ictal recruitment period	109
Figure A.1	Triple correlation applied to monkey spike data	136

LIST OF TABLES

Table 2.1	Patient table: demographics and clinical features	52
Table 2.2	Patient table: seizure recording and spike detection information	53
Table 2.3	st-SCA contributions per each position for Patient 1	54
Table 2.4	SNR values per each position for Patient 1	54
Table 5.1	Cellular parameters for Hodgkin-Huxley model.....	100
Table 5.2	Gating equations for resonator and integrator classes.....	100
Table A.1	Counting the number of lag-sign motifs per motif class.....	148
Table A.2	The 169 possible lag-sign motifs	156

ACKNOWLEDGEMENTS

I am truly grateful for the support, guidance, and mentorship I have received over the course of this degree. Thank you, thank you, thank you to my PI, Professor Wim van Drongelen, PhD for providing me with this wonderful opportunity to complete my PhD in his lab. From learning to question everything to honing my inquiry and analysis skills, I now think critically about my own and others' science. Thank you, Wim, for your dedication in teaching me to become a scientist.

Thank you to my thesis committee members for their support and guidance: Nicho Natsopoulos, PhD, Naoum Issa, MD, PhD, Dan McGehee, PhD, and V. Leo Towle, PhD. I would also like to thank all of the lab members for their support as well as our collaborators: the Schevon lab at Columbia University in New York and the van Putten lab at the University of Twente, Netherlands. I am also incredibly grateful to the MSTP administration (Marcus Clark, MD, Alison Anastasio, PhD, Stephen Meredith, MD, PhD, Marisa Davis, and Allicia Washington-White) and the Neuroscience Department (Elena Rizzo & Lili Gonzalez Hernandez) for their continued support. Furthermore, I am so thankful to all my academic and research mentors that have inspired me to embark on this journey to become a physician-scientist: Sriram Sonty, MD, Kornel Schuebel, PhD, and Keith Martin, MD.

To my family, words do not suffice. Thank you to my parents, Rajender and Sarada, my first teachers who continually inspire me to become the best version of myself in this pursuit of knowledge as well as lifelong learning and service. Thank you to my siblings, Rajiv and Meena, for being my best friends, and thank you to my husband, Surya, for being a wonderful partner. Their unwavering support and love in all my endeavors have been my rock throughout each phase of my education, and I wholeheartedly dedicate my successes to them.

ABSTRACT

Uncovering information hidden within brain networks can be a daunting task, especially in the cases of abnormal, disrupted neural networks, such as epilepsy. Here, I present a multifaceted approach that combines signal processing, computational neuroscience, and theoretical and mathematical modeling to investigate the mechanisms and structure that underlie neuronal activity in both time and space. First, I show that there is a mathematical symmetry in the temporal and spatial domains if the spike-centered averages (a novel second-order metric of the action potential spike-LFP relationship) resemble sinc functions in human focal seizures. I then advance network analysis by presenting a novel approach to characterize neural networks using third-order motifs, which are sufficient to completely and uniquely characterize networks in both time and space. Furthermore, these third-order motifs are classified according to their sequencing depending on the combination of up to two lags in time and space, yielding fourteen qualitatively distinct motif classes that can embody well-studied neural network properties, such as synchrony, feedback, divergence, and convergence. Building from triple correlation, I then develop a novel quantitative metric that captures overall network activity: the 4D entropy based on the spatiotemporal lag distribution computed from triple correlation. Applying this metric to rat cortical cultures from microelectrode arrays, I demonstrate the enhanced value of 4D entropy, which is based on third-order structure, in that it captures the underlying dynamics in comparison to 2D, or pairwise, entropy. Lastly, I develop and implement a Hodgkin-Huxley simulation of excitatory-inhibitory population activity to model the first three stages of a focal seizure and use triple correlation to show that the network represented by the model is a good fit for the network of the patient data.

CHAPTER 1

INTRODUCTION

Epilepsy is a neurological disorder characterized by recurrent, spontaneous seizures. Between 1-2% of people are diagnosed with epilepsy in the US, and approximately 65 million people are diagnosed worldwide (Fiest *et al.*, 2017). The word “epilepsy” is derived from the Greek word *epilambanein*, which means “to be seized” (Cule, 1973; Patel & Moshe, 2020), and the word “seizure” is derived from the Latin word *sacire*, meaning “to take possession of” (Bromfield *et al.*, 2006). Even though these terms have been around for many centuries, defining and diagnosing epilepsy is not a trivial task. This can be attributed to the fact that epilepsy constitutes a multitude of disorders, each with varied combinations of symptoms, causes, prognoses, and treatments. While each epileptic pathology offers a plethora of intriguing research questions to study, the work presented in this dissertation mainly focuses on evaluating the spatiotemporal characteristics and mechanisms underlying human focal seizures by utilizing novel computational neuroscience and signal processing tools.

1.1 Clinical Aspects of Epilepsy

1.1.1 Diagnosis

Diagnosing epilepsy is not a straightforward task, as epilepsy is a complex and multifaceted disorder. Detailed medical and family history is crucial, and a clinical epileptologist will determine whether the seizure is epileptic or not, based on signs, symptoms, and presentation (Thijs *et al.*, 2019). To diagnose epilepsy and identify seizure type, neurologists analyze electroencephalogram (EEG) signals for epileptic activity, such as interictal events, electrographic seizures, and background abnormalities. However, misdiagnosis of epilepsy by using EEG can occur. In these cases, clinicians may over-read or misinterpret normal

background fluctuations as abnormal rhythms in EEG (Ferrie, 2006). Furthermore, between 25 to 30% of patients who were administered a first-line anti-epileptic medication do not actually have epilepsy (Amin & Benbadis, 2019). This highlights the importance of diagnostic guidelines. The diagnostic conditions of epilepsy as defined by the ILAE include the following (repeated below from Fisher *et al.*, 2014):

- (1) “At least two unprovoked (or reflex) seizures occurring >24 hr apart
- (2) One unprovoked (or reflex) seizure and a probability of further seizures similar to the general recurrence risk (at least 60%) after two unprovoked seizures, occurring over the next 10 years
- (3) Diagnosis of an epilepsy syndrome”

An unprovoked seizure is one that does not have a temporary or reversible cause (Fisher *et al.*, 2014). Thus, “provoked” seizures, such as those caused by hypoglycemia, hypoxia, infection, injury, drugs/medications, hypertension, alcohol withdrawal, among others (Huff & Murr, 2022), would not be diagnosed as epilepsy (Fisher *et al.*, 2014).

1.1.2 Anti-seizure medications and drug resistance

For most patients with epilepsy, anti-seizure medications (ASMs) are the first-line options. Most ASMs primarily either target sodium channels with an overall goal of reducing the excitability of the neuron or increase GABA transmission with an overall goal of increasing neuronal inhibition (Davies, 1995). These include phenytoin, carbamazepine, valproate, oxcarbazepine, among others (Czapinski et al, 2005). While ASMs tend to be efficacious in reducing seizure burden, approximately 1/3rd of epilepsy patients does not respond to these drugs, which is called pharmacoresistant or drug-resistant epilepsy (DRE) (Fattorusso *et al.*,

2021). While the mechanisms that lead to DRE are not well-established, DRE is thought to be caused by multiple mechanisms acting in congruence. Some of these mechanisms include:

- (1) Transporter hypothesis: The increased expression of specific transporters (e.g. ATP-binding cassette transporters) and P-glycoprotein at the blood brain barrier reduces the effectiveness of ASMs, and thus, leads to DRE (Tang et al., 2017; Fattorusso et al., 2021; Czornyj et al., 2022)
- (2) Pharmacokinetic hypothesis: The increased expression of these transporters in peripheral organs (e.g. colon, liver, and kidney) takes up the ASM in plasma, and thus decreasing the amount of ASM to reach the brain (Tang et al., 2017; Fattorusso et al., 2021; Czornyj et al., 2022).
- (3) Target hypothesis: The structure or function of the molecular targets of ASMs becomes altered, and thus reduces the efficacy of the ASMs (Remy & Beck, 2006). For example, during prolonged status epilepticus, patients can develop resistance to benzodiazepines due to GABA_A receptor internalization at the postsynaptic terminal (Goodkin et al., 2007; Wasterlain & Chen, 2008; Rogawski 2013).

Researchers continue to investigate these hypotheses, the causes of drug resistance in epilepsy, and the development of novel treatments that compensate for these proposed mechanisms of drug resistance.

1.1.3 Surgical resection

For patients with pharmacoresistant focal epilepsy, surgical resection may be a treatment option. Patients first undergo presurgical evaluation to determine if surgical resection would be appropriate and effective. This involves the following steps: (1) identify potential surgical candidates who would benefit from presurgical evaluation, and (2) determine whether surgery

outweighs the potential risks for the surgical candidate (Ryvlin & Rheims, 2008). For the first step, there are three criteria that must be considered: (a) the patient must provide informed consent (the patient understands the goal of presurgical evaluation and surgical treatment); (b) the patient must have pharmacoresistant epilepsy that impacts the social and familial aspects of the patient's life; and (c) imaging and clinical data should indicate that surgical resection could reduce seizure burden (Ryvlin & Rheims, 2008).

The goal of presurgical evaluation is to identify the seizure onset zone (SOZ), which is the region of the brain from which the seizures originate (Ryvlin & Rheims, 2008). The SOZ is utilized as a potential surrogate for the epileptogenic zone (EZ), which is a theoretical construct (as there is no method for direct measurement) and is defined as the minimum brain area that should be resected for the patient to achieve seizure freedom (Luders *et al.*, 1993; Ryvlin & Rheims, 2008). In addition, several other cortical zones have been previously described: the *irritative zone* generates interictal spikes; the *symptomatogenic zone* generates the initial signs and symptoms of a seizure; and the *functional deficit zone* is the brain area that does not function correctly during the interictal period (Ryvlin & Rheims, 2008; Jayakar *et al.*, 2018; Jehi, 2018). These cortical zones can be described independently or may overlap with the EZ and with each other, and thus, are not necessarily mutually exclusive.

After the patient is deemed a good candidate during presurgical evaluation, the next step is to identify the SOZ (Ryvlin & Rheims, 2008). Precise localization of the SOZ is critical to provide an opportunity for surgical resection to be effective (Ryvlin & Rheims, 2008). This is performed using monitoring modalities, such as EEG, stereo-EEG, or intracranial EEG (for more details regarding these recording techniques, refer to Section 1.3 – Multiscale Recording Modalities) (Ryvlin & Rheims, 2008). In addition, identifying the SOZ with high spatial

resolution becomes especially critical if the seizures are thought to originate from brain regions near eloquent cortex regions, which are brain areas responsible for language, motor control, cognition, memory, and sensory perception (Kahn *et al.*, 2017). If the putative SOZ is identified and is outside of eloquent cortex, an interdisciplinary team of neurologists, neurosurgeons, clinical neurophysiologists, radiologists, among others work to develop a surgical plan. Surgical resection involves cutting out the brain tissue responsible for causing the seizures and minimizing the damage to surrounding healthy tissue (Ryvlin & Rheims, 2008). After the surgery is complete, the clinical team will closely monitor the patient in the Epilepsy Monitoring Unit and follow-up to assess the patient's progress, whether the patient needs additional medication, and whether the patient has achieved seizure freedom (Ryvlin & Rheims, 2008).

1.1.4 Psychiatric comorbidities and epilepsy-related structural changes

An epilepsy diagnosis can significantly affect the quality of life physically, socially, and psychologically, including effects on driving, independent living, and work opportunities (Hermann & Seidenberg, 2007). Furthermore, progressive damage from epilepsy can lead to neurocognitive impairment, memory difficulties, and attention deficits (Hermann & Seidenberg, 2007). Because epilepsy results in pathological neural networks that are characterized by disrupted neuronal communication (Bromfield, 2006), it can eventually lead to reorganization of neural circuits (Eyo *et al.*, 2017). Due to this, patients can experience psychiatric and mood disorders in conjunction with epilepsy (Jenson, 2011; Salpekar, 2016). The prevalence of psychiatric comorbidities (of which depression and anxiety are the most frequent) in patients with epilepsy ranges from 25-50%, which is much higher than that of the general population (LaFrance *et al.*, 2008; Hellwig *et al.*, 2012; Salpekar, 2016). Several potential etiologies link depression to epilepsy, such as psychological, familial, and social stressors associated with an

epilepsy disorder. In addition, anti-seizure medications, such as phenobarbital, have been linked to causing depressive symptoms (Vining, 1986; Brent *et al.*, 1990). This can be attributed to increased overall inhibitory transmission and decreased excitatory activity. Furthermore, several studies have noted changes in anatomical structures within the temporal lobe for patients with both epilepsy and depression. Specifically, a structurally smaller hippocampus and a larger amygdala have been identified using neuroimaging techniques in these subset of patients (van Elst *et al.*, 2001; Kanner, 2004; Briellman *et al.*, 2007; Shamim *et al.*, 2009; Taylor *et al.*, 2015). This currently remains an active area of research in identifying structural changes in neuronal circuitry due to epilepsy.

1.1.5 Seizure classification

The International League Against Epilepsy (ILAE) has continually made efforts to refine the classification of different types of epilepsy. Current guidelines involve a multi-level classification of (I) seizure type (focal onset, generalized onset, and unknown onset), (II) epilepsy type (focal, generalized, combined generalized and focal, and unknown), and (III) epilepsy syndrome (Scheffer *et al.*, 2017). *Seizure type* refers to the characteristics of the seizure. The two most described seizure types amongst adults are generalized and focal (partial) seizures. Generalized seizures occur bilaterally across the brain and can be further subdivided into primary and secondary. Focal seizures begin in a distinct cortical region, can spread across the brain, and can progress into secondary generalized seizures (Scheffer *et al.*, 2017). These seizures can be further sub-divided into focal aware (does not involve loss of consciousness) and focal impaired awareness (involves the loss of consciousness) (Thijs *et al.*, 2019). The four *epilepsy types* include focal, generalized, combined generalized & focal, and unknown, and can be determined after the patient has an epilepsy diagnosis (Scheffer *et al.*, 2017). *Epilepsy syndrome* accounts for

the seizure type and epilepsy type and refers to the overall characteristics of the disorder (Scheffer *et al.*, 2017). While there are a multitude of epilepsy syndromes (e.g., Dravet syndrome, infantile spasms, Doose syndrome (Berg *et al.*, 2010)), the work presented in this dissertation focuses on uncovering spatiotemporal relationships and mechanisms in pharmacoresistant focal epilepsy.

1.2 Multiscale Recording Modalities

Investigating epileptic seizure dynamics can involve multiple scales: microscale (μm), mesoscale (mm), and macroscale (cm). For these reasons, various recording modalities and the locations of placement for these recording modalities will capture underlying neural activities at these scales, such as electroencephalogram (EEG), electrocorticogram (ECoG), and microelectrode arrays (MEA), among others (Fig. 1.1A). One of the most important recording and diagnostic tools for epilepsy is the electroencephalogram (EEG). EEG has significantly advanced contributions to investigate epileptiform mechanisms. Briefly, Richard Caton, an English scientist, first utilized galvanometers to measure electrical potentials in animals in 1875. This has since sparked subsequent discoveries in the field of neuroscience. Hans Berger, a German psychiatrist, published his seminal work on discovering the EEG in 1929 (Berger, 1929). The EEG has since been extensively used to describe seizure dynamics (Gibbs & Gibbs, 1952; Penfield & Jasper, 1954; Fisher *et al.*, 2005; Fisher *et al.*, 2014). The fundamental principle underlying EEG is differential amplification: measuring the change in voltage between two pairs of electrodes (Britton *et al.*, 2016). Large groups of neurons firing together leads to the generation of electrical currents, which are detected by EEG electrodes placed on the scalp, typically using the standardized 10-20 placement system (Britton *et al.*, 2016). In epilepsy, different types of EEG recording modalities are utilized. Some examples include: (1) scalp EEG

is the most commonly utilized noninvasive method in which electrodes are placed on the scalp (Berger 1929; Haider *et al.*, 2008); (2) stereo-EEG involves the placement of intracranial electrodes into specific brain regions and is often used to facilitate identification of the seizure onset zone (Isnard, 2004); and (3) intracranial EEG involves the placement of depth electrodes into specific brain regions (Spencer, 2002). Electrocorticogram (ECoG) is an additional invasive recording modality in which grids or strips of ECoG electrodes are placed directly on the surface of the brain for monitoring (Bernabei *et al.*, 2021). These intracranial EEG methods and ECoG electrodes offer increased spatial resolution, which may facilitate identification of the seizure onset zone and eloquent cortex. For detection of activity at the single-neuron scale, microelectrode arrays (MEAs) can be utilized. Utah arrays, a type of MEA, are a 4 mm x 4 mm, 96-channel, 10x10 grid of electrodes placed onto the putative seizure onset zone. Implantation of Utah arrays for temporal lobe epilepsy patients have significantly increased our understanding of single-neuron dynamics on the millimeter-scale, including identification of seizure sub-territories (Schevon *et al.*, 2012; Weiss *et al.*, 2013), neuronal waveform changes due to recruitment (Merricks *et al.*, 2015; Merricks *et al.*, 2021), characterization of the spatiotemporal dynamics of the action potential spike-LFP relationship (Lee *et al.*, 2023), and cell-type interactions both within the millimeter scale (unpublished results, Chapter 5) and across scales (Eissa *et al.*, 2017). Previous studies have used the terms “recruited territory” and “unrecruited territory” to describe two types of seizure sub-territories¹ (Schevon *et al.*, 2012; Weiss *et al.*, 2013; Merricks *et al.*, 2015; Merricks *et al.*, 2021; Lee *et al.*, 2023). The recruited territory is characterized by high

¹The terms “core” and “penumbra” were initially used to describe the two seizure sub-territories (Schevon *et al.*, 2012; Weiss *et al.*, 2013), but “recruited territory” and “unrecruited territory” have since been utilized to account for the dynamic nature of these sub-territories (Merricks *et al.*, 2015; Merricks *et al.*, 2021; Lee *et al.*, 2023).

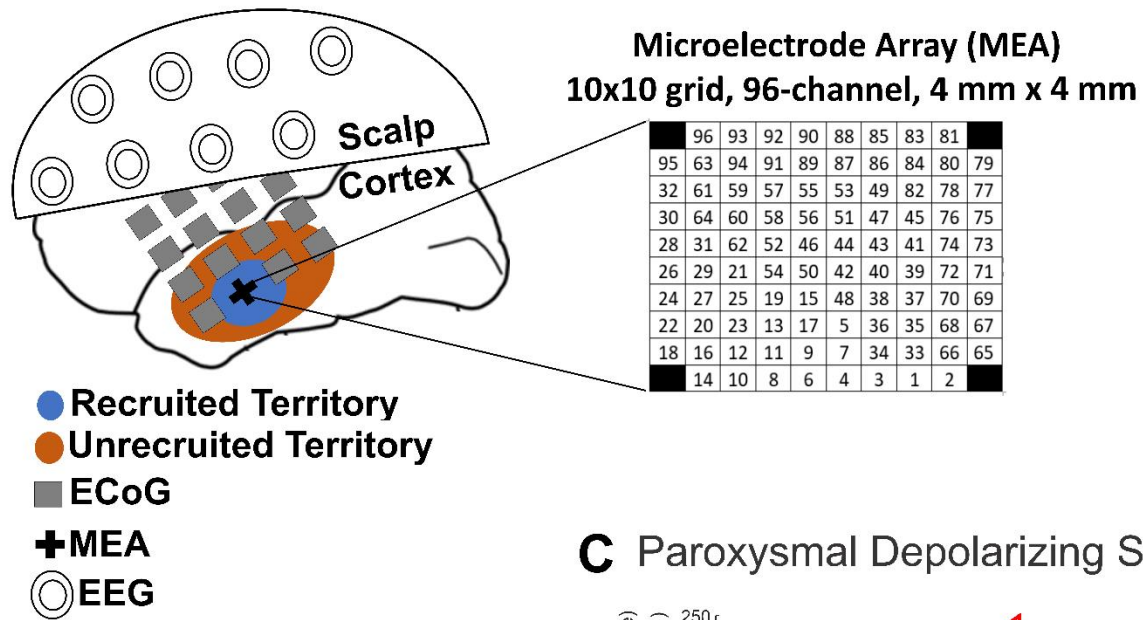
spiking activity and synchronized bursting, while the unrecruited territory is the surrounding territory characterized by non-synchronous, lower spiking activity (Schevon *et al.*, 2012; Weiss *et al.*, 2013). Over time, more neurons are recruited into recruited territory by the propagating ictal wavefront (Fig. 1.1B). Furthermore, the macroscopic low frequency component of the LFP is correlated with multi-unit spiking activity in recruited territory as far as 10 cm away, suggesting that there is an interaction among scales (Eissa *et al.*, 2017).

1.3 Excitation and Inhibition Imbalance

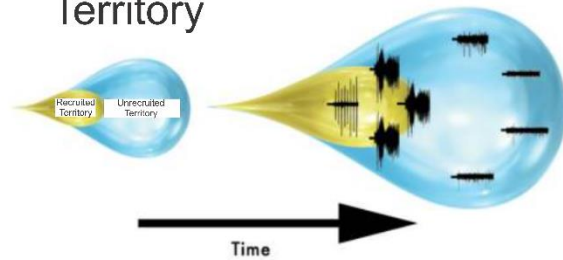
While the exact mechanisms that govern epilepsy are yet to be fully determined, one of the fundamental principles of epileptic pathology is the imbalance of excitation and inhibition. Epileptic seizures are associated with uncontrolled hyperexcitability, hypersynchrony, and disrupted network communication (Tryba *et al.*, 2019). Hyperexcitation is excessive neural activity associated with large deflections in EEG & high firing rates, and hypersynchrony is synchronous activity across neural populations associated with high amplitude signals (Tryba *et al.*, 2019). These concepts may seem contradictory: hyperexcitation seems to favor E over I, while hypersynchrony suggests that the balance instead alternates between E and I (Tryba *et al.*, 2019). The E/I imbalance may be explained by acquired insults (e.g. structural alterations in circuitry due to head trauma (Stafstrom & Carmant, 2015)) or genetic factors, like abnormal circuitry in cortical dysplasia or ion channel mutations in benign familial neonatal epilepsy (Poduri & Lowenstein, 2011; Berkovic, 2015). Several candidate mechanisms have been proposed to explain ictal hyperexcitation and failure of inhibition (Tryba *et al.*, 2019): 1) increased extracellular K^+ concentration, which results in depolarization and a further increase in excitation (Rutecki *et al.*, 1985; Ying *et al.*, 2015); 2) increased intracellular Cl^- concentration in excitatory neurons, which reduces inhibitory efficacy by decreasing the hyperpolarizing effect of

GABA_A receptors (Staley, 2006; Glykys *et al.*, 2017); 3) decreased local extracellular Ca²⁺ concentrations at seizure onset (Han *et al.*, 2015; Rajakulendran and Hann, 2016); and 4) paroxysmal depolarizing shift (PDS) (Fig. 1.1C). PDS is considered an intracellular correlate of seizure activity and results from enhanced synchronization of the neuronal population (Matsumoto & Marsan, 1964; Greiner *et al.*, 2003; Hotka & Kubista, 2019; Tryba *et al.*, 2019). PDS is characterized by: (1) a burst of action potentials with decreasing amplitudes, (2) sustained, plateau-like depolarization, followed by (3) repolarization and termination (Fig. 1.1C) (Matsumoto & Marsan, 1964; Greiner *et al.*, 2003; Hotka & Kubista, 2019; Tryba *et al.*, 2019). Investigating this E-I imbalance is currently an active area of research. It is well-established that failure of inhibition at the local, mesoscale allows the ictal wavefront to propagate in focal seizures (Schevon *et al.*, 2012; Meijer *et al.*, 2015; Eissa *et al.*, 2017). In addition, one study investigated the relationship between mesoscopic and macroscopic network properties and found that failure of inhibition at the ictal wavefront allows for propagation, yet activation of feedforward inhibition on a macroscopic scale allows the waveform to propagate in a distinct dynamical pathway (Eissa *et al.*, 2017). These results suggest that inhibition plays different roles across multiple scales during ictal activity.

A Multi-Scale Recording Modalities



B Recruited and Unrecruited Territory



Panel adapted from Weiss *et al.*, 2013

C Paroxysmal Depolarizing Shift

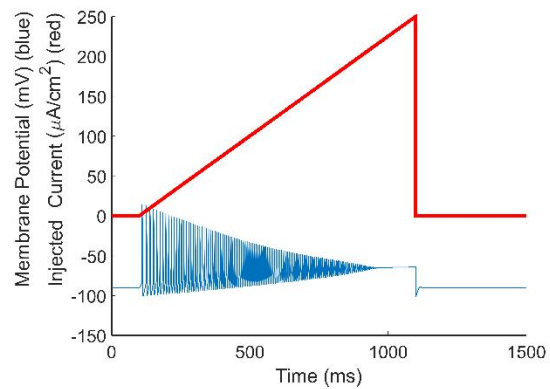


Figure 1.1: Schematics of multi-scale recording modalities, recruited and unrecruited territories, and paroxysmal depolarizing shift. **A)** Multiscale recording modalities in epilepsy include scalp electroencephalogram (EEG), electrocorticogram (ECoG), and microelectrode arrays (MEA). A schematic of the Utah array, which is a 10x10 grid, 96-channel, 4 mm x 4 mm MEA, is placed on the putative seizure onset zone, as shown by the recruited territory. **B)** The recruited territory is characterized by increased neuronal firing and highly synchronous activity (yellow), while unrecruited territory is characterized by lower neuronal firing (blue). The edge of the recruited territory is the expanding ictal wavefront and consists of the most intense neuronal firing activity (panel adapted from Weiss *et al.*, 2013). **C)** Paroxysmal depolarizing shift (PDS) can be simulated using a Hodgkin-Huxley model of a single neuron in response to increasing current, which shows decreasing action potential spike amplitudes and eventually depolarization.

1.4 Computational Models in Epilepsy Research

Computational models can range from the single neuron (microscopic) level, which usually involves the Hodgkin-Huxley model or some modification thereof, to the population (mesoscopic and macroscopic) scale, which accounts for neural activity across groups of neurons, typically modeled by a set of mathematical equations (e.g. neural mass models, Wilson-Cowan model). Utilization of various computational models across these multiple scales have resulted in significant and meaningful findings in epileptic seizure research.

1.4.1 Cellular models

Many cellular and sub-cellular models at the single neuron scale have been used to investigate epilepsy. These models typically focus on the biophysical properties and/or electrochemical properties of neurons, such as ion channel dynamics and synapses. One of the most famous and consequential cellular models in neuroscience was developed by Alan Hodgkin and Andrew Huxley in 1952. The *Hodgkin-Huxley (HH) model* consists of four nonlinear differential equations that describe the dynamics of the action potential by modeling the resulting change in membrane potential due to sodium channel activation & inactivation and potassium channel activation. The HH model has been used extensively to investigate seizure activity. One of the early studies to do so used an HH network model of 100 hippocampal neurons to show that neuronal synchronization could lead to interictal spiking activity (Traub & Wong, 1982). Conductance-based models and modifications thereof have since lead to significant insights into understanding the mechanisms and markers of epileptic activity, such as synchronicity of neuronal activity (Traub *et al.*, 1991), synchronized oscillations and propagating waves (Destexhe *et al.*, 2001), interictal epileptic activity (Wendling *et al.*, 2002), and the effects of different pharmacological treatments (Lytton, 1998).

There have since been several simplifications to the HH model, namely the Fitzhugh-Nagumo model, the Morris-Lecar model, and the Izhikevich model. These models reduce the number of variables and equations from the HH model while still retaining the essential properties. The *Fitzhugh-Nagumo (FN) model*, developed by Richard Fitzhugh in 1961 and later extended by J. Nagumo in 1962, reduces the four nonlinear differential equations of the HH model into a set of two ordinary differential equations (Fitzhugh, 1961; Nagumo *et al.*, 1962). Due to its simplicity and computational efficiency, the FN model has been used extensively in epileptic seizure research (Gerster *et al.*, 2020; Ibrahim *et al.*, 2021; Salfenmoser *et al.*, 2022). Furthermore, with specific parameters, the FN model can generate limit cycle oscillations, which can reflect the sustained and rhythmic activity characteristic of epileptic seizures. The *Morris-Lecar (ML) model* is also a two-dimensional simplification of the HH model, and it describes the flow of potassium and calcium across the membrane potential (Morris & Lecar, 1981). Similar to the FN model, the ML model can exhibit a variety of dynamical behaviors, such as periodic oscillations and steady-state resting potentials, depending on the combinations of input parameters (Morris & Lecar, 1981). As such, the ML model has been used for epileptic seizure modeling to simulate seizure-like activity across multiple scales, ranging from individual neurons (Ermentrout *et al.*, 2008) to neuronal networks (Naze *et al.*, 2008). The *Izhikevich model* is another two-dimensional simplification of the HH model, which was developed by Eugene M. Izhikevich in 2003 (Izhikevich, 2003). This model can exhibit a variety of spiking patterns and behaviors, such as regular spiking, bursting, chattering, etc; and for this reason, multiple studies have used this model to study seizure dynamics in neuronal networks (Izhikevich, 2003; Strack *et al.*, 2013; Tryba *et al.*, 2019; Depannemaecker *et al.*, 2021).

1.4.2 Population-scale models

Population-scale models can be used to gain insights into the complex mechanisms underlying seizures. With this approach, mesoscopic and macroscopic scales of neuronal networks can be used to simulate patterns exhibited by large groups of neurons. This allows for investigation into mechanisms that drive seizure onset, propagation, and termination, as well as insights into how changes in overall connectivity between E-I populations can govern seizure dynamics. A neural mass model is one type of population model that simulates the overall behavior of a group of neurons from one specific brain region. This model is particularly useful for evaluating large-scale brain activity and for investigating seizure mechanisms (Wendling *et al.*, 2002; Eissa *et al.*, 2017). The Wilson-Cowan model was introduced in 1972 to describe macroscopic brain dynamics by considering the interactions between E-I populations (Wilson & Cowan, 1972). The Wilson-Cowan model is a mean-field model, meaning it approximates the numerous and complex interactions between individual neurons by considering the average effect of each population (Wilson & Cowan, 1972; Destexhe *et al.*, 1998; Brunel, 2000). This consequential model laid the groundwork for population-scale modeling efforts and has been extensively used to investigate seizure dynamics, especially with respect to neuronal synchronization and oscillations (Borisjuk *et al.*, 1995; Campbell & Wang, 1996) and large-scale brain dynamics using EEG (Keeley *et al.*, 2013; Li *et al.*, 2022).

1.5 Overview of Dissertation

The overarching goal of the work presented in this dissertation is to uncover information hidden within brain networks. We apply a combination of signal processing, mathematical modeling, and computational methods to ultimately bridge the gap between signals recorded from the brain and extracting and interpreting pertinent information from those signals. Chapter

2 demonstrates that for human focal seizures, there is a mathematical symmetry between the temporal and spatial domains of the spatiotemporal spike-centered averages (st-SCA) if the st-SCAs resemble sinc functions. Chapter 3 presents a novel theoretical framework to capture neural network activity completely and uniquely using triple correlation, which relates three nodes in space and time. Chapter 4 builds upon the approach from Chapter 3 to develop a novel quantitative metric of network activity by computing the entropy from the triple correlation spatiotemporal lag distribution. Chapter 5 provides insights underlying the mechanisms of cell-type activity during human focal seizures by utilizing modeling approaches. Lastly, I explore the translational implications and future directions of this work in Chapter 6.

CHAPTER 2

SPATIOTEMPORAL SPIKE-CENTERED AVERAGING REVEALS SYMMETRY OF TEMPORAL AND SPATIAL COMPONENTS OF THE SPIKE-LFP RELATIONSHIP DURING HUMAN FOCAL SEIZURES¹

2.1 Summary

The electrographic manifestation of neural activity can reflect the relationship between the faster action potentials of individual neurons and the slower fluctuations of the local field potential (LFP). This relationship is typically examined in the temporal domain using the spike²-triggered average. In this study, we add a novel spatial component to this relationship. Here we first derive a theoretical model of the spike-LFP relationship across a macroelectrode. This mathematical derivation showed a special symmetry in the spike-LFP relationship wherein a sinc function in the temporal domain predicts a sinc function in the spatial domain. We show that this theoretical result is observed in a real-world system by characterizing the spike-LFP relationship

¹This chapter is reproduced from the following publication under the Creative Commons Attribution 4.0 International License from: Lee S*, Deshpande SS*, Merricks EM, Schlafly E, Goodman R, McKhann GM, Eskandar EN, Madsen JR, Cash SS, van Putten MJAM, Schevon CA, van Drongelen W. Spatiotemporal spike-centered averaging reveals symmetry of temporal and spatial components of the spike-LFP relationship during human focal seizures. *Commun Biol.* 2023 Mar 25;6(1):317. *equal contribution

Link to Creative Commons license: <http://creativecommons.org/licenses/by/4.0/>

Attestation Statement: The work presented in this chapter was a collaborative effort with Somin Lee in the Wim van Drongelen lab. Somin and I contributed equally to both research and authorship and share first-authorship.

²Note: For the entirety of this dissertation chapter (unless explicitly noted otherwise), the terms “spike” or “ictal spike” refer to action potentials.

The format of this chapter differs from the other chapters in this dissertation in that the Results and Discussion sections are presented before the Methods section. This ordering facilitates the storyline and flow of the results presented.

using microelectrode array (MEA) recordings of human focal seizures. To do this, we present a novel approach, termed the spatiotemporal spike-centered average (st-SCA), that allows for visualization of the spike-LFP relationship in both the temporal and spatial domains. We applied this method to 25 MEA recordings obtained from seven patients with pharmacoresistant focal epilepsy. Of the five patients with MEAs implanted in recruited territory, three exhibited spatiotemporal patterns consistent with a sinc function, and two exhibited spatiotemporal patterns resembling deep wells of excitation. These results suggest that in some cases characterization of the spike-LFP relationship in the temporal domain is sufficient to predict the underlying spatial pattern. Finally, we discuss the biological interpretation of these findings and propose that the sinc function may reflect the role of mid-range excitatory connections during seizure activity.

2.2 Introduction

Spatiotemporal patterns of brain electrical activity reflect neural mechanisms underpinning different brain pathologies. Consequently, temporal and spatial patterns observed in electrographic recordings are frequently employed to guide diagnostic and therapeutic approaches in the treatment of epilepsy. During surgical evaluation of patients with epilepsy, a variety of electrodes are used to record brain electrical activity across different scales. For example, large-scale (cm-range) global activity can be recorded by macroelectrodes at the scalp or cortex, and mesoscale (mm-range) and microscale (sub-mm range) activity can be recorded by intracranial arrays or bundles of microelectrodes (Eissa *et al.*, 2017; Eissa *et al.*, 2016; Schevon *et al.*, 2012). Despite the heavy reliance on electrophysiology in clinical practice, the relationship between neural activity across scales and the mechanistic implications of the observed spatiotemporal patterns remain poorly characterized.

One important question in understanding cortical seizure dynamics is how the activity of individual neurons relates to local and global network activity in ictal and interictal states. The interactions of neural networks during human focal seizures across micro-, meso- and macroscopic scales have been characterized by other recent studies (Eissa *et al.*, 2017). Specifically, one study showed that the spike-triggered average (STA) of the ongoing low frequency component of the local field potential (LFP) could be approximated by a sine cardinal (sinc) function (Eissa *et al.*, 2018). Furthermore, filtering a train of ictal action potentials with a rectangular (brick wall) filter generated an output that correlated well with the observed seizure, consistent with the fact that the Fourier transform of a rectangular function is the sinc function (Boashash, 2016). While the ictal STA was determined in the temporal and frequency domains, the spatial component of the relationship between action potentials and low frequency LFP was not characterized.

Similarly, most previous studies that describe the relationship between single spiking activity and the surrounding LFP have focused primarily on temporal descriptions using the STA (Bazelon *et al.*, 2010; Glickfeld *et al.*, 2009). The few studies that have investigated the spatial component of this relationship do so by incorporating spatial information into the STA through the addition of spatial filters (Telenczuk *et al.*, 2017) or use a covariance-based approach (Rust *et al.*, 2004). None so far have directly visualized the full spatial topography of LFP associated with spiking activity.

In this study, we present a mathematical model describing an ictal spike as measured by a macroelectrode to show that in special cases, the temporal and spatial features of the spike-associated LFP can predict one another. We hypothesize that this spatiotemporal relationship is governed by the network state (ictal vs. non-ictal) and the location in the network (recruited vs.

unrecruited seizure territory). To test whether this relationship can be observed in real electrographic recordings of human seizures, we developed a novel approach, termed the spatiotemporal spike-centered average (st-SCA), in which the spatial topography of spike-associated LFP can be visualized by calculating a spatial average of the LFP centered around the location of individual spikes. Calculation of this topography results in a powerful tool that allows for the visualization of both the spatial and temporal components of the spike-LFP relationship. This visualization confirmed that in a subset of patients, a 1D-sinc function in the temporal domain was associated with a pattern consistent with a 2D sinc function in the spatial domain. This result suggests that in these special cases, the underlying spatial activation pattern can be inferred from temporal measurements alone. In the discussion, we propose that the temporal sinc function can be adequately described by data from sparse sampling, opening up the possibility that these spatial patterns can be inferred without the use of gridded microelectrode arrays. Finally, we explore the biological mechanisms and clinical implications of the newly observed spatiotemporal properties in the context of pharmacoresistant focal epilepsy.

2.3 Results

2.3.1 Theoretical model of the spike-LFP relationship

To generate a theoretical prediction of the temporal and spatial components of the spike-LFP relationship, we first introduce a mathematical model of a macroelectrode that measures the network LFP response to a single spike (Fig. 2.1). In this model, a single ictal action potential is generated at the center under a macroelectrode that covers a cortical surface bounded by $[-R, R]$, and the associated LFP is measured. If the spike is represented by a unit impulse, the delta function $\delta(r, \tau)$, the correlation between the spike and LFP can be described as a unit impulse response (UIR), $UIR(r, \tau)$, that is governed by some function $f(r, \tau)$ of space (r) and time (τ).

We first evaluate the UIR in the time domain, $UIR(\tau)$. Because the potential of cortical generators attenuates sharply with distance, we assume that we may ignore contributions associated with the centrally located impulse in areas not directly under the macroscopic electrode. Under this assumption, the electrode's signal can be approximated by summing the contributions over only the neocortical area under the electrode:

$$UIR(\tau) \approx \int_{-R}^R f(r, \tau) dr = \int_{-\infty}^{\infty} rect(-R, R) f(r, \tau) dr \quad (\text{Equation 2.1})$$

where $rect(-R, R)$ represents a rectangular window bounded by $[-R, R]$.

Similarly, we can find the UIR in the spatial domain, $UIR(r)$, by integration over a fixed time epoch, $[-T, T]$:

$$UIR(r) \approx \int_{-T}^T f(r, \tau) d\tau = \int_{-\infty}^{\infty} rect(-T, T) f(r, \tau) d\tau \quad (\text{Equation 2.2})$$

In most cases, the underlying function $f(r, \tau)$ cannot be simply derived by measuring $UIR(\tau)$ and $UIR(r)$. There is a special case, however, where this derivation is possible. Note that in Eissa *et al.* (2018), the temporal UIR of an ictal network was characterized and was shown to have the following relationship:

$$UIR(\tau) \propto sinc(\tau) \quad (\text{Equation 2.3})$$

Substituting this relationship into Eq. 1 results in the following:

$$sinc(\tau) \approx \int_{-R}^R f(r, \tau) dr = \int_{-\infty}^{\infty} rect(-R, R) f(r, \tau) dr \quad (\text{Equation 2.4})$$

Because the sinc function is the Fourier transform of a rectangular function, the relationship between time and space parallels a time-frequency Fourier-transform-pair (Supplementary Text: The sine cardinal (sinc) function, Fig. 2.7) (Boashash, 2016). Thus, in the special case where $UIR(\tau)$ is described by a sinc function, we find:

$$f(r, \tau) \propto e^{jr\tau} \quad (\text{Equation 2.5})$$

The identification of $f(r, \tau)$ above now enables us to find the spatial UIR $UIR(r)$:

$$UIR(r) \propto \int_{-T}^T f(r, \tau) d\tau = \int_{-\infty}^{\infty} \text{rect}(-T, T) f(r, \tau) d\tau = \int_{-\infty}^{\infty} \text{rect}(-T, T) e^{jr\tau} d\tau = \text{sinc}(r)$$

(Equation 2.6)

Thus, we find that the temporal and spatial components of the ictal UIR are symmetric and both described by sinc functions. Note that in our model we assume that f only depends on the distance r from the unit impulse. Thus, while the temporal sinc function $\text{sinc}(\tau)$ has one dimension (time), the spatial sinc function $\text{sinc}(r)$ is a two-dimensional function that covers a flat surface. Fig. 2.7 shows examples of 1D and 2D sinc functions.

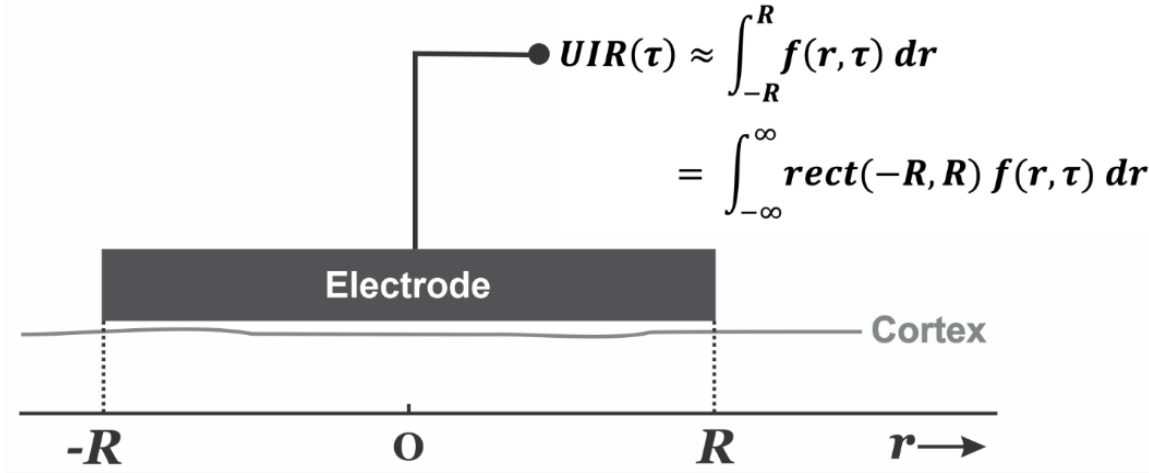


Figure 2.1: Mathematical model of the spike-LFP relationship. The electrode covers an area of one-dimensional cortex where we record the effect related with a single ictal action potential at location $r = 0$ and time $\tau = 0$, represented by the unit impulse $\delta(r, \tau)$. In this scenario, the macroelectrode measures the underlying network's temporal component of the UIR, $UIR(\tau)$. This measurement can be approximated by an unknown spatiotemporal cortical function, $f(r, \tau)$ associated with the action potential, integrated over the spatial range $[-R, R]$ covered by the electrode.

2.3.2 Characterization of the spike-LFP relationship in microelectrode arrays

Next, we asked whether the results of the above theoretical derivation could be observed in a real-world system, specifically in human seizures recorded by microelectrode arrays (MEA; Fig. 2.2A). To do this, we develop a calculation that we have termed the spatiotemporal spike-

centered average (st-SCA). The st-SCA builds upon the more typically utilized spike triggered average (STA) by accounting for both the timing and location of the spikes.

The spike-LFP relationship can be characterized in the temporal domain by calculating the cross-correlation $C(\tau)$ between the spiking activity and associated LFP. This cross-correlation $C(\tau)$ is mathematically equivalent to and frequently referred to as the STA (Ito, 2015). To find an expression for $C(\tau)$, we first represent a multi-unit spike train with N spikes occurring at times t_i as a series of delta functions:

$$\sum_{i=1}^N \delta(t - t_i) \quad (\text{Equation 2.7})$$

We then take the average LFP in a temporal window defined by a positive or negative lag τ around the spike times t_i . This results in the following:

$$C(\tau) = \frac{1}{N} \int_{-\infty}^{\infty} (\sum_{i=1}^N \delta(t - t_i)) LFP(t + \tau) dt = \frac{1}{N} \sum_{i=1}^N LFP(t + \tau) \quad (\text{Equation 2.8})$$

To expand this expression to include a spatial component, we must account for both the spikes' timing (t) and location in the cortical plane (x, y). We first represent a multi-unit spike train with N spikes occurring at times t_i and at locations (x_i, y_i) as a series of delta functions:

$$\sum_{i=1}^N \delta(x - x_i, y - y_i, t - t_i) \quad (\text{Equation 2.9})$$

We then take the average LFP in a temporal window defined by a positive or negative lag τ around spike times t_i and a spatial window defined by the plane (ξ, ψ) around locations (x_i, y_i) . This produces the expression for the normalized spatiotemporal cross-correlation $C(\xi, \psi, \tau)$ between the LFP and action potential:

$$C(\xi, \psi, \tau) = \frac{1}{N} \iiint (\sum_{i=1}^N \delta(x - x_i, y - y_i, t - t_i)) LFP(x + \xi, y + \psi, t + \tau) dx dy dt \quad (\text{Equation 2.10})$$

To evaluate this expression, we interchange the integration and summation operations and integrate over the spatiotemporal domain. The resulting expression is what we have termed as the spatiotemporal spike-centered average (st-SCA):

$$C(\xi, \psi, \tau) = \frac{1}{N} \sum_{i=1}^N LFP(x_i + \xi, y_i + \psi, t_i + \tau) = st-SCA(\xi, \psi, \tau) \quad (\text{Equation 2.11})$$

Note that if we set the range of (ξ, ψ) equal to the area covered by a fixed spatial range, we obtain the well-known temporal STA as in Eq. 1 (Fig. 2.2B). In contrast, if we set τ to a fixed temporal range, we obtain purely the spatial component of the st-SCA for that epoch, conform Eq. 2. In the following, we describe the computational steps to determine the st-SCA in MEA recordings.

2.3.3 Application of st-SCA to clinical microelectrode array recordings

To apply the st-SCA to microelectrode array (MEA) recordings, we must account for the irregular timing and location of spiking activity across the array. A simplified analogy of this approach is to visualize spiking activity as stones being tossed into water. Consider throwing a single stone into water and analyzing the consequent effects by observing the resulting water ripples. We can simulate multiple sources by dropping identical stones from the same height but at different times and locations across the horizontal plane of the water surface, resulting in a complex landscape. To determine the contribution of a single stone to this landscape, we can take a field of view centered around individual stones. According to Eq. 11, averaging across all stones gives the stone's characteristic spatiotemporal perturbation.

To apply this to the analysis of MEA recordings, spikes are detected for each channel in the MEA (Fig. 2.2C, left column), and the low frequency LFP associated with each spike is determined (Fig. 2.2C, middle column). This LFP is then spatially translated such that the associated spike position (x, y) is at the origin of a new axes (ξ, ψ) (Fig 2.2C, right column).

This spike detection and LFP translation process is then applied to all channels. Averaging the results across all channels results in a field of view of the spike-associated LFP that is (1) centered around individual spikes and (2) approximately four times larger than the area of the MEA (Fig. 2.2C, right panel). This field is then calculated for time points τ to result in the st-SCA.

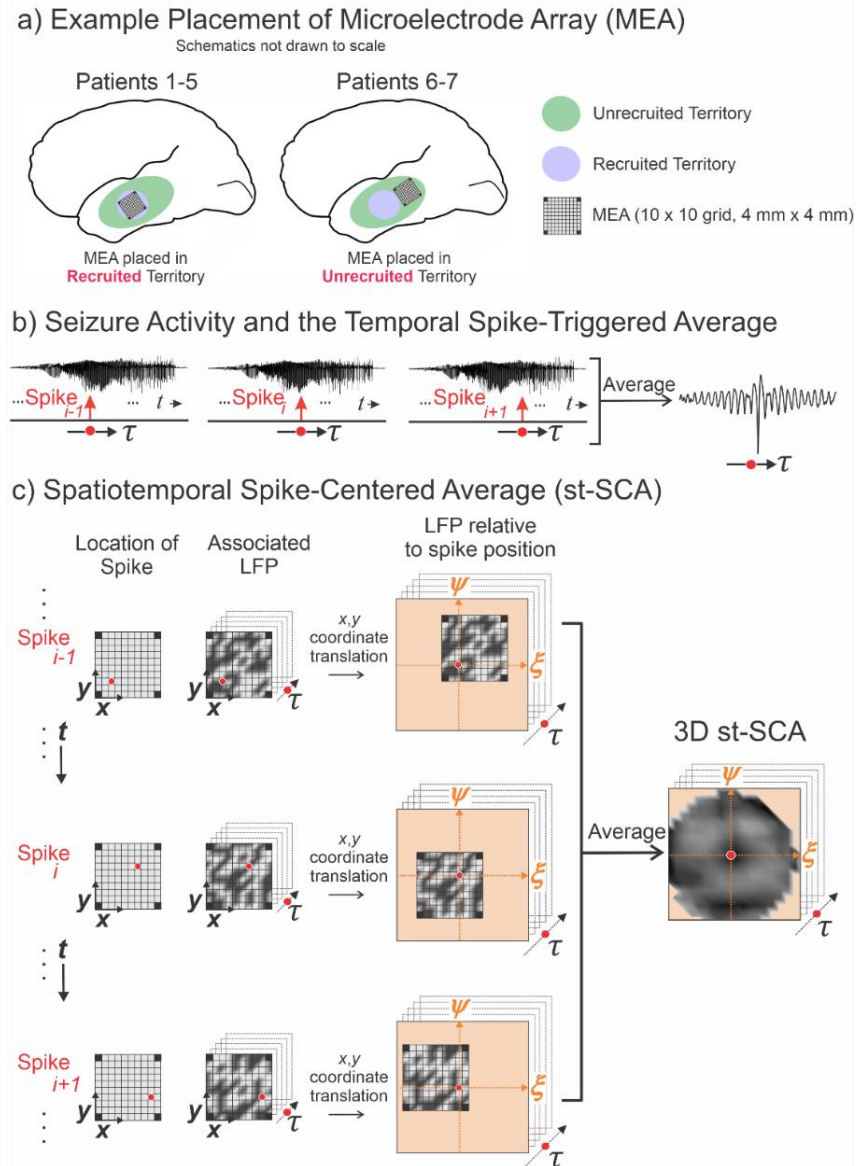


Figure 2.2: Method to compute the st-SCA. **A)** Diagram of the microelectrode array (MEA) placement, a 10x10 grid of electrodes of 4 mm x 4 mm in size, was implanted in either recruited territory (blue shading; Patients 1-5) or unrecruited territory (green shading; Patients 6-7). Recruited territory involves a seizure passing through and invading the local cortical tissue, and unrecruited territory is tissue outside the recruited territory but may still be characterized by strong, local synaptic activity (Schevon *et al.*, 2012; Merricks *et al.*, 2021). **B)** During seizure activity, the LFPs within the area of the electrode array (the summed LFP of the microelectrode array is depicted in the black signal traces) are associated with a multi-unit action potential train. The LFP's relationship to the spike is considered over time τ relative to the spike events. **C)** For each spike across the MEA, its associated spatiotemporal LFP is determined. The red circle in the middle column indicates the spike position on the MEA. Next, the (x, y) axes of the LFP are translated into the (ξ, ψ) axes, such that the spike position is at the origin. Finally, the results in the right column are averaged to create a matrix that contains the st-SCA. Note that the corners of the average are undefined because the MEA does not have electrodes in the corner positions.

2.3.4 Visualization of spatial and temporal components of the spike-LFP relationship

We applied the st-SCA method to analyze microelectrode recordings of 19 focal seizures across seven patients undergoing epilepsy surgery evaluation (Table 2.1). These recordings were obtained from 96-channel, 4x4mm Utah microelectrode arrays (MEA) (Schevon *et al.*, 2012; Truccolo *et al.*, 2011) (Methods). Although the MEA was implanted in the seizure onset zone as determined during clinical assessment for all patients, five patients were determined to have arrays implanted in recruited seizure territory (Patients 1-5), and two patients had arrays implanted in unrecruited seizure territory (Patients 6-7) (Fig. 2.2A). As previously described (Schevon *et al.*, 2012; Truccolo *et al.*, 2011), recruited seizure territory is an area of tissue that is invaded by the ictal wavefront throughout the course of a seizure. The ictal wavefront is defined by high rates of firing that are highly correlated with overlying low frequency rhythms. Unrecruited territory sees no invasion of the ictal wavefront but still shows rhythmic EEG activity due to local synaptic activity (Merricks *et al.*, 2021; Schevon *et al.*, 2012). Both ictal and interictal recordings were evaluated, where interictal was defined as being at least two hours away from any known ictal activity. Filtering was used to extract local multi-unit neural firing activity and the associated low frequency component of the LFP of the surrounding network (Methods).

Representative ictal and interictal signals and STAs calculated across ictal and interictal states for two recruited territory recordings and one unrecruited territory recording are depicted in Fig. 2.3. The black lines in Fig. 2.3C-H represent the STAs, the red lines represent the associated noise estimates, and the vertical dotted lines indicate $t = 0$, i.e., the timing of the spike trigger. For both recruited and unrecruited territory recordings, the amplitudes of the ictal STAs (Fig. 2.3C, E, G) were larger than the corresponding interictal STAs (Fig. 2.3D, F, H). The

amplitude for the unrecruited ictal STA (Fig. 2.3G), however, was much smaller than the recruited ictal STAs (Fig. 2.3C, E).

Patients with the MEA located in recruited seizure territory showed STAs with different morphologies (Fig. 2.8A-E), but all had a dominant negative peak around $t = 0$. Consistent with previous findings, we found that the STA for Patients 1-3 resembled a sinc function with a peak embedded in a weak oscillatory component (Fig. 2.3C, 2.4C, 2.8A-C) (Eissa *et al.*, 2018). In contrast, the STA for Patients 4 and 5 did not resemble a sinc function as Patient 4 showed a dominant peak embedded in a strong oscillation (Fig. 2.8D) while Patient 5 showed no oscillatory component (Fig. 2.3E, Fig. 2.4D, 2.8E). The STAs calculated from MEAs implanted in unrecruited territory (Patients 6 and 7) were weak with a smaller amplitude deflection around to $t = 0$ (Fig. 2.3G, Fig. 2.8F, G).

We then evaluated the relationship between spiking activity and the LFP in the spatiotemporal domain by computing the st-SCA over the entire MEA (ξ, ψ) and times $\tau = \pm 1\text{ms}$ (Fig. 2.4E, F). This 2ms interval averaged across to yield a 2D spatial topography. In the ictal phase for Patients 1-3, we observed a centrally located trough surrounded by a pair of rings with apparent radial symmetry, a shape that is consistent with the center of a 2D sinc function (Fig. 2.4E, 2.9A). The distance between the center and the region indicated by the inner circle was $\sim 1.5\text{mm}$, and the distance between center and the region indicated by the outer circle was $\sim 2.5\text{mm}$ (Fig. 2.4E). In contrast, the ictal phase for Patients 4 and 5 showed a deep well of stronger negative activity (Fig. 2.4F, 2.8D, E). The st-SCAs during the interictal phase as well as the results obtained in unrecruited territories showed different patterns with relatively smaller amplitude signals (Fig. 2.9B, D, E, F). The temporal and spatial results across seizures within

each patient were consistent. Representative st-SCAs for each patient are depicted in Fig. 2.8. Representative noise estimates are shown in Fig. 2.10.

In sum, three of five patients with recordings from recruited territories (Patients 1-3) showed STAs with sinc function morphology and st-SCAs with a “donut-ring” pattern that was consistent with the center of a 2D sinc function (Fig. 2.4C, E, 2.8A-C). In Patients 4 and 5, the STAs did not have a sinc morphology, and the st-SCAs showed deep and diffuse wells of negative activity (Fig. 2.4D, F; 2.8D, E).

Note that these observations were not attributable to widespread correlations among MEA electrodes. To demonstrate that the observed st-SCA patterns are representative of the spike-LFP relationship and not the global correlations among network LFPs, we showed that STAs in unrecruited territory show a large and significant oscillatory component only when triggered by spikes from recruited territories (Fig. 2.11B), and not when triggered by spikes from unrecruited territories (Fig. 2.11C). This result is a replication of previous studies (Eissa *et al.*, 2017). Furthermore, randomizing the spike times detected across the MEA resulted in complete destruction of the observed st-SCA patterns, emphasizing the importance of spike timing as the driver for these spatiotemporal patterns (Fig. 2.12). Finally, calculation of the st-SCA after applying a spatial filter to decorrelate LFP signals across MEA channels did not qualitatively alter the st-SCA patterns (Methods, Fig. 2.13).

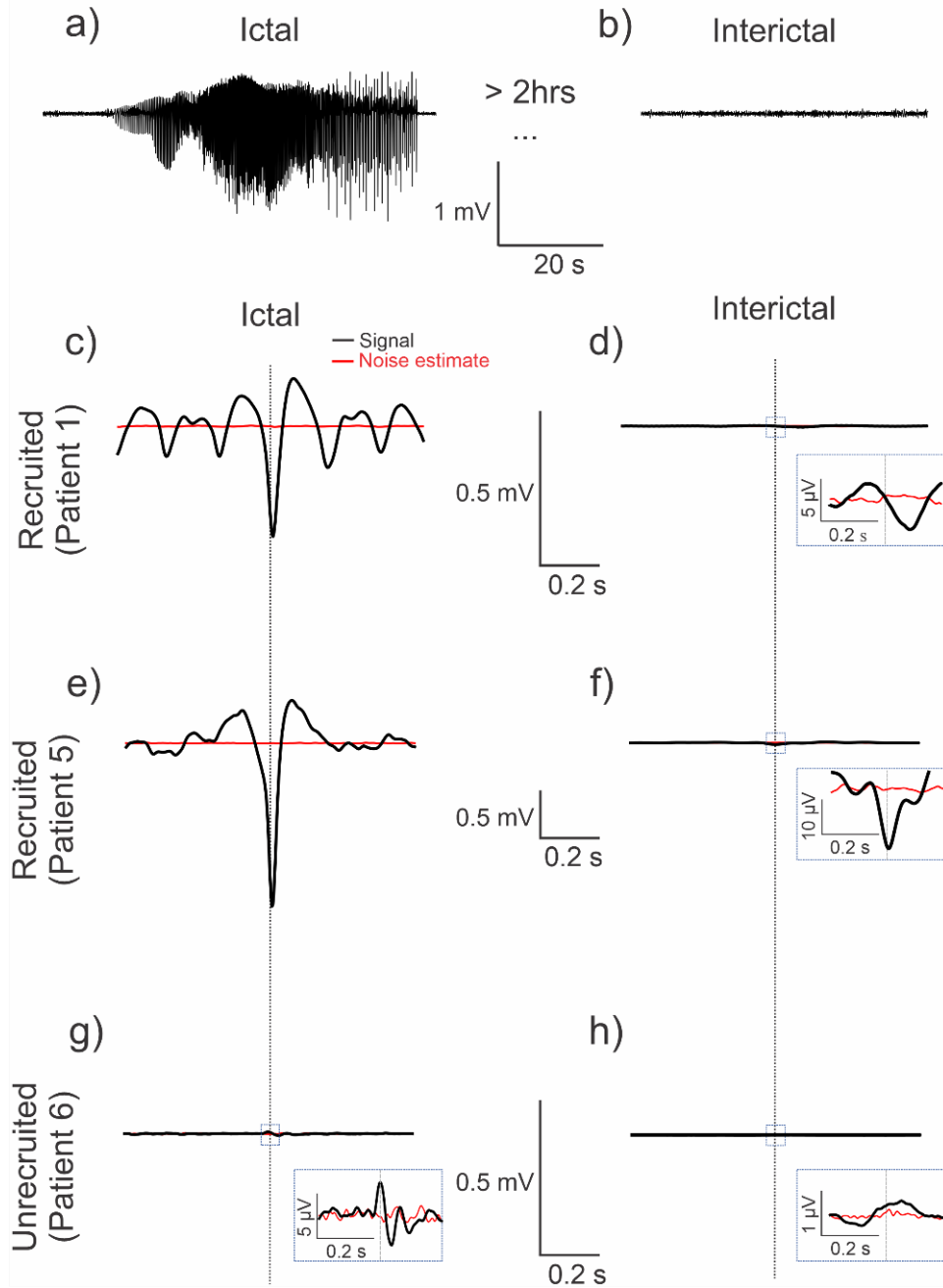


Figure 2.3: STAs in recruited and unrecruited seizure territories. The black traces are the signals, and the red traces represent the associated noise estimates. Vertical stippled lines represent the zero of the time-axis. **A-B)** Example signal trace of average ictal and interictal LFP activity across MEA channels. **C-F)** The STA (black trace) in the recruited territories show an evolution towards a characteristic negative peak, with or without surrounding oscillations, during the ictal phase. The ictal phase amplitudes are also much higher than those of the interictal phase. Noise estimates are shown in red. **G-H)** The results in the unrecruited territory show comparatively low amplitudes as compared to the recruited STAs.

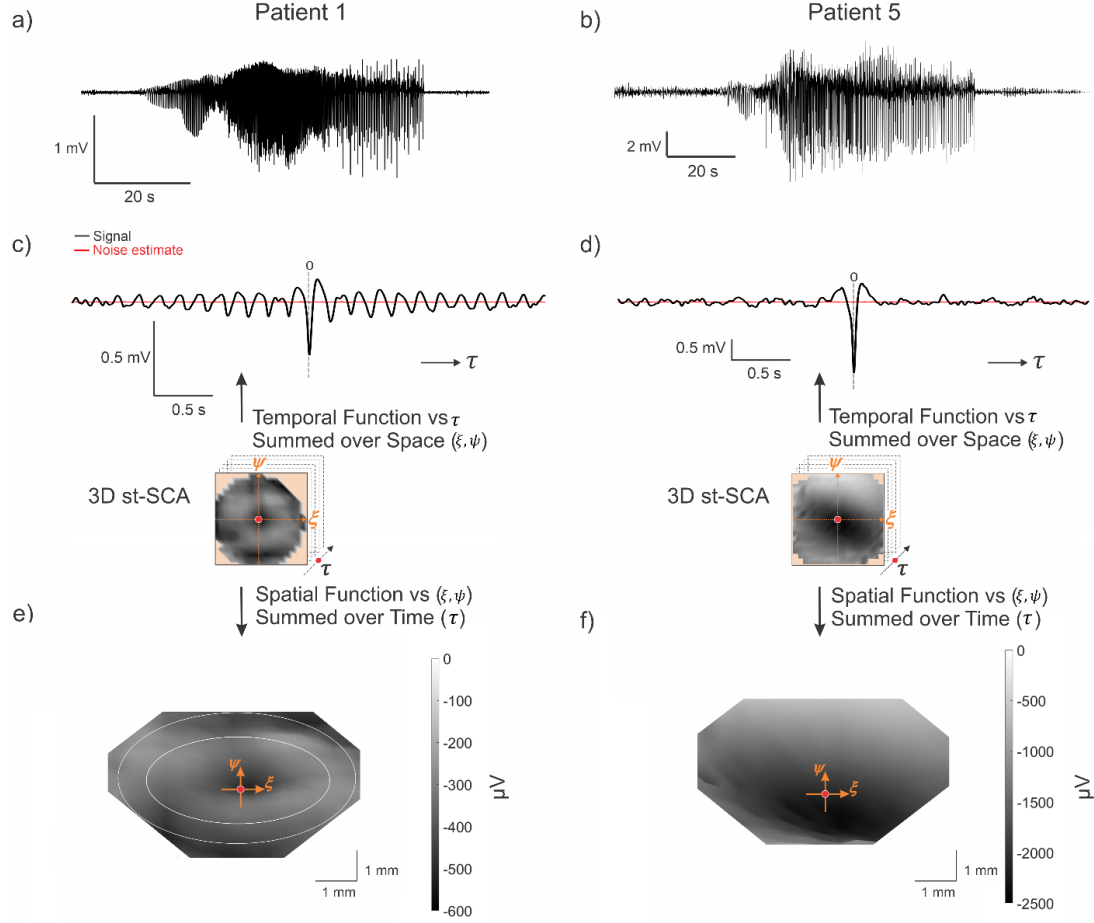


Figure 2.4: Examples of the st-SCA computation for two patients. **A-B)** Representative traces of the average LFP activity across the microelectrode array for Patient 1 and Patient 5. **C-D)** The temporal average (black trace) is calculated by averaging the st-SCA over all spatial contributions ($\pm 3.6\text{mm}$). Noise estimates are shown in red. **E-F)** A 3D view (azimuth = 0° , elevation = 70°) of the 3D st-SCA summed over time $\tau = \pm 35\text{ms}$. The center ($\xi, \psi = 0, 0$) is indicated by the red dot. The two concentric circles in (e) are drawn to indicate that the center is surrounded by two rings. Note the apparent radial symmetry of the st-SCA pattern in Patient 1. The ξ -axis and ψ -axis represent the spatial dimensions of the MEA, and the third dimension (z-axis) in this topological view represents microvolt (μV) units. The grayscale corresponds to the z-axis and is in μV units.

2.3.5 Quantification of the peak-to-peak distance of spatial patterns

Next, we aimed to more quantitatively describe the donut-shaped activity observed in Fig. 2.4E. Taking advantage of the qualitatively observed radial symmetry observed in the st-SCA, we converted the Cartesian coordinates (ξ, ψ) into polar coordinates (r, θ) and focused on

the spatial relationship with respect to r (Fig. 2.5A). This enabled us to depict the st-SCA in two dimensions, (r, τ) (Fig. 2. 5B), similar to function $f(r, \tau)$ in Fig. 2.1. A detail of that relationship is depicted in Fig. 2. 5C, and the summed values across this two-dimensional detail are plotted along its margins. These summed values are the two components as a function of space and time (r and τ). Note that the graph in the bottom margin of Fig. 2.5C represents the central trough ($\tau = \pm 35\text{ms}$) of the function shown in Fig. 2.4C. As anticipated by the outcome in Eq. 6 we observed a spatial component (Fig. 2.5C, left margin) that shows a central trough with smaller amplitude side lobes—a pattern consistent with the shape of a sinc function. Note that the resolution and range of the spatial component ($r = \pm 3.6\text{mm}$) is limited by the size of the MEA (Methods, Fig. 2.2C). Consistent with the donut-shaped rings observed in Fig. 2.4E, the peaks of the function shown in the left margin of Fig. 2. 5C were separated by $\sim 2.5\text{mm}$ (blue arrows, Fig. 2.5C).

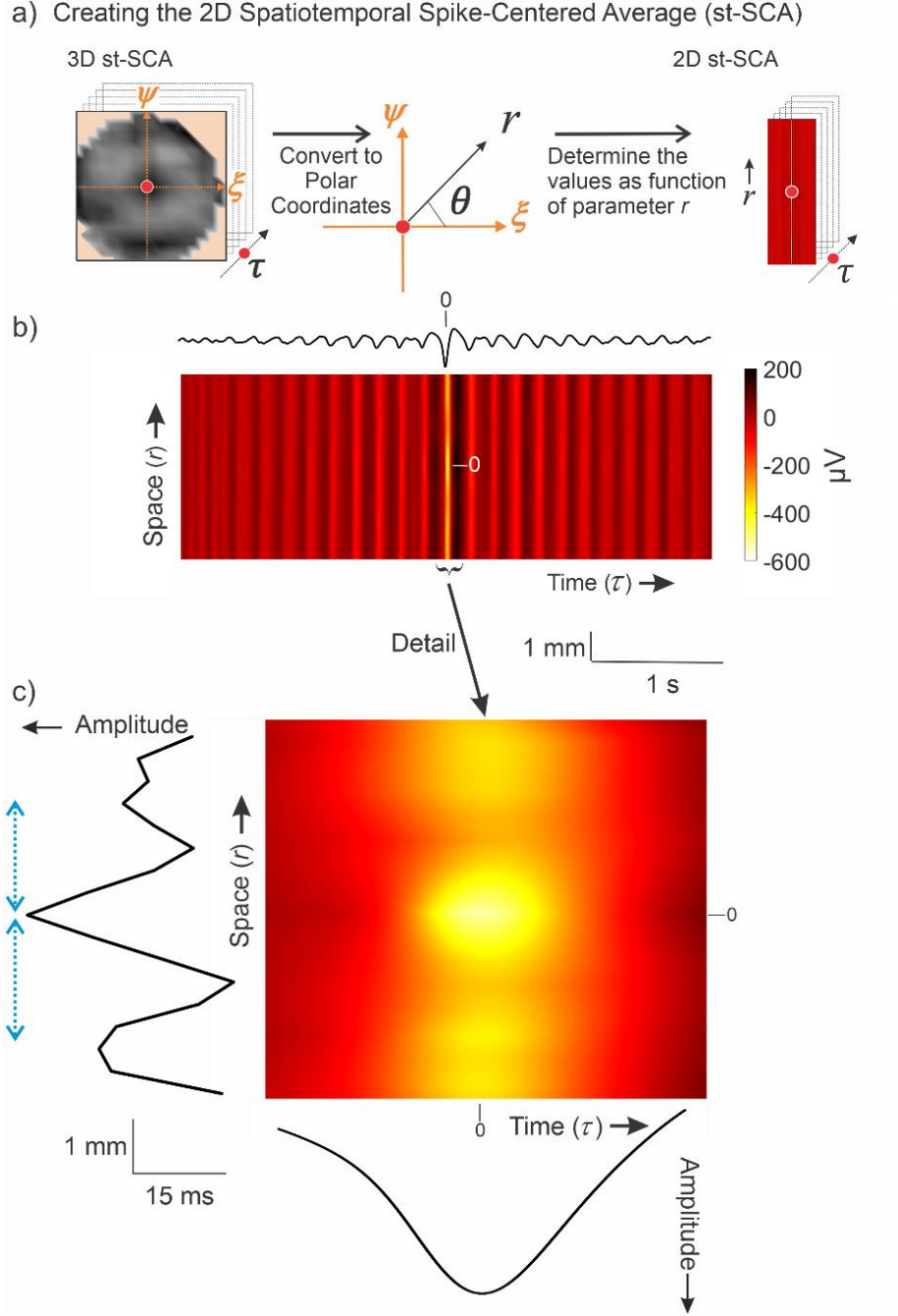


Figure 2.5: Method to compute 2D st-SCA. **A)** The Cartesian coordinates (ξ, ψ) from the 3D st-SCA are converted into polar coordinates (r, θ) , resulting in a 2D st-SCA. **B)** A color representation of $st-SCA(r, \tau)$. The temporal component of the st-SCA (τ) (black trace) is obtained by the sum of $st-SCA(r, \tau)$ over r (same as the signal in Fig. 2. 4e). Amplitude and color scales are in μV . **C)** Detail of the central part of Panel B. The left margin shows the resulting wave from summation over time, generating the spatial component of st-SCA. The blue arrows on the left indicate the distance ($\sim 2.5\text{mm}$) between the peaks seen in this function. The bottom margin depicts the resulting wave from summation over space, generating the temporal component of the st-SCA.

2.4 Discussion

A key result of this study is that there exists a mathematical symmetry between the temporal and spatial domains of the spike-LFP relationship in the special case where both domains resemble a sinc function. By characterizing the spatiotemporal components of the spike-LFP relationship in microelectrode array (MEA) recordings of human focal seizures, we showed that this mathematical symmetry is not confined to the theoretical realm. Of the five patients with recruited territory recordings, three showed temporal and spatial patterns consistent with this symmetric relationship. The existence of this symmetry in clinical recordings offers an interesting implication: in some cases, the underlying spatial pattern of the spike-LFP relationship may be inferred by characterization of the temporal pattern alone. Specifically, a sinc pattern observed in the temporal domain predicts a 2D sinc pattern in the spatial domain (Eq. 2.4-2.6; Fig. 2.1; Fig. 2.6A).

This predictive power is important in the context of clinical microelectrode recordings because it suggests that it may be possible to characterize spatial patterns without the use of gridded MEAs. While MEAs are advantageous for monitoring and studying seizure activity with high temporal and spatial resolution, their current clinical utility is limited as they cannot be easily used to sample from multiple cortical areas. Interestingly, we found that the sinc function can be characterized in the temporal domain by using spiking and LFP information from a random subset of only eight electrodes (Fig. 2.6B). Although the spatial pattern is impossible to discern with just eight electrodes, the underlying spatial pattern may be inferred to be a 2D sinc function since the associated temporal pattern is a sinc function. This suggests that the st-SCA may be characterized by using neocortical microelectrodes that allow for recording from multiple areas by reducing the number of channels per probe. The development of such electrodes is

technologically feasible as similar probes are already used clinically for the monitoring of deep brain structures such as Behnke-Fried depth electrodes (Misra *et al.*, 2014).

A natural and necessary question to ask at this junction is whether the 2D sinc function in the spatial domain has any biological meaning. While the exact mechanisms underlying temporal and spatial sinc patterns are beyond the scope of this study, we propose here that the concentric “donut-ring” pattern in the spatial component of the spike-LFP relationship may reflect the engagement of mid-range horizontal connections during seizure initiation and propagation.

Under physiological conditions, synaptic activity is a major contributor to the extracellular potential field (Nunez *et al.*, 2006). Other contributors may include intrinsic membrane currents, gap junctions, neuron-glia interactions, and ephaptic effects (Buzsaki *et al.*, 2012; Herreras, 2016). While the relative contributions of these different mechanisms during pathological states such as seizures have not been fully elucidated, a non-zero cross-correlation between action potentials and LFPs is expected because synaptic currents are a major component in the compound activities observed in ictal states.

In our discussion of the biological implications of the observed st-SCAs, we adopt the interpretation for our specific electrode configuration as previously described (Eissa *et al.*, 2017) by assigning a net excitation to negative deflections and net inhibition to positive deflections. This interpretation is also in line with previous studies of the ictal core and propagation (Schevon *et al.*, 2012; Tryba *et al.*, 2019). Accordingly, our st-SCA analyses (Fig. 2.3, 2.4) show that in the recruited ictal territory, the spike-LFP correlation at small lags is dominated by net excitation during seizures in all patients. The activity level in the excitatory center, representing the activity at the ictal wave, is excessively high, possibly due to saturation of the local inhibitory population (Tryba *et al.*, 2019). In Patients 1-3 we also observe a ring of reduced excitation at a distance

~1.5mm around the excitatory center (Fig. 2.4E, 2.8A-C). In turn, the ring of reduced excitation is surrounded by a second ring at an additional distance of ~1mm where excitation increases again. For these patients, this donut-shaped st-SCA is specific to the recruited seizure territory in the ictal phase (Fig. 2.8A-C, 2.9A). This observation suggests that the ictal wave in the recruited territory, represented by the excitatory center ($\xi, \psi = 0,0$), creates an escape of hyperexcitation via a jump that engages mid-range connectivity in the millimeter range. Decorrelation of the LFP prior to the st-SCA calculations yielded similar spatiotemporal patterns (Telenczuk *et al.*, 2017) (Fig. 2.13), further corroborating the importance of local millimeter range excitatory connections in focal seizures.

A question that remains is whether there is any biological evidence that supports this type of connectivity. Histological studies have shown that there are indeed excitatory mid-range connections at the millimeter scale mediated by axon collaterals within the gray matter in the neocortex in addition to short-range excitatory and inhibitory connections at a scale of hundreds of μm (Fig. 2.6C) (Nieuwenhuys, 1994; Oberlaender *et al.*, 2011; Pichon *et al.*, 2012; Zhang & Deschênes, 1997). Additionally, previous studies of ictal wave dynamics provide direct evidence that mm-range connections are invoked during seizure activity (Schevon *et al.*, 2012). An example of this jump in action potential activity is depicted in the spatial plot in Fig. 2.6C (a snapshot of the multiunit activity across the MEA), in which there are multiple areas of simultaneously increased neural activity across the MEA, separated by mm-range gaps. This is consistent with the distance between the excitatory center and outer ring we observe in the donut-shaped spatial cross-correlation depicted in Fig. 2.4E. This pathological escape of uncontrolled excitation across cortex could be considered a candidate mechanism in seizure recruitment and propagation (Supplementary Materials: Mechanisms for Focal Seizures).

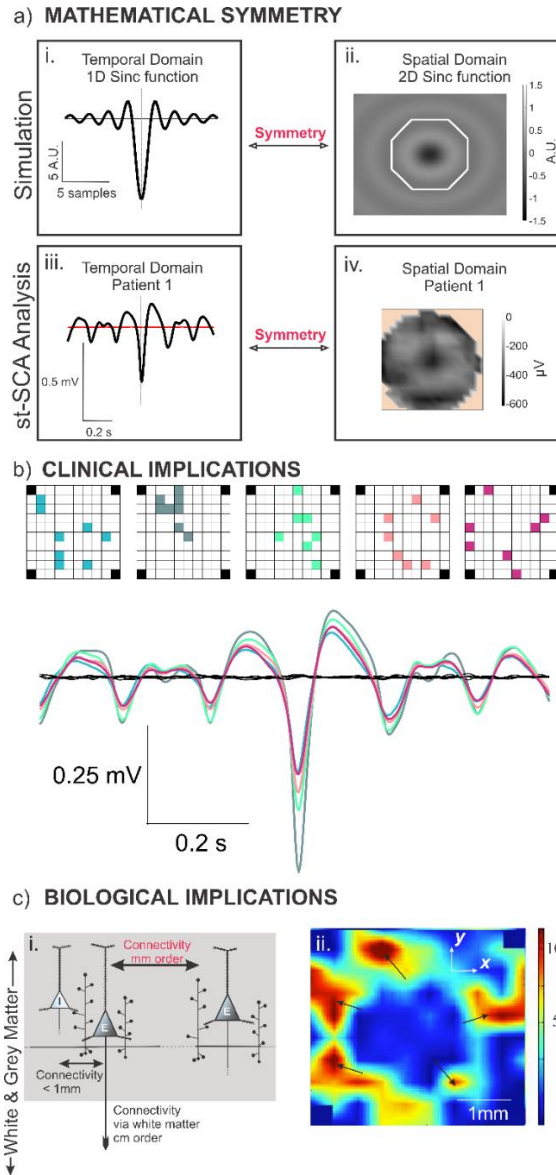


Figure 2.6: Summary of key findings and biological/clinical implications of results. A) There exists a special mathematical symmetry between the temporal and spatial domains if they resemble sinc functions. Panels ai and aii show simulated results, and Panels aiii and aiv show results from the clinical st-SCA analysis for Patient 1. B) Spike-triggered average (STA) calculated from using spike timing and LFP activity from a random subset of eight electrodes for Patient 1. The sinc function may be characterized in the temporal domain using signals from only eight channels across the MEA. C) *Panel ci*: Diagram of gray matter excitatory connections of a neocortical pyramidal cell showing the short-range connections (order of 100s of μm) and mid-range connections (order of mm) via the pyramidal cell axon collaterals (based on Fig. 2. 5 in Nieuwenhuys, 1994. *Panel cii*: Snapshot of multiunit activity across the MEA depicting the propagation of ictal multi-unit action potentials across part of a Utah array. The black arrows show multiple contiguously active areas that are separated by a mid-range mm-sized distance, supporting that the excitatory axon collateral connections are invoked for propagation of the ictal activity. Color scale represents the number of spikes per second.

Not all patients with implants in recruited territory showed spatiotemporal patterns resembling a sinc function, and the clinical etiologies for these patients may offer some clues about why this is the case. The diffuse depressions observed in the spatial domains for both Patients 4 and 5 (Fig. 2.4F, 2.8D, E, 2.9C) seem consistent with a local flood of excitation. Indeed, the seizures in both patients were characterized as secondarily generalized (Table 4.1). This suggests that in generalized seizures, the mid-range excitatory connectivity structure (as represented by the sinc function) may play a diminished role in comparison to other mechanisms of ictal propagation, such as local excitation or engagement of white matter tracts (Fig. 2.6C). Furthermore, a unique case is Patient 3, who was diagnosed with cortical dysplasia (Table 4.1). The STA is sinc-like, and the st-SCA partially resembles a sinc function (Fig. 2.8C). Cortical dysplasias have been shown to be associated with functional connectivity defects (Hong *et al.*, 2017; Jeong *et al.*, 2014; Rezayev *et al.*, 2018), which may explain the partial donut ring of activity in the st-STA (Fig. 2.8C). If indeed st-STA patterns reflect underlying pathologies, clinicians could potentially use these spatiotemporal characterizations to target specific mechanisms underlying a patient's seizures and choose appropriate therapeutic strategies. For example, removal of horizontal interactions on a mm-scale has been the rationale for performing subpial transections in patients with intractable epilepsy (Morrel *et al.*, 1989). In these cases, characterization of the st-SCA may inform the appropriateness of such interventions in personalized patient treatment plans. Furthermore, because this novel method includes the spatial domain, the st-SCA method can be used for a broad scope of applications, such as MEA cultures (Cotterill *et al.*, 2016; Kapucu *et al.*, 2022), Utah arrays implanted in monkeys completing tasks (Brochier *et al.*, 2018; Dickey *et al.*, 2009; Manyakov & Van Hulle, 2010), MEAs implanted in

humans for sleep (Le Van Quyen *et al.*, 2016), and for brain-computer interfaces (Maynard *et al.*, 1997; Woepfel *et al.*, 2021).

2.5 Methods

2.5.1 Patients

Seven patients with pharmacoresistant focal epilepsy underwent chronic intracranial EEG studies to help identify the epileptogenic zone for subsequent removal. Patients 1, 4, 6, and 7 were recruited at Columbia University Medical Center, and Patients 2, 3, and 5 were recruited from Massachusetts General Hospital/Brigham and Women's Hospitals (Table 2.1). The entirety of the ictal segments and two-minute interictal segments were used in these analyses (Table 2.1). Procedures were approved by the Internal Review Board committees at Columbia University Medical Center, The University of Chicago Comer Children's Hospital, and Massachusetts General Hospital/Brigham and Women's Hospitals. The patients' surgeries and treatment plans were not directed by or altered as a result of these studies. All ethical regulations were followed, and all patients provided informed consent regarding the use of their data for research purposes.

2.5.2 Signal acquisition and pre-processing

A 96-channel, 4 x 4mm MEA (Utah array; Blackrock Microsystems) was implanted into neocortical gyri along with subdural electrodes (ECoG). The 96 microelectrodes were 1mm in length and arranged in a regular 10x10 grid pattern with empty corners, defacterized prior to implantation. Expanded and complete details of study enrollment, clinical evaluation of the SOZ, surgical procedures, and recording parameters have been previously published (Schevon *et al.*, 2012; Truccolo *et al.*, 2014). Signals from the MEA were acquired continuously at a sample rate of 30 kHz per channel (0.3-7500Hz bandpass, 16-bit precision, range ± 8 mV). The reference was epidural. Up to three seizures from each patient were selected for detailed analysis to avoid

biasing the dataset from the patients from whom many seizures were recorded. Categorization of seizure recordings as recruited or unrecruited territory was determined (Fig. 2.2A) (Schevon *et al.*, 2012). Channels and time periods with excessive artifact or low signal-to-noise ratio were excluded. Recordings were obtained during the presurgical evaluation of the patients.

Unit activity was identified using filtered 0.3-3kHz signals with spikes defined as deflections ≥ 4 standard deviations below the mean. The low frequency component of the local field potential (LFP) activity across the array was created by averaging the artifact-free LFP activity from all micro-electrode signals filtered 2-50Hz. The averaged LFP procedure has been shown to generate signals that are representative of and comparable to nearby electrocorticography signals (Eissa *et al.*, 2017; Eissa *et al.*, 2018).

2.5.3 st-SCA calculations and signal analysis

All signal processing and statistical analyses were performed in MATLAB (MATLAB, Natick, MA, USA). The spatiotemporal spike-centered average (st-SCA) was determined using the following steps (Fig. 2. 1). Each broadband signal of the 10×10 MEA was bandpass filtered for the low frequency component (2-50Hz) of the local field potential (LFP) and for spike detection (0.3–3kHz) (Eissa *et al.*, 2017; Eissa *et al.*, 2018). Spikes were detected in the multi-unit activity as negative deflections that exceeded four standard deviations of the filtered signal. A complete list of spike detection results can be found in Table 2.2. For each spike the 10×10 frames of the LFP data were collected for $\pm n$ sample times representing ± 5 s around the spike time, and the timescale of the frames was set such that the spike occurred at time zero, $\tau = 0$. All LFP frames associated with a single spike were translated such that the spike location was at the origin of the new spatial coordinate system $\xi, \psi = 0, 0$. Note that this spatial translation is necessarily spike specific because spikes do occur at different locations. Next, the translated

$10 \times 10 \times (2n + 1)$ frames were put into a three dimensional $19 \times 19 \times (2n + 1)$ configuration with the spatiotemporal origin $(\xi, \psi, \tau = 0, 0, 0)$ is at position $10, 10, n + 1$. This step was done to keep the LFP frames compatible across spikes. For each spike, these frames were summed into a three dimensional $19 \times 19 \times (2n + 1)$ matrix. For each position in the $19 \times 19 \times (2n + 1)$ matrix, the total number of contributions N was counted. Finally, to obtain the spatiotemporal cross-correlation, the sum obtained in step 6 was divided by the N obtained in step 7 for each position. This resulted in the discrete spatiotemporal estimate of $C(\xi, \psi, \tau)$, as shown in Eq. (3). This method to determine spatiotemporal patterns is based on a spike trigger that is not constrained spatially because an ictal action potential can occur across the spatial dimension of the MEA.

Evidence of radial symmetry of the st-SCA (Fig. 2. 4e) allowed conversion from Cartesian coordinates (ξ, ψ) coordinates to polar coordinates (r, θ) . By ignoring the minor deviations from radial symmetry, we focused on the spatial component of the st-SCA with respect to r (Fig. 2. 5A), which enabled us to depict the spatiotemporal properties in two dimensions (Fig. 2. 5). Furthermore, if we compute the sum across space, we obtain purely the temporal component of the st-SCA, which is equivalent to the STA. Similarly, summation over time τ generates the spatial component of the st-SCA. With these results, we can assess to what extent our model of the ictal network, a linear time-invariant (LTI) system with unit impulse response $C(\tau) \propto \text{sinc}(r, \tau)$, fits the data.

2.5.4 Spatial filtering

For calculations involving the spatial filtering of LFP signals, we applied the spatial whitening process as described in Hyvärinen *et al.* (2001) and Telenczuk *et al.* (2017). As

previously published, a signal is spatially filtered by matrix multiplication with a whitening matrix \mathbf{W} , where \mathbf{W} is the inverse square root of the signal's covariance matrix, \mathbf{C} :

$$\mathbf{W} = \mathbf{C}_{signal}^{-1/2} = \mathbf{E}\mathbf{D}^{-1/2}\mathbf{E}^T \quad (\text{Equation 2.12})$$

where \mathbf{E} is a matrix of eigenvectors of \mathbf{C}_{signal} , and \mathbf{D} is a diagonal matrix with inverse square roots of eigenvalues λ_i on its diagonal, such that $\mathbf{D}_{ii} = \frac{1}{\lambda_i}$ and $\mathbf{D}_{ij} = 0$ (Telenczuk *et al.*, 2017). In this study, the signals being transformed were the MEA channel signals bandpass filtered at 2-50Hz.

2.5.5 Statistics and reproducibility

The number of analysis segments (both ictal and interictal) per patient, epoch length, and number of spikes are shown in Table 2.2. Replicates are defined by the number of seizures per patient. The signal-to-noise ratio (SNR) was computed for each st-SCA by estimating the residual noise using the plus-minus averaging approach. We implemented this by employing the above eight steps while keeping two three-dimensional 19×19 matrices: one summed the even contributions for each location and the other summed the odd ones. To obtain the averages for the odd and even components, each position in the matrix was then divided by its number of contributions. The sum of the even and odd averages is the same result obtained in step 8 above. In contrast, the difference between the even and odd averages cancels the consistent component (i.e., the signal) while preserving the random noise estimate (4). The SNR was estimated by computing the root mean square (rms) of the signals and the rms of their noise estimates, leading to a signal-to-noise ratio, $SNR = 20 \log \left(\frac{rms_{signal}}{rms_{noise}} \right)$ dB. Average ratios for the st-SCAs across space and time all were >30 dB.

An example of the total number of contributions per each position in the 19x19 grid is shown in Table 2.3. The average values in each pixel of the 19x19 image is based on variable numbers of trials, with less trials towards the corners of the picture (e.g., Table 2.3). Due to these unequal number of contributions, the signal-to-noise ratio also varies across the image (Table 4.4), but with the exception of very few pixels (four in Table 2.4), all locations satisfy the so-called Rose criterion, namely that in order to distinguish image features reliably, the signal's amplitude must be 4-5 times (12-14 dB) the amplitude of the associated noise (Rose, 1973; Bushberg *et al.*, 2012). Finally, in our spatial images, we excluded the corners of the image from our analyses because there are no observations in these parts of the image (NaN in Table 2.4).

2.6 Supplementary Materials

2.6.1 The sine cardinal (*sinc*) function

The observation that the spatial average over a small-time interval resembles a sinc function in Patients 1-3 is used for the interpretation of the relationship between spatial and temporal STAs. The central part of the reasoning is that, in general, the relationship between a rectangular function and the sinc function (Fig. 2.7) can be written in the form:

$$\text{sinc}(y) \propto \int_{-\infty}^{\infty} \text{rect}(-X, X) e^{jxy} dx \quad (\text{Equation 2.13})$$

Here x, y are a pair of dimensions (e.g. time and space or time and frequency) and $\text{rect}(-X, X)$ is a rectangular function over $(-X, X)$; $j = \sqrt{-1}$.

Based on the definition of the Fourier transform and its inverse, the sinc function and rectangle function are Fourier transform pairs (Boashash, 2016).

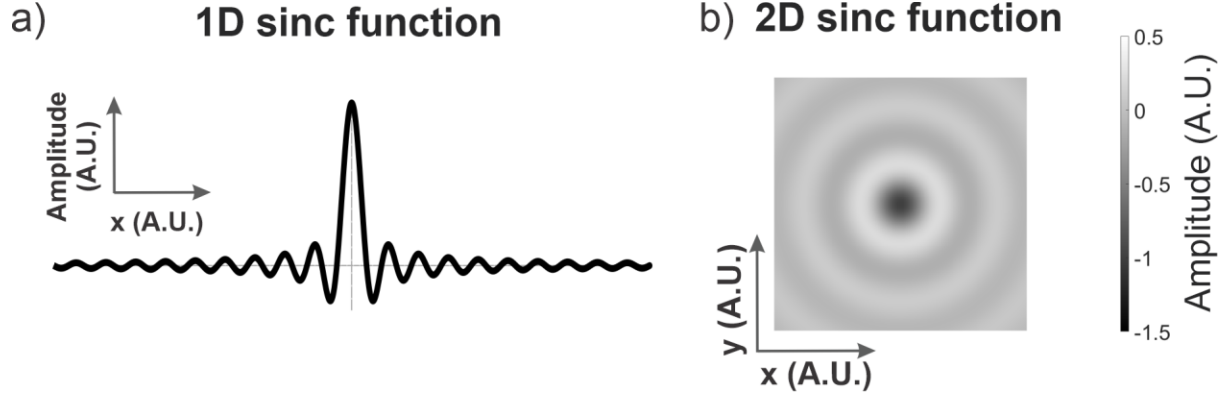


Figure 2.7: Simulated 1-dimensional (D) and 2D sinc functions. **A)** Simulation of a 1D sinc function, $\text{sinc}(x)$. **B)** Top view of a simulated 2D sinc function.

The property in Eq. 2.13 is used to model the spatiotemporal relationship of the electrical activity recorded by a macroelectrode (Fig. 2.1). Because of Eq. 2.13, the spatiotemporal activity function in Fig. 2.1, $f(r, \tau)$ can be approximated by $e^{j r \tau}$. The spatiotemporal symmetry as outlined in the first section of the results follows from this. In summary, in this situation, spatial and temporal aspects of the ongoing activity under the macroelectrode are coupled.

2.5.2 The st-SCA as a unit impulse response

Computation of the spatiotemporal spike-centered average (st-SCA) using ictal recordings presents a challenge because the occurrence of action potentials across a seizing network is not experimentally controlled, unlike the scenario in which the location and timing of the neuronal activities are evoked by external stimuli. The approach as outlined in Eqs. S2-S5 addresses this problem and demonstrates that the st-SCA is spatiotemporal analog of well-known spike-triggered average (STA). For convenience, we repeat here that (x, y, t) are the spatiotemporal components of the signals; (x_i, y_i, t_i) are the spatiotemporal coordinates of spike i and (ξ, ψ, τ) are the spatiotemporal components of the signal relative to the spike. Using a similar approach as in (Eissa *et al.*, 2018), we now extend the model of the ictal network as a linear time invariant (LTI) system with the multi-unit action potential activity as input, the LFP

as its output (note that this LTI system isn't necessarily causal), and the network's unit impulse response (UIR) (see Main Text Eq. 5) defined as the LFP associated with a single unit impulse (δ):

$$UIR = st-SCA = C(\xi, \psi, \tau) \quad (\text{Equation 2.14})$$

We now can recover the network output Z using the convolution of the UIR and the network's input, i.e. the spikes:

$$Z = \iiint C(\xi, \psi, \tau) \left\{ \frac{1}{N} \sum_{i=1}^N \delta(x - x_i - \xi, y - y_i - \psi, t - t_i - \tau) \right\} d\xi d\psi d\tau \quad (\text{Equation 2.15})$$

Note that we used the $\frac{1}{N}$ scaled version of the input here. Plugging in the expression for $C(\xi, \psi, \tau)$ (see Eq. 11) results in:

$$\begin{aligned} Z = \iiint \left\{ \frac{1}{N} \sum_{i=1}^N LFP(x_i + \xi, y_i + \psi, t_i + \tau) \right\} \dots \\ \dots \left\{ \frac{1}{N} \sum_{i=1}^N \delta(x - x_i - \xi, y - y_i - \psi, t - t_i - \tau) \right\} d\xi d\psi d\tau \end{aligned} \quad (\text{Equation 2.16})$$

Exchange of the summation and integration operations and evaluation of the triple integral gives the model's estimate of the spatiotemporal LFP from the LTI system:

$$Z = \frac{1}{N^2} \sum_{i=1}^N \sum_{i=1}^N LFP(x, y, t) = LFP(x, y, t) \quad (\text{Equation 2.17})$$

As shown in (Eissa *et al.*, 2018), the time domain component of this linear estimate produces a close approximation of the ongoing seizure activity with significant correlation ($p < 0.01$) between recorded and estimated activity.

2.5.3 Mechanisms involved in focal seizures

By combining current and previous findings on ictal dynamics, we can outline the following summary for an evolving neocortical focal seizure. At the micro and meso-scales, an ictal wave of action potential activity propagates at a velocity of ~ 1 mm/s by invoking excitation via the local connections over distances < 1 mm. This wave of hyperexcitation propagates locally when the inhibition in front of this wave fails to constrain the excitation (Eissa *et al.*, 2017; Schevon *et al.*, 2012; Tryba *et al.*, 2019). In this context, it is interesting to note that this propagation process seems compatible with the evolution of the clinically observed Jacksonian march first described by Hughlings Jackson in 1870 (Extercatte *et al.*, 2015). We now find evidence that, in addition to the slow propagation process, the ictal wave excites cortical areas farther than 1 mm away, probably via axon collaterals within the gray matter, which allows excitation to ‘escape,’ and enables recruitment of additional cortical territory (Fig. 2.6C). This activation of areas > 1 mm away might also explain modular propagation of ictal activity, a property previously observed in experimental seizures (Trevelyan *et al.*, 2006). At the macroscale, white matter intracortical connections are invoked, spreading ictal activity across a cm-sized territory. The activity in this macroscale territory is still highly correlated with the action potential activity in the ictal wave located in the recruited territory rather than the local action potential activity located in the non-recruited areas (Fig. 2.11) (Eissa *et al.*, 2017). In addition, while local inhibition fails at the ictal wavefront, longer range inhibition remains intact and plays a critical role in sustaining the synchronous oscillatory component of the ongoing seizure at the macroscale (Eissa *et al.*, 2017; Eissa *et al.*, 2018).

2.5.4 Supplemental figures and tables

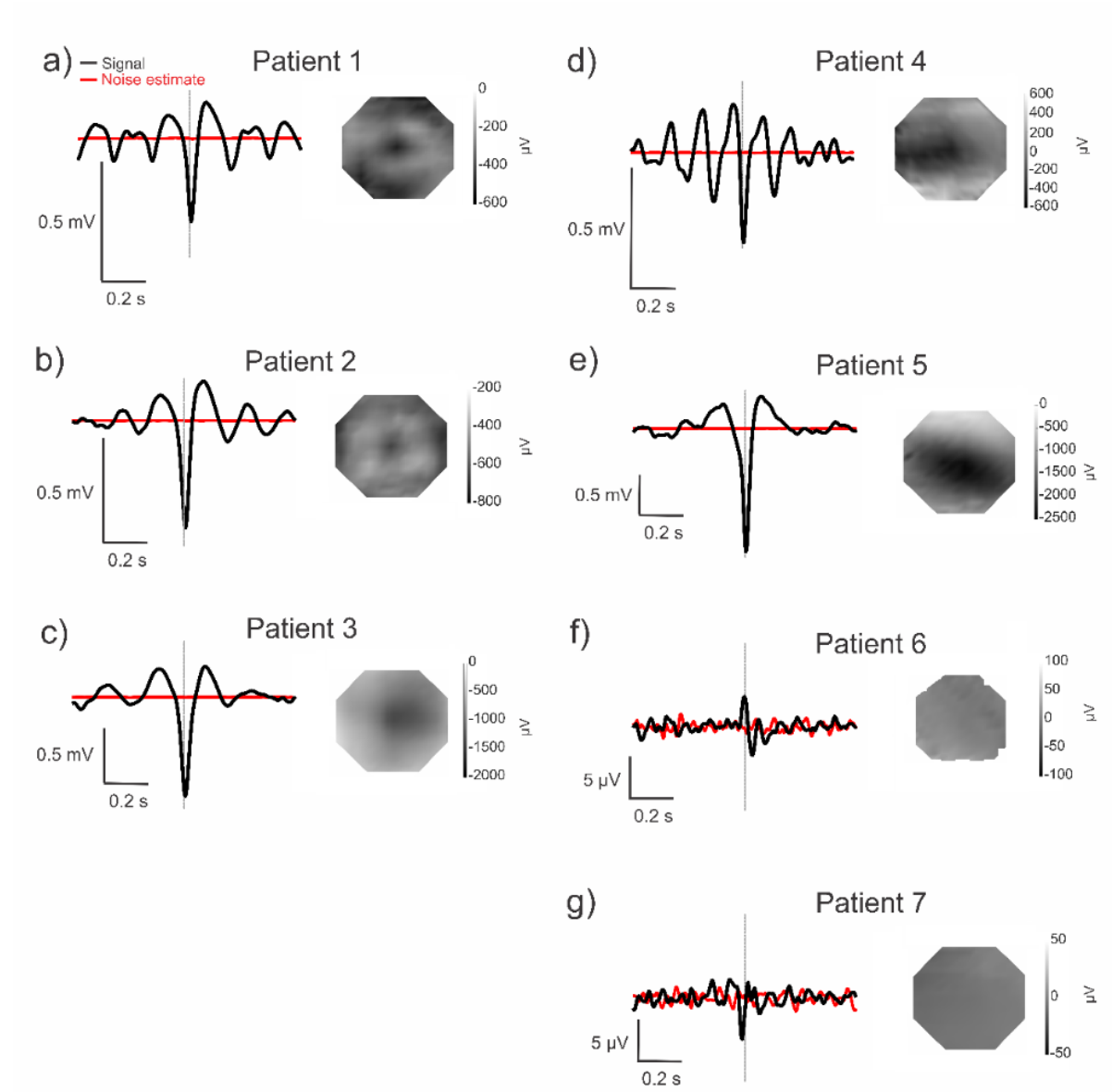


Figure 2.8: Representative st-SCAs for each patient. Patients 1-5 had microelectrode arrays (MEAs) implanted in recruited territory, and Patients 6-7 had MEAs implanted in unrecruited territory. Grayscale is in μV units. **A-B)** Patients 1-3 resemble sinc functions in the temporal and spatial domains. The black traces are the signals, and the red traces are the noise estimates. **D-E)** Patients 4-5 do not resemble sinc functions in the temporal domain and resemble deep wells of in the spatial domain. **F-G)** Patients 6-7 are characterized by comparatively much smaller amplitude signals in both the temporal and spatial components.

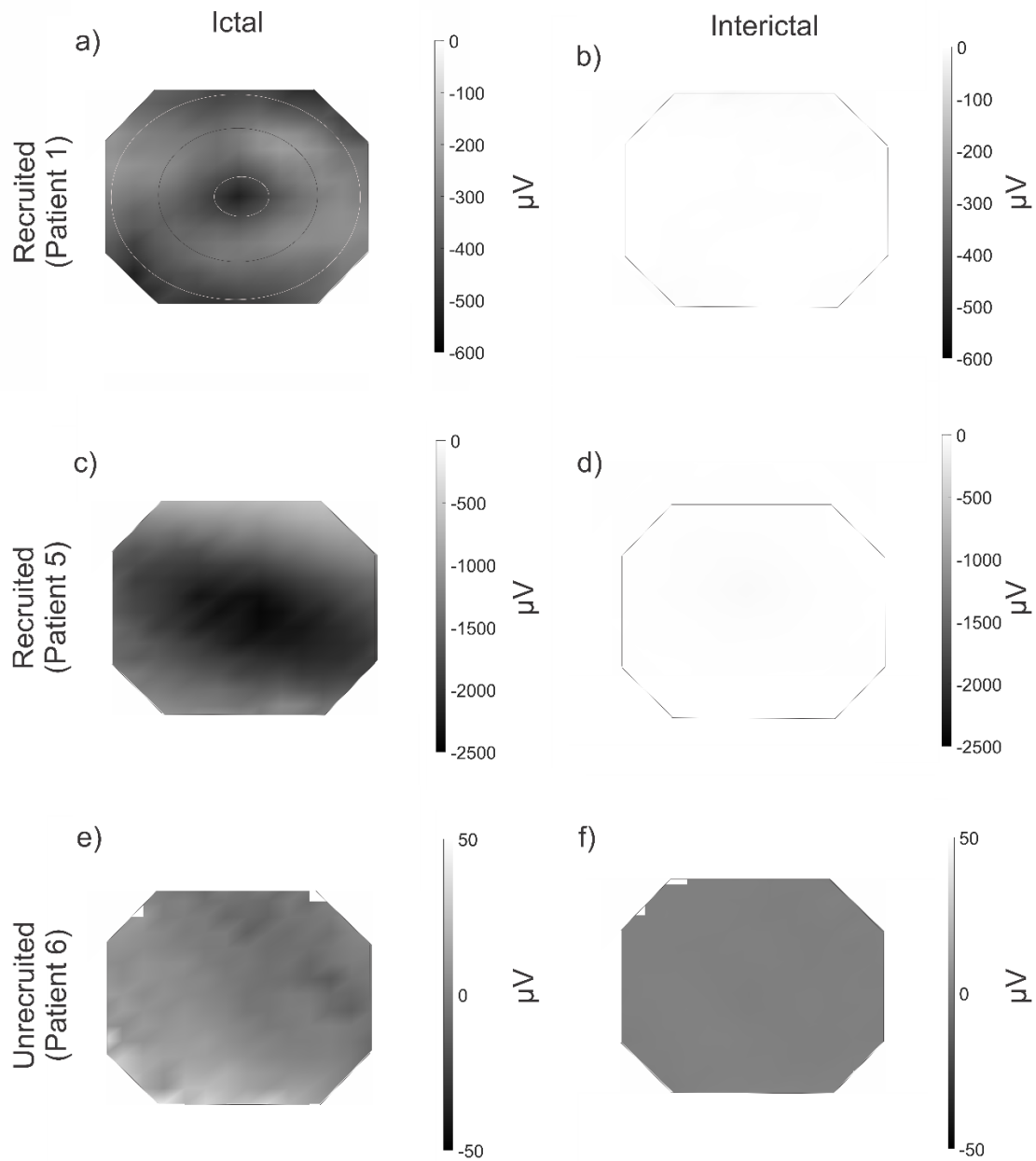
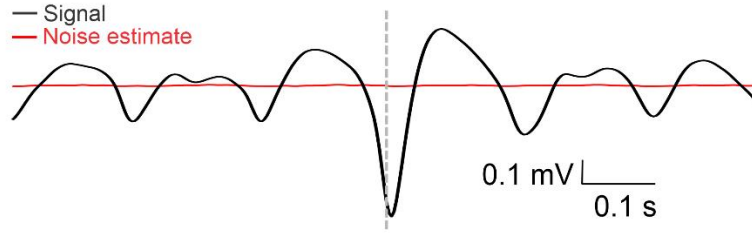
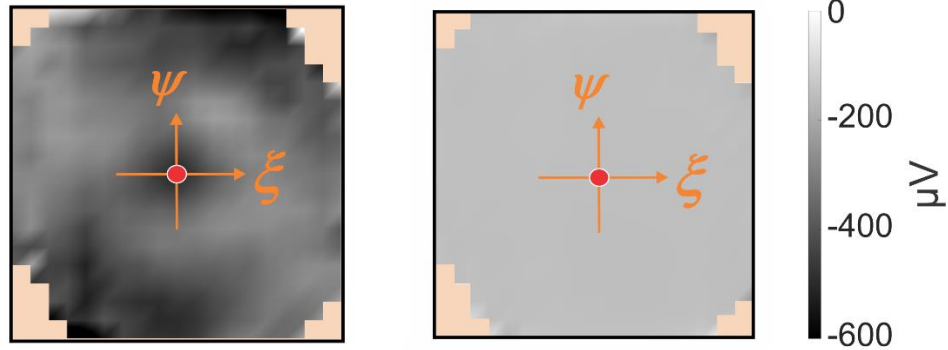


Figure 2.9: Spatial component of the st-SCAs. The st-SCA in panels a and c represent the same spike-LFP relationship as depicted in Fig. 2.4e and f, respectively. In all patients, the ictal signal (a, c, e) is stronger than the interictal one (b, d, f). In Patient 1 (a), the two rings surrounding the center are indicated by the circles. Patient 5 (c) instead shows a deep well of negative activity. The dynamics in unrecruited territories (e-f) are markedly different and are also much smaller in amplitude. Grayscale is in μV units.

a) Detail of the Temporal SCA with its Noise Estimate



b) 3D st-SCA with its Noise Estimate



c) 2D st-SCA with its Noise Estimate

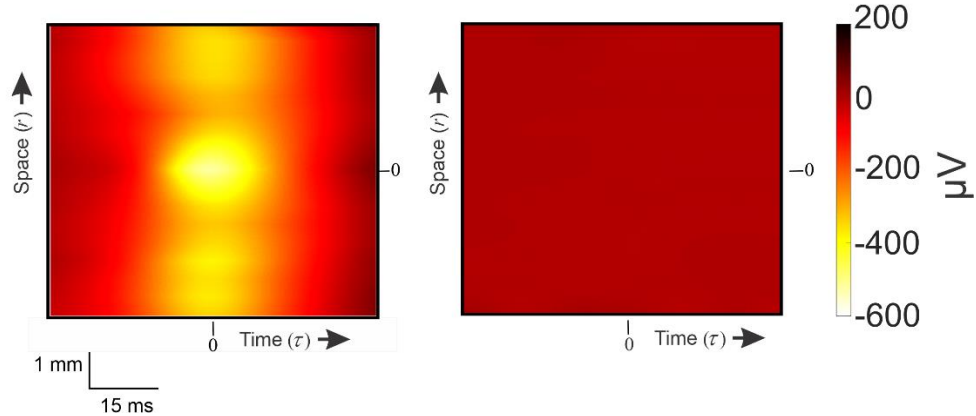


Figure 2.10: Noise estimates of the st-SCA. The SNR of the signals is well above 14dB in each panel (as per application of the so-called five sigma rule). a) Detail of the temporal component of the st-SCA from Fig. 2.4C (black) and its noise estimate (red). The signal-to-noise ratio (SNR) of the depicted data is 45dB. b) The spatial component of the st-SCA depicted in Fig. 2.4E and its estimated noise component. The location specific SNR of the depicted data range is 26 – 80dB, with an average of 38dB. The units for the grayscale are identical for both maps and identical to the scale in Fig. 2.4e, 2.8a, 2.9A. c) The 2D st-SCA from Fig. 2.5C and its noise estimate. The SNR of the depicted data is 39dB. The units for the color scale are identical for both maps and the same as in Fig. 2.5.

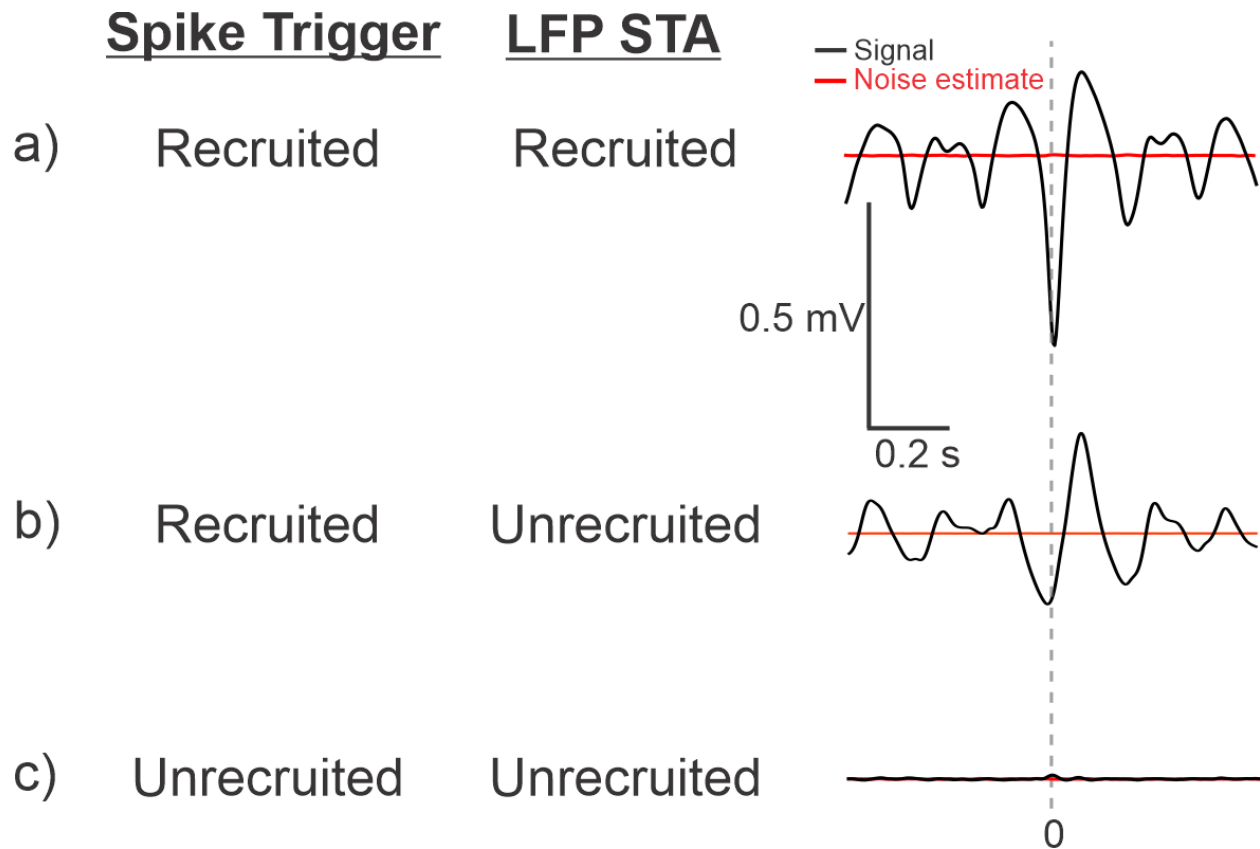


Figure 2.11: STAs based on LFP from recruited & unrecruited territories. The STA of the LFP in the recruited area triggered by spikes in the recruited area (A) show a large negative peak at the time of the trigger. The STA in the unrecruited areas have a relatively strong signal component when triggered by spikes in from the recruited areas (B), but not if triggered by spikes in the unrecruited area (C). The black traces are the signals, and the red traces are the noise estimates.

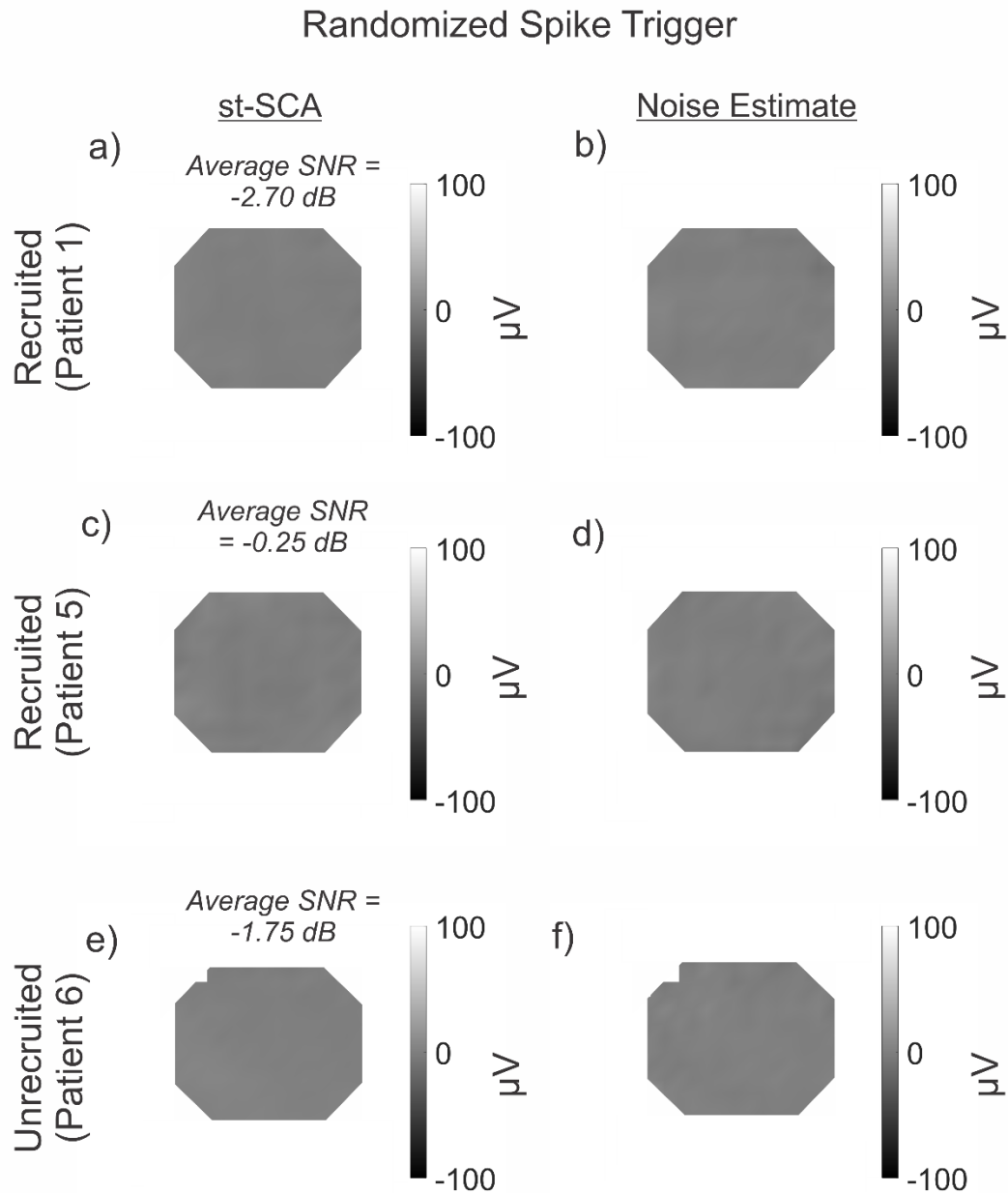


Figure 2.12. Representative st-SCAs after randomizing spike triggers. No spatial patterns are seen, highlighting the importance of spike timing in the st-SCA calculation. Grayscale is in arbitrary units (A.U.). The average signal-to-noise ratios (SNR) are listed per patient.

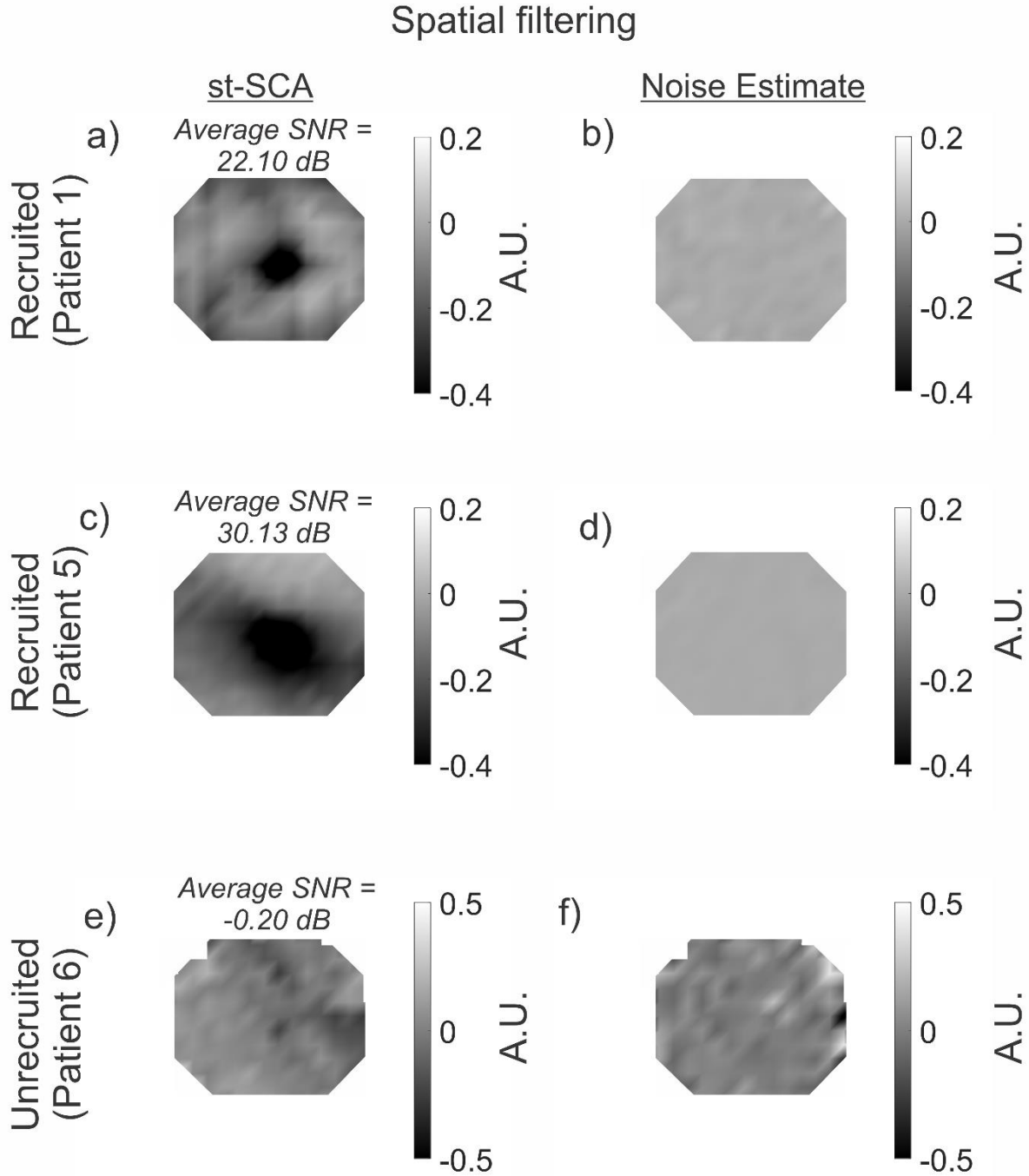


Figure 2.13: Representative st-SCAs after spatial filtering. The spatially filtered st-SCAs resemble similar patterns to non-whitened st-SCAs, albeit a smaller amplitude signal. Grayscale is in arbitrary units (A.U.). The average signal-to-noise ratios (SNR) are listed per patient.

Table 2.1. Patient Table: Demographics and Clinical Features

Patient (age/ sex)	Patient 1 (25yo/F)	Patient 2 (19yo/F)	Patient 3 (21yo/M)	Patient 4 (32yo/M)	Patient 5 (45yo/M)	Patient 6 (30yo/M)	Patient 7 (39yo/M)
Implant location	Left lateral and sub temporal	Right lateral and sub temporal, parietal, occipital	Left lateral frontal, sub frontal, temporal, sub temporal	Left lateral temporal, sub temporal, parietal, frontal	Right lateral temporal, parietal, frontal	Left lateral frontal, mesial frontal, temporal	Left lateral and mesial frontal
MEA location	Left inferior temporal gyrus 2.5 cm from anterior temporal pole	Right posterior temporal, 1 cm inferior to angular gyrus	Left middle temporal gyrus 1–2 cm posterior to the temporal tip	Left superior temporal gyrus	Right superior temporal gyrus	Left supplementary motor area, 3 cm superior to Broca's area	Left lateral frontal 2 cm superior to Broca's area
Seizure onset zone	Left basal/ anterior temporal	Right posterior lateral temporal	Left mesial temporal	Left anterior fronto-temporal	Right anterior temporo-parieto-occipital	Left supplementary motor area	Left frontal operculum (3 × 3-cm cortical area)
No. of seizures	3	1	3	3	3	3	3
Seizure type(s)	Complex partial	Complex partial with secondary generalization	Complex partial	Complex partial	Complex partial with secondary generalization	Complex partial/ tonic	Complex partial

Table 2.2. Patient Table: Seizure Recording and Spike Detection Information

	Epoch Length (sec)	n spikes*	spikes/s*
PATIENT 1			
Interictal	180	7720	43
Seizure 1	58	78479	1353
Seizure 2	80	77788	972
Seizure 3	102	153063	1501
PATIENT 2			
Interictal	180	181116	1006
Seizure 1	29	110896	3824
PATIENT 3			
Interictal	180	16582	92
Seizure 1	52	162707	3129
Seizure 2	88	274656	3121
Seizure 3	57	193733	3399
PATIENT 4			
Interictal**	180	23881	133
Seizure 1	82	385978	4707
Seizure 2	102	366705	3595
Seizure 3	96.23	322148	3348
PATIENT 5			
Interictal	180	52998	294
Seizure 1	102	304058	2981
Seizure 2	101	314402	3113
Seizure 3	73	349189	4783
PATIENT 6			
Interictal	180	24438	136
Seizure 1	12	3471	289
Seizure 2	13	4902	377
Seizure 3	6	1635	273
PATIENT 7			
Seizure 1	20	17157	858
Seizure 2	23	7778	338
Seizure 3	31	7065	228

*Across all channels of the MEA.

**Due to limitations in available recordings, this interictal clip is 12 minutes away from the nearest known ictal activity

Table 2.3. st-SCA contributions per each position for Patient 1.

0	0	0	103	255	820	2455	3733	3820	3843	3843	3740	3588	3023	1388	110	23	0	0
0	0	103	1351	1916	4367	6910	8496	8519	9601	9646	8550	8447	7479	5649	2515	1237	68	0
0	0	1295	2528	5459	8359	12487	14617	17793	19560	21165	20084	17335	17183	14451	9508	4660	2851	45
0	967	3247	5426	6807	11063	16262	18528	21611	24829	25761	25188	22908	21201	19441	15082	10006	5505	1746
871	967	3724	6357	7885	12650	17621	20154	25398	29523	28658	27631	24732	22895	21466	16717	11715	7854	2678
871	3287	9713	13611	15223	20139	25265	27873	34893	37525	34148	31846	27605	24035	21722	18477	14282	9613	2684
3191	8533	14665	18792	21507	26302	32201	35560	45834	48131	45108	38963	32494	29372	26614	23873	17695	12947	2974
5699	11151	19184	22539	25680	32674	39669	45411	56147	60608	52622	48376	40281	36785	29212	24439	18118	14293	3488
7927	12450	21762	26520	30323	38476	46592	52892	65817	71443	62671	54461	49289	39763	34507	26143	19817	12622	6087
9127	13359	22366	27238	30418	39017	48327	56367	65787	78479	63226	57602	48841	43962	33058	30803	19025	13447	5318
9127	13528	21382	27053	29659	35132	46226	53925	60109	64798	55277	51414	46905	39197	32124	27793	17662	9285	4057
9127	13432	19430	24503	29167	34290	37810	45054	51606	60047	50782	46523	44215	37950	29328	24965	13723	5175	2216
8256	13432	19728	23326	25981	28722	31439	40238	40611	48968	39481	36527	32763	25651	22666	18687	11858	2283	2176
8256	12561	15606	19098	23375	27189	29788	35703	36666	40196	30809	29173	24897	21777	13927	12645	8363	3189	1875
5936	9823	13364	20424	21921	25322	29748	36538	31736	32811	27806	24121	22046	18885	14415	11512	7097	1876	6
3428	7113	6394	12652	16398	17789	20958	27735	25045	25668	24040	18424	19431	16942	14840	6899	4921	112	0
1200	4506	4055	5418	8778	12290	14600	19003	15726	16523	17926	16363	11102	9996	6798	3764	1987	0	0
0	1369	2390	2773	3716	5793	7012	10406	11718	9940	9776	8955	7851	4999	2674	113	6	0	0
0	0	169	281	295	592	1213	1283	2152	2089	1977	1963	1666	1045	975	106	0	0	0

Table 2.4. SNR values per each position for Patient 1.

NaN	NaN	NaN	18	29	29	34	40	38	39	38	34	32	29	26	19	3	NaN	NaN
NaN	NaN	17	34	42	44	46	57	54	50	49	50	47	54	56	35	35	19	NaN
NaN	NaN	44	63	41	45	61	62	53	49	41	40	39	41	40	45	36	36	4
NaN	48	74	45	44	58	60	58	39	37	40	40	37	41	46	41	38	36	27
37	40	54	37	45	52	44	55	40	38	38	38	36	38	45	43	35	33	34
35	34	37	38	40	45	46	44	34	35	36	36	36	39	43	40	39	34	36
33	40	41	44	48	48	50	42	37	36	36	36	39	40	65	48	37	40	42
36	38	45	38	44	43	52	46	40	41	41	44	50	42	49	42	40	36	38
53	40	43	43	45	51	62	52	43	46	47	48	46	53	58	46	42	39	41
45	39	48	44	45	51	56	56	46	48	54	55	51	52	41	50	40	46	39
44	43	48	46	47	56	57	53	49	48	44	44	61	42	51	56	43	40	36
47	45	38	42	52	58	42	47	67	48	54	48	46	48	49	44	40	40	33
82	43	39	50	51	44	43	55	43	43	43	39	40	42	42	88	36	36	55
54	38	39	41	44	67	43	57	58	51	51	43	60	51	47	43	45	46	34
38	41	35	44	43	43	65	55	46	42	46	50	62	59	60	50	57	36	4
33	48	41	51	51	55	43	50	68	52	68	44	43	59	46	39	43	35	NaN
27	44	40	37	43	50	49	47	55	63	49	44	49	64	46	48	37	NaN	NaN
NaN	30	37	35	51	36	34	40	44	42	44	53	47	46	46	37	2	NaN	NaN
NaN	NaN	25	33	46	39	32	27	29	27	30	31	29	27	29	51	NaN	NaN	NaN

CHAPTER 3

THIRD-ORDER MOTIFS ARE SUFFICIENT TO FULLY AND UNIQUELY CAPTURE SPATIOTEMPORAL NEURAL NETWORK ACTIVITY¹

3.1 Summary

Neuroscientific analyses balance between capturing the brain's complexity and expressing that complexity in meaningful and understandable ways. Here we present a novel approach that fully characterizes neural network activity and does so by uniquely transforming raw signals into easily interpretable and biologically relevant metrics of network behavior. We first prove that third-order (triple) correlation describes network activity in its entirety using the triple correlation uniqueness theorem. Triple correlation quantifies the relationships among three events separated by spatial and temporal lags, which are triplet motifs. Classifying these motifs by their event sequencing leads to fourteen qualitatively distinct motif classes that embody well-studied network behaviors including synchrony, feedback, feedforward, convergence, and divergence. Within these motif classes, the summed triple correlations provide novel metrics of network behavior, as well as being inclusive of commonly used analyses. We demonstrate the

¹This chapter is reproduced from the following publication under the Creative Commons Attribution 4.0 International License from: Deshpande SS*, Smith GA*, van Drongelen W. Third-order motifs are sufficient to fully and uniquely characterize spatiotemporal neural network activity. *Sci Rep.* 2023 Jan 5;13(1):238. *equal contribution

Link to Creative Commons license: <http://creativecommons.org/licenses/by/4.0/>

Attestation Statement: The work presented in this chapter was a collaborative effort with Graham Smith in the Wim van Drongelen lab. Graham and I contributed equally to both research and authorship and share first-authorship.

Note: For the entirety of this dissertation chapter (unless explicitly noted otherwise), the term “spike” refers to an action potential.

power of this approach on a range of networks with increasingly obscured signals, from ideal noiseless simulations to noisy experimental data. This approach can be easily applied to any recording modality, so existing neural datasets are ripe for reanalysis. Triple correlation is an accessible signal processing tool with a solid theoretical foundation capable of revealing previously elusive information within recordings of neural networks.

3.2 Introduction

Meaningfully capturing the complexity of neural networks is a daunting task: a range of different approaches are currently in use to quantify network behavior (e.g. Abeles and Gerstein, 1988; Dechery and MacLean, 2018; Schneidman *et al.*, 2006; Jiang *et al.*, 2017; Sporns and Kötter, 2004; Jovanović and Rotter, 2016; Milo *et al.*, 2002; Buzsáki and Draguhn, 2004). Intuitively, we assume that completely characterizing this complexity should require correlations of such high-order as to be incomprehensible, perhaps even unenumerable (Yu *et al.*, 2011). However here we show that third-order correlations fully characterize even the most complex neural recordings. This full characterization arises from the unique correspondence between a dataset and its triple correlation, per the triple correlation uniqueness (TCU) theorem. Introduced decades ago in optical sciences (Bartelt *et al.*, 1984), this theorem states that any finite image has unique triple correlation. The TCU theorem has since languished, but we hope to bring triple correlation to the forefront of data analysis with one simple observation: any finite dataset can be interpreted as an "image." In neuroscience, this encompasses any completed recording of neural activity: functional magnetic resonance imaging, local field potential, single-unit electrophysiology, multi-electrode array electrophysiology, voltage-sensitive dye imaging, etc. Beyond these, the TCU theorem applies to any finite dataset in any field.

Here, we bring the TCU theorem into the heart of neuroscience with a focus on analysis of spike rasters as the representation of neuronal population activity. We propose that the activity patterns of a neural network can be ideally characterized by its triple correlation, $c3$. We begin by defining $c3$, which comprises triplet motifs, the relationships among three events. We briefly summarize the proof of the uniqueness of $c3$ and explore the implications of this uniqueness for neural data. We then classify the triplet motifs by event sequencing and neuron recruitment to derive a natural summary of $c3$ in fourteen motif classes. This summary falls out naturally and maps onto network properties of both computational and biological interest, including synchrony, feedback, feedforward, convergence, and divergence. We illustrate the utility of that simple summary with some straightforward simulations and apply our analysis to experimental recordings. In sum, we present a novel, theory-based approach to quantifying network activity.

3.3 Methods

We worked with a multi-neuron raster of spikes (Fig. 3.1A) to outline our approach, though the analysis works the same for any finite dataset (see section A.2.5).

3.3.1 Defining triple correlation

Unlike pairwise correlation (a function of one lag between two spikes), triple correlation characterizes three-way interactions as a function of two lags among three spikes (Fig. 3.1B). We will call C_3 the triple correlation transform, which transforms a spatiotemporal raster into its triple correlation. So for a spatiotemporal raster, $r(n, t)$ (n , *space*; t , *time*) the triple correlation $c3$ is a function of four variables:

$$C_3[r] = c3(n_1, t_1, n_2, t_2) = \langle r(n, t) * r(n + n_1, t + t_1) * r(n + n_2, t + t_2) \rangle_{n, t} \quad (\text{Equation 3.1})$$

The operation $\langle \dots \rangle_{n,t}$ computes the average over all bins in the raster. The argument \dots is 1 when (n, t) is part of a spiking triplet with lags (n_1, t_1, n_2, t_2) , and 0 otherwise. In practice, we only calculate the triple correlation up to a certain maximum spatiotemporal lag which we determine based on experimental and computational considerations on a per-experiment basis (noted in each figure). In most cases calculating the full $c3$ would be a needless computational expense as usually the triple correlations with longer lags become more likely to be dominated by chance. See subsection A.2.4 "Computing the triple correlation" for implementation details.

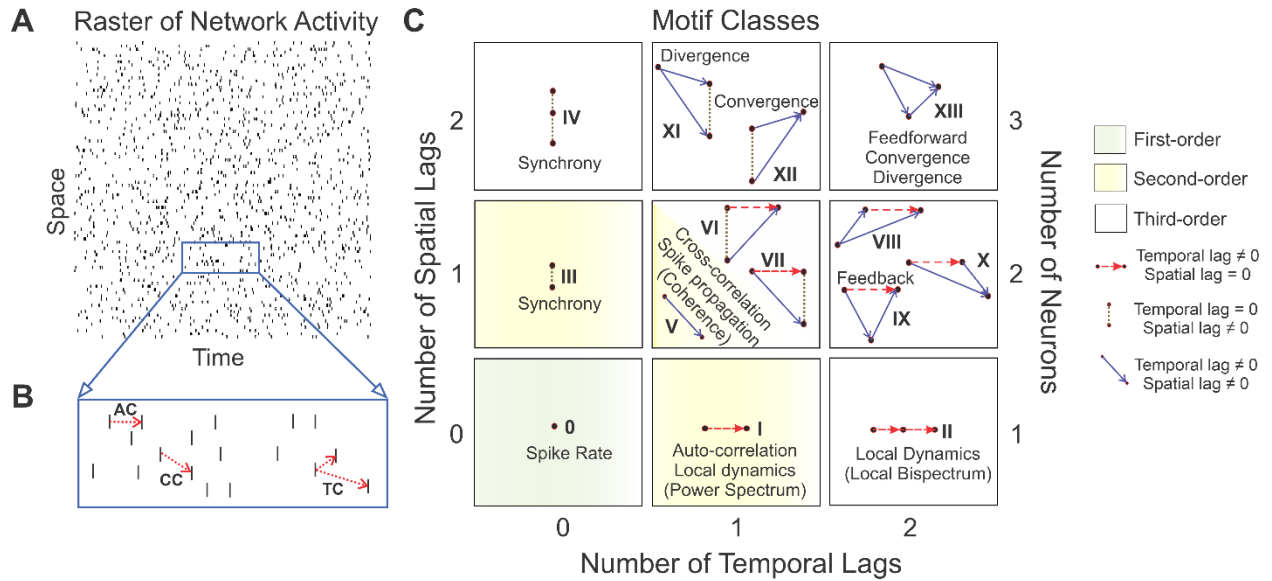


Figure 3.1: Application of the fourteen motif classes to spike rasters. For a given raster (Panel A), second- order correlations can relate activity within a neuron (auto-correlation, AC; Panel B) or between neurons (cross- correlation, CC; Panel B). Triple correlation (TC; Panel B) relates three bins, separated by up to two temporal and two spatial lags. Three particular spike bins constitute a triplet motif (e.g. as shown in Panel B). We classify these motifs into fourteen motif classes by the motif's spike sequence (Panel C; see section A.2.5 for a complete derivation). Dot: a single spike bin. Horizontal red dashed arrow: intraneuronal spike bins, i.e. space lag= 0, e.g. I and II. Vertical stippled line: synchronous spike bins, i.e. time lag = 0, e.g. III and IV. Solid blue arrow: interneuronal spike bins (e.g. V). These 14 motif classes can also embody well-known neuronal processing properties (such as synchrony, feedback, convergence, divergence, and feedforward) in both the time (listed adjacent to the motif class) and frequency domains (listed within parentheses). First- (0) and second-order (I, III, and V) motif classes are highlighted in green and yellow, respectively. The second-order motif classes I, III, and V are constituent motif classes that comprise the third-order motifs. The remaining ones are third-order motif classes.

3.3.2 Overview of uniqueness proof

To prove uniqueness, we apply the Triple Correlation Uniqueness (TCU) theorem, originally applied in optical sciences (Bartelt *et al.*, 1984; Yellott and Iverson, 1992; Yellott, 1993). It states that if we have two images x and y with equal triple correlations ($C_3[x] = C_3[y]$), then the images themselves must be equal ($x = y$). The TCU theorem applies to any finite bounded dataset, including continuous signals and multi-dimensional data—a fact that can be understood by interpreting any dataset as an image—so we apply it to a spike raster. We begin with two rasters x and y whose triple correlations are equal. This implies that the triple correlations' Fourier transforms (bispectra) are equal, which we can write as equality between the product of three characteristic functions. Characteristic functions are the Fourier transform of probability distributions and are well-known in statistics to have certain nice properties (Feller, 1950). Using those properties, we perform simple algebraic manipulations of that equality to derive that the Fourier transform of x equals the Fourier transform of y times an exponential function, $F[x](\sigma) = F[y](\sigma)e^{ja\sigma}$, where σ is frequency, j is the imaginary number, and a is some constant. This means that raster x equals raster y translated by some constant a . Thus, rasters with equal triple correlations are themselves equal up to translation. See section A.2 for the full proof, both in the two dimensions of a typical raster and in the fully general N dimensions. Because of this result, spiking activity can in principle be recovered in its entirety from triple correlation (see "Reconstruction Algorithms for Finite Images" in Yellott and Iverson, 1992).

3.3.3 Summarizing triple correlation with motif classes

To better interpret triple correlation, we summarized it along lines meaningful to the underlying neural dynamics, combining the motifs into qualitatively distinct motif classes, M_i .

To do this, we asked what differences between three-spike motifs constitute fundamental differences. First, we grouped motifs according to whether their lags are zero or non-zero, producing $2^4 = 16$ groups for the four spatiotemporal lags. Next, we distinguished within these groups according to the signs of the lags, which expanded those 16 groupings into 169 lag-sign motifs (proven in subsection 3.5.6 "The number of lag-sign motifs"; enumerated in Table 3.1). These 169 lag-sign motifs enumerate all possible shapes of the motifs where the identity of each node matters, and where space is ordered. However, for our purposes many of these shapes are functionally the same. For example, we only distinguished between zero and non-zero spatial lags: zero meaning "intra-neuronal" and non-zero meaning "inter-neuronal." Further, node identity is irrelevant. Using these considerations, we grouped together these 169 lag-sign motifs according to those invariant under reflecting over the horizontal axis and node identity permutation. As a result, we found fourteen motif classes (Fig. 3.1C; proven in subsection 3.5.7 "The number of motif classes").

3.3.4 Controlling for expected contributions

When using motif classes to quantify network patterns, it is essential to distinguish between the occurrence of these motif classes due to underlying network behavior versus due to chance. Based on simple combinatorics, we expect contributions for each motif class to differ by orders of magnitude. For example, motif classes I and III each have only one varying lag, whereas motif class XIII has four. So, if λ is the maximum lag between spikes in a motif, the expected contributions of motif classes I and III are $O(\lambda)$, while the expected contribution of motif class XIII is $O(\lambda^4)$. Intuitively, we also expect the motif class contributions to vary depending on the number of spikes required in the motif: while there are more motifs in motif class XIII, the chances of any one of them occurring is lower than motif class I because a motif

needs three spikes for motif class XIII but only two for motif class I. So given a fixed spike rate p , we calculated the theoretically expected motif class contributions under the simplifying assumption that every neuron is a Poisson process with rate p per bin: $E[M_i | p, \lambda] = NT \#(M_i | \lambda) p^{n_i}$, where NT is the size of the raster, $\#(M_i | \lambda)$ is the number of motifs given maximum lags λ , and n_i is the number of events in a motif in motif class i . (See subsection A.2.8 "Expected contributions per motif class" for case-by-case calculation)

We note that the higher-order motifs are composed of lower-order motifs, e.g. looking at motif class X in Fig. 3.1C, it is constructed of two kinds of arrows: those of motif classes I and V. We say that motif classes I and V are constituent motif classes of motif class X (see also Fig. 3.4 for more explicitly deconstructed examples). We want to control also for this dependency. By computing the expected relationship between the contribution of a higher-order motif class and the contributions of its lower-order constituent motif classes, we derived $E_c[M_i]$ which is the expected motif-class contributions given a spike rate and controlling for lower-order constituent motif-class contributions (constituent-controlled expectation). For lower order motifs, this is the same (e.g. $E_c[M_I] = E[M_I]$), but for higher order motifs this reflects the expected contribution in a raster of Poisson processes with the observed contributions of its constituent motifs, i.e.

$E_c[M_X] \approx E[M_X | M_I M_Y]$,. We report $\left(\frac{M_i}{E_c}\right) - 1$ so that positive values indicate higher contribution than expected, negative indicate less, and zero indicates contributions in line with those expected due to noise and the observed lower-order constituent motif-class contributions.

3.4 Results

Our principal goal is to bring triple correlation into general usage, with the triple correlation uniqueness theorem providing theoretical foundation for its use. Since triple correlation is entirely untested in the field, we approached it as we would any new tool: we

showed that it works in the simplest possible case, before adding noise and testing it across the whole gamut of possible patterns. After these checks, we applied triple correlation to open-source real-world data.

3.4.1 Application of triple correlation summary

For a simple example to test this approach, we simulated a network spike raster with synchronous, periodic firing at a frequency of $f = 0.08$ arbitrary units (Fig. 3.2A). From this raster, we determined contributions of all motif classes by summing the raster's triple correlation across all motifs in each motif ($M = \{M_i\}$, where $\{M_i\} = \sum c3(m)$ for motifs m in motif class i). We also simulated rate-matched pure-noise rasters (Fig. 3.2B) as surrogates and calculated their motif-class contributions. These surrogates were simulated Poisson processes with identical firing rates for every neuron. In addition, we calculated a theoretical value, the constituent-controlled expectation (μ_c ; see Methods). We plotted all three quantities for each motif class (Fig. 3.2C). These quantities on their own are difficult to read: any difference between motif classes is completely overshadowed by the inevitable combinatorial differences in the number of triplet motifs per motif class. To account for these expected combinatorics and effectively report the contribution of each motif class, we calculated the constituent-controlled ratio ($\left(\frac{M}{\mu_c}\right) - 1$; Fig. 3.2D), which highlights the deviation of each motif-class contribution from that expected due to noise and lower-order constituent motif class contributions. To demonstrate that the contributions from surrogate rasters do not differ much from the constituent-controlled expectation, we plotted the estimated-to-constituent-controlled ratio $\left(\frac{\hat{\mu}}{\mu_c}\right) - 1$ for all $n = 100$ surrogate rasters (Fig. 3.2E).

We see that our summary of the triple correlation reflects the simple underlying structure: motif-classes III and IV, which correspond purely to neural synchrony, are highest above the

expected contributions. Motif-classes VI, VII, XI, and XII, which each includes a synchronous component, are also above chance expectations (Fig. 3.2D). Thus, as a single facet of our analysis, we can detect not only second-order synchrony (motif class III), which is considered important in neuroscience research (Roscoe *et al.*, 1985; Kreuz *et al.*, 2011, 2013), but also third-order synchrony (motif class IV). We recognize that this is an ideal case, in which the synchronicity is also visibly apparent from the raster itself. We will now proceed to show that this particular detection works in the face of noise, and that all the other facets of our analysis (i.e. the other motif classes) also work.

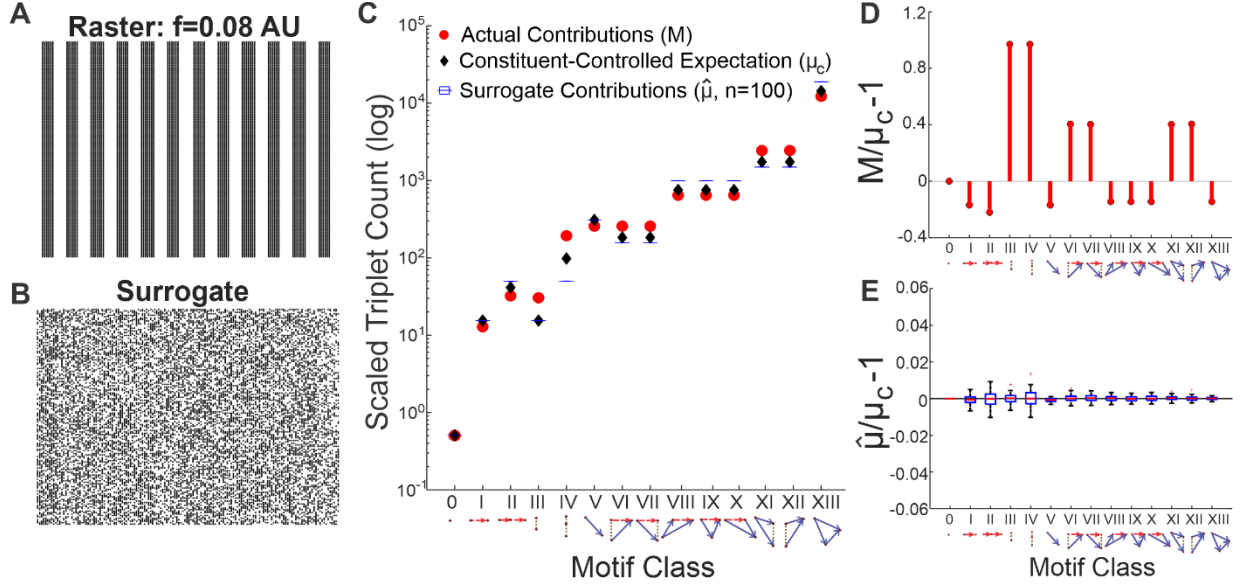


Figure 3.2: Motif-class contributions to the raster's triple correlation. **A)** 150 x 150 spike raster generated by thresholding an 0.08 AU frequency sine wave. **B)** Surrogate raster generated by randomly shuffling the periodic raster in panel A. **C)** Various motif-class summary metrics calculated from a triple correlation using lags up to 20 bins in time and space: the actual contributions per motif class (M , red circles); the constituent-controlled theoretically expected contributions (μ_c , black diamond) conditioning on spike rate and controlling for the observed contributions of lower-order motifs; surrogate contributions (μ_c , blue boxplots visible as horizontal lines due to relatively small variance) the average motif-class contributions across $n = 100$ shuffled surrogate rasters. **D)** The constituent-controlled ratios ($M/\mu_c - 1$) per motif class. $M/\mu_c - 1$ for purely synchronous motif classes III and IV are highest; motif classes VI, VII, XI, and XII (which all consist of an element of synchrony) also show positive $M/\mu_c - 1$ values. Note that motif class 0 always has zero signal because motif class 0 is the spike rate, which is controlled for by both N and T . **E)** The estimated-to-constituent-controlled ratios ($\hat{\mu}/\mu_c - 1$) for 100 noise simulations fluctuate around 0 for all motif classes and are shown as box-and-whisker plots. The centerline is the median, the bottom and top edges of the box are the first and third quartiles, and the whiskers extend to the minimum and maximum values.

3.4.2 Resistance to noise

We explored the effects of increasing noise on detecting network structure using faster synchronous firing with added uniform noise input ($f = 0.12$ AU, SNR = 0 dB; Fig. 3.3A). Similar to the results of those with slower synchronous firing (Fig. 3.2D), motif classes III, IV, VI, VII, XI, and XII (those with elements of synchrony) are found more often than chance (Fig.

2.3B). We increased noise (SNR = -9dB; Fig. 3.3C), resulting in lower magnitude signals across all motif classes, yet still detecting synchronous signals (Fig. 3.3D). In this case, the underlying network structure is still overtly present in the raster. We then increased the noise such that the synchronous network structure in the raster is not overtly present (SNR = -17 dB; Fig. 3.3) and found that while all signals move even closer to 0, those with synchrony are still elevated (Fig. 3.3F). Thus, triple correlation reflects underlying structure in the face of added noise. Finally, we show that in an extremely noisy raster (SNR = -40dB; Fig. 3.3G), the synchronous signals are no longer detected as all motif classes now show even lower magnitude signals, approaching 0 (Fig. 3.3H). In this overwhelmingly noisy simulation, the motif-class spectrum is dominated by chance.

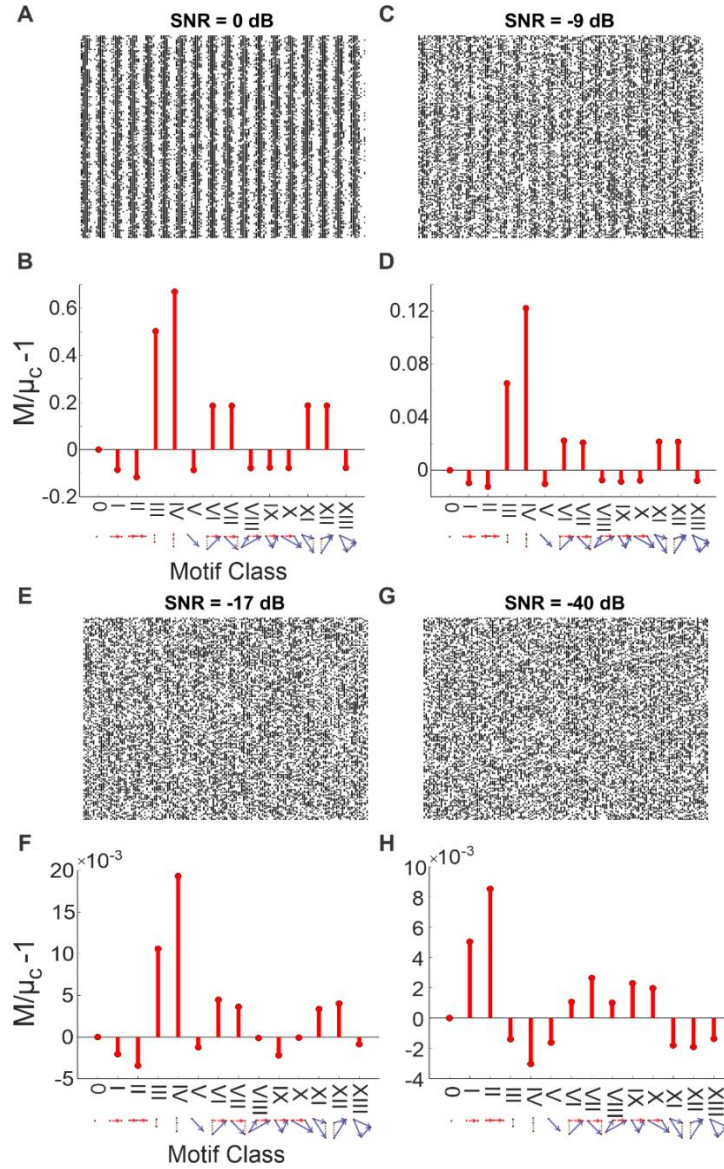


Figure 3.3: Detecting synchrony amidst increasing noise. **A)** The 150x150 spike raster plot is generated by thresholding a 0.12 AU frequency sine wave with added noise. The noise consists of uniform noise scaled to give the desired signal-to-noise ratio (SNR = 0 dB). **B)** The motif-class contributions (M) of the above raster relative to chance ($M/\mu_c - 1$). These were calculated from a triple correlation using lags up to 14 bins in time and space. These values show increased contributions of motif classes with synchronous elements, as expected. **C)** The periodic signal is embedded in more noise (SNR = -9 dB), albeit still visible from the raster. **D)** Same as panel B with lower magnitude signals. **E)** The synchronous structure is embedded in more noise (SNR = -17 dB), but now not overtly apparent to the naked eye. **F)** Same as panels B) and D) with lower magnitude signals. All motif-class contributions are closer to 0, but motif classes with synchronous elements are still detected. **G)** The synchronous structure is now embedded in extreme noise (SNR = -40 dB). **H)** Same as panels (B, D, and F), but now other motif-class signals are also detected (and not just those with synchronous elements) due to chance. All motif classes have even lower magnitude signals, approaching pure noise.

3.4.3 Detecting various spiking sequences

Next, we tested that our method correctly detects various isolated spike sequences (triplets). Our approach correctly detected third-order motifs by the appropriate motif class. We illustrate six simulations, each including only one repeated triplet across the raster. In addition to motif class 0, all motif classes are composed of one or more constituent motif classes (I, III, and/or V). Of the simulations depicted, the first three show triplets whose motif classes are purely composed of a single constituent motif class (Fig. 3.4A-C), and the other three show motif classes composed of a mix of two different constituent motifs (Fig. 3.4D-F). Fig. 3.4A-C show that the second- and third- order motifs for local dynamics (Fig. 3.4A; I & II), synchrony (Fig. 3.4B; III & IV), and feedforward (Fig. 3.4C; V & XIII) are correctly detected. Note that motif class V (simple second-order cross-correlation, which we describe as "spike propagation") is in fact a constituent part of every third-order motif other than those in motif classes II and IV, and so was detected at lower levels in every subsequent test. Fig. 3.4D-F shows the other three cases: feedback (IX; composed of I and V), divergence (XI; composed of III and V), and convergence (XII; composed of III and V).

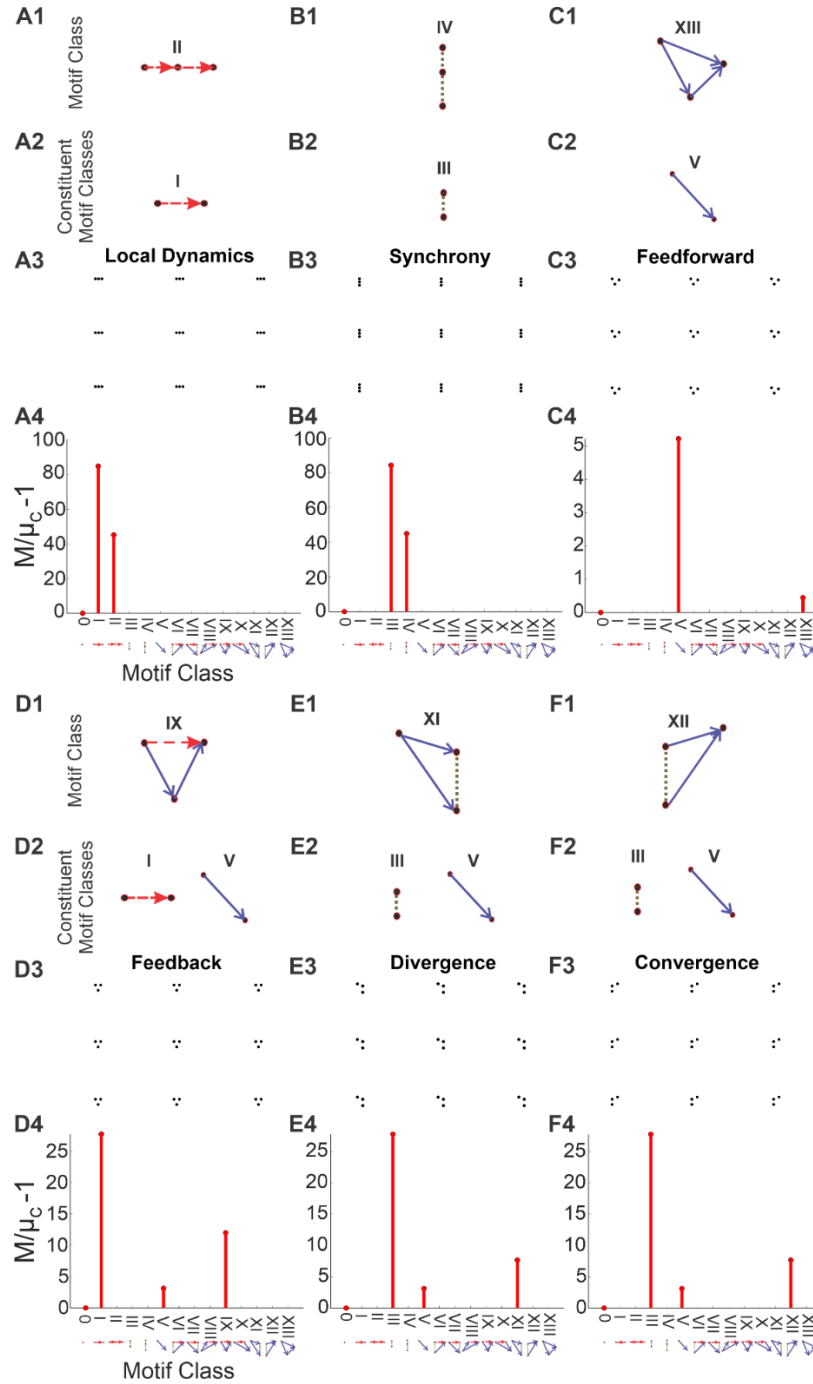


Figure 3.4: Detecting motif classes in individual patterns. We simulated 150 x 150 rasters, each consisting of a single repeated triplet. Row 1: the motif class of the repeated triplet. Row 2: the motif class' constituent motif classes. Row 3: the simulated raster. Row 4: the motif-class contributions ($M/\mu_c - 1$) calculated from the row 3 raster's triple correlation, using lags of up to 14 bins (which is less than the separation between motifs in the raster). In all cases, the highest-order motif with a non-zero contribution is the motif class, and the remaining non-zero contributions are the constituent motif classes. Note the changing y-axis scale: motif classes I and III are far less likely to occur from chance than motif class V.

In every case, including those not depicted, the tested triplets were reflected by the correct motif-class contribution (along with the triplets' constituent parts). For example, a feedback triplet elevates the contribution from motif-class IX, along with contributions from motif-classes I and V, which together constitute motif-class IX (Fig. 3.4D). Note that the particular summary used in this approach does not depend on quantitative details. Because of this, our detector works purely on 1) the qualitative spike sequencing that defines the motif-class, and 2) the presence of that motif class anywhere within the raster.

3.4.4 Application to experimental data

We further tested our approach using open-source, publicly available network data recorded from rat cortical cultures (details of this dataset are described in Hyvarinen *et al.*, (2019) and obtained from Kapucu *et al.*, (2022)). Briefly, rat cortical neurons were cultured in microelectrode array (MEA) well plates consisting of 16 (4x4 array) electrodes. Data were collected at 22 days *in vitro*. The datasets consisted of already-detected spike time data from baseline wells (n = 35 wells) and from wells treated with the following pharmacological agents (n = 35 wells):

1. Control (n=7 wells)
2. γ -aminobutyric acid (GABA, 10 μ M, n=7 wells)
3. 6-cyano-7-nitroquinoxaline-2,3-dione (CNQX, 50 μ M, n=7 wells), an amino-3- hydroxy-5-methyl-4-isoxazolepropionic acid (AMPA)/kainate receptor antagonist
4. D-(-)-2-amino-5-phosphonopentanoic acid (D-AP5, 50 μ M, n=7 wells), which is an N-methyl-D-aspartate (NMDA) receptor antagonist
5. Gabazine (30 μ M, n=7 wells), a GABA_A receptor antagonist

The raw data were sampled at 12,500 samples/channel, and the spikes were detected by the researchers as described in Kapucu *et al.*, (2022). We downsampled the spike rasters to 500 samples/channel. Where multiple spikes were occasionally binned together, we counted them as a single spike. Representative 1-minute snippets of each raster per condition are depicted in Figure 3.6. We computed the triple correlation for each well of the MEA plate with temporal lags of -50ms:50ms and spatial lags that cover the entirety of the dataset in each of the two dimensions of the 4x4 array. We first show that the results from the triple correlation approach to quantify spike rate (contributions of motif class 0, Fig. 3.5A) concur with the results reported in Hyvarinen *et al.*, (2019) (their Fig. 7C). Then for each pair of baseline and treatment wells, we calculated the ratio between $M/\mu_c - 1$ for the treatment well over the baseline well and reported these values with a boxplot for each treatment (Fig. 3.5B-D). In these box-and-whisker plots, the center line represents the median (50th percentile), the bottom and top edges of the box represent the first (25th percentile) and third (75th percentile) quartiles, the whiskers represent the minimum and maximum range of data not considered outliers, and individual data points outside of the box-and-whisker plot represent outliers.

The drugs used in this study provide specific levers to control synaptic activity: GABA increases and gabazine decreases inhibitory synaptic function; CNQX blocks faster excitatory synapses (AMPA/kainate); and D-AP5 blocks slower excitatory synapses (NMDA). These have broadly straightforward effects on the network's firing rate: potentiating inhibitory synapses or blocking excitatory synapses decreases the firing rate, while blocking inhibitory synapses increases the firing rate (Fig. 3.5A; Hyvarinen *et al.*, (2019)) Modulating the inhibitory synapses has a similar gross effect: excess inhibition suppresses contributions throughout, while decreasing inhibition leads to an increase in structured firing across the motif-class spectrum

(Fig. 3.5B). When antagonizing particular excitatory receptors-with either faster or slower post-synaptic potentials-the triple correlation reflects changes in network behavior beyond simple firing rate modulation. On top of the gross reduction in firing, antagonizing faster excitatory AMPA/kainate receptors results in a decrease in synchrony and (most) higher-order motifs involving synchrony (Fig. 3.5C). On the other hand, antagonizing slower excitatory NMDA synapses, creating a network in which excitation is governed by faster synapses, results in a marked increase across the motif-class spectrum, despite the overall reduction in activity. The particularly high prevalence of third-order synchrony (motif class IV) reflects the fact that the remaining firing is overwhelmingly synchronous, well above the expectation governed by chance (Fig. 3.5D, Fig. 3.6). These results agree with the connectivity graphs comparing faster and slower correlations in AMPA and NMDA networks (Suresh *et al.*, 2016, their Fig. 9).

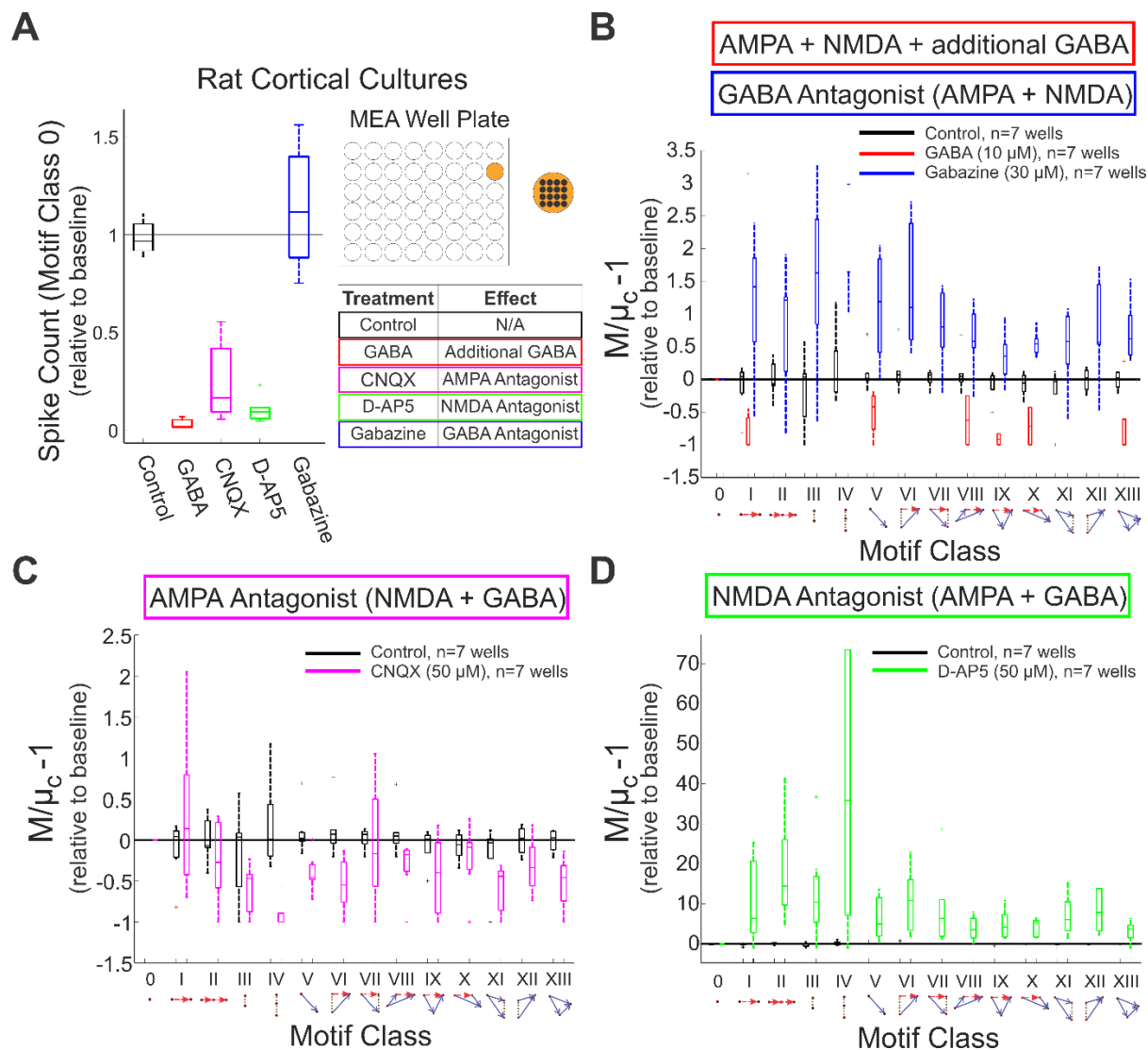


Figure 3.5: Application of the triple correlation approach to experimental data. We determined motif-class contributions in an open-source dataset of rat cortical cultures. Networks (n=70 wells; n=35 baseline and n=35 treated) were cultured on microelectrode array (MEA) well plates—each well configured with 4x4 electrodes. The treated wells were exposed to the following experimental conditions (n=7 wells per condition): control (black), GABA (red), gabazine (blue), CNQX (magenta), and D-AP5 (green). Each treatment well was matched to an untreated baseline well. For each motif class, we depict the distribution of ratios between the treatment and baseline wells. In these box-and-whisker plots, the centerline is the median, the bottom and top edges of the box are the first and third quartiles, and the whiskers extend to the minimum and maximum values. **A)** The normalized spike counts relative to baseline (contributions of motif class 0) are shown for each experimental condition. The table shows the effect of each of the experimental conditions. **B)** $M/\mu_c - 1$ values are shown for control-, GABA-, and gabazine-treated cultures. Note that some motif classes (IV, VI, VII, XI, XII) do not show values for GABA treatment due to lack of spiking. **C)** Results for control- and CNQX-treated cultures. **D)** The motif-class spectra for control and D-AP5-treated cultures indicate increased network structure for the latter, while its level of activity was reduced (Panel A).

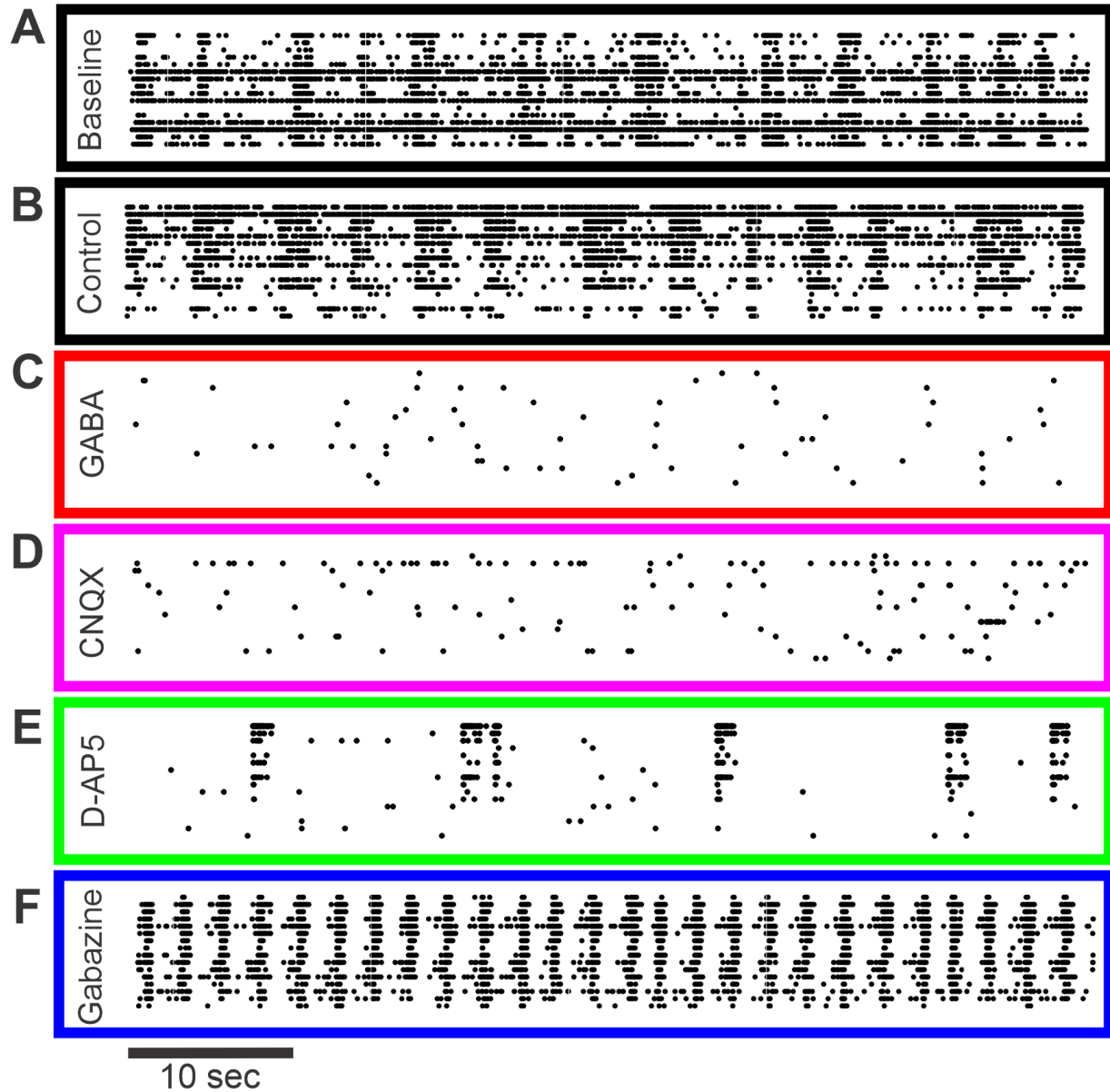


Figure 3.6: Representative 1-min epochs of rat cortical spike rasters. Rat cortical cultures from microelectrode array well plates were exposed to the following pharmacological agents: baseline (A; black), control (B; black), GABA (C; red), CNQX (D; magenta), D-AP5 (E; green), and gabazine (F; blue). Note that we present the raster in two dimensions here while in our analysis for Fig. 3.5 we used the two spatial dimensions of the MEA and one temporal dimension.

3.5 Discussion

The essence of this study is the introduction of a new analytical tool that fully characterizes network activity using triplet motifs. Our mathematically unique statistical analysis

not only encompasses typical first- and second-order analyses (e.g. auto-correlation, cross-correlation; Fig. 3.1), but also includes third-order correlations that are reflective of nonlinear network behaviors. In the preceding section, we demonstrated the robustness of our approach with networks of escalating complexity: in a simple synchronous test case (Fig. 3.2), in the face of substantial noise (Fig. 3.3), and in an experimental dataset (Fig. 3.5). We also validated our simple summary metric in response to all computationally relevant motif classes (Fig. 3.4). The beauty of this approach lies in its flexible application to a multitude of finite data sets, including spike raster plots, fMRI images, local field potential (LFP), electroencephalogram (EEG), and data analyses in many other disciplines. Thus, we are excited to introduce this new analytical approach and eagerly anticipate its use as a tool to uncover new insights into network behavior.

Historically, neural network activity has been an important topic of investigation (McCulloch and Pitts, 1943). Hebb's foundational idea of cell assemblies, which aimed to link physiology and function (Hebb, 1949), have often been investigated by searching for repeated patterns of spiking. Typically, these cell assemblies are investigated in the context of searching for multispikes pattern activation that may not be time-locked to any external stimulus or action, as "would be the case for internal processes like recalling a memory or planning a movement" (Abeles and Gerstein, 1988). The field has expanded considerably over the decades, fostering research in precise zero-phase lag synchronization (Abeles, 1991; Singer, 1999; Russo and Durstewitz, 2017), temporally-coded sequential patterns (Skaggs and McNaughton, 1996; Buzsaki and Draguhn, 2004), and synfire chain-like structures (Abeles, 1982; Hertz and Prügel-Bennett, 1996; Diesmann *et al.*, 1999; Ikegaya *et al.*, 2004). Our approach builds on this active area of research by integrating across multiple patterns within spatiotemporal motifs. Much as multispikes patterns are putatively reflective of cell assemblies, these spatiotemporal motifs are

potentially reflective of underlying structure, and thus, changes in structure could be indicative of network state shift, for example: the transition between normal and seizure states (Jirsa *et al.*, 2014), preparation-to-movement in monkeys (Riehle *et al.*, 1997), sleep/wake states (Saper *et al.*, 2010), or neuromodulation in response to pharmacological agents (Iorio *et al.*, 2013).

When applying our approach to investigate a particular hypothesis, there are two critical questions that should be asked: 1) what choice of spatiotemporal lags is relevant for the dataset (e.g. are there *a priori* synaptically relevant temporal lags?); and 2) depending on the null hypothesis, what choice of method for random chance firing is best suited for the dataset? The former presents an exciting and unexplored frontier that allows researchers to tailor this approach to a variety of hypotheses. The latter can be informed by prior literature either on null hypothesis distributions (to calculate theoretical expectations) or surrogate generation (to estimate the same). In order to present a foundational concept, we used Poisson processes to model our neurons, both in theory and in surrogate datasets. For future applications, when testing specific hypotheses using experimental data, a more nuanced surrogate (e.g. Stella *et al.*, (2022); Baker and Lemon (2000); Grun (2009)) should be used: e.g. a stimulated neuron will not obey a simple Poisson process. Thus, the particular surrogate would depend on the hypothesis being tested and must match the null hypothesis.

Among signal processing tools, a prominent example of another unique transform of neural data is the Fourier transform, with amplitudes and phases of frequencies as fundamental units (van Drongelen, 2018). Much of medical imaging relies on the uniqueness of the Fourier transform, including computerized tomography (CT) and magnetic resonance imaging (MRI), which uses the Fourier transform to generate images (van Drongelen, 2018). In EEG and LFP research, application of Fourier transform has progressed our understanding based in the

frequency spectrum (van Drongelen, 2018). Since triple correlation also constitutes a unique characterization of neural data, we present our approach as a more complex yet still useful tool, as it is not only nonlinear and higher-order, but also comprises fundamental units, triplet motifs, that are still intuitively informative. Analogous to the typical summary of the Fourier transform's frequency spectrum into frequency bands (alpha, beta, gamma, etc.), we summarize the triple correlation's motifs into a spectrum of fourteen motif classes. However, unlike the EEG frequency bands, which depend on clinically defined ranges, the motif-class spectrum arises directly from theory and is purely derived from possible spike sequences. It is a natural summary, and the classes themselves reflect their parsimony: they distinguish fundamental properties of computation, such as synchrony (motif classes III and IV), feedback (motif class IX), etc. (Fig. 3.1C). Furthermore, the constituent motif classes (I, III, and V) capture the well-known second-order correlations in analyzing neural spike data. Thus, while there are many alternative summaries, ours is both natural and useful in quantifying activity patterns (as exemplified in Figs. 3.2-3.5). Curiously, these theoretically defined fundamental units agree with previously data-driven work that has pointed to the primacy of third-order network motifs (Bojanek *et al.*, 2020; Dechery and MacLean, 2018; Schneidman *et al.*, 2006; Jiang *et al.*, 2017).

Not only is triple correlation unique in the time domain, but its own Fourier transform, the bispectrum, is unique in the frequency domain. The bispectrum of the spike raster includes the well-known power spectrum and cross-spectrum (and coherence), the Fourier transform of autocorrelation (I) and cross-correlation (V) respectively for binary data (e.g. van Drongelen, 2018). The bispectrum's uniqueness gives theoretical weight to the growing consensus among researchers that insights about neural signals are encoded in the bispectrum (Bou Assi *et al.*, 2018; Gagliano *et al.*, 2019). Specifically, this underscores the importance of the fundamental

elements of the bispectrum, which are the relationships between frequencies' amplitudes and phases. In some cases, as in our simulated rasters (Figs. 3.2-3.4), the spatial frequencies may not be relevant due to the arbitrary ordering of neuron rows in the rasters. In other cases, where the spatial dimension has a real ordering (e.g. our MEA dataset; Fig. 3.5) the spatial frequency bands can be an untapped source of insight.

Both triplet motifs and inter-frequency analyses are already important topics of investigation in neuroscience (e.g. Jovanovic and Rotter, 2016; Milo *et al.*, 2002; Bojanek *et al.*, 2020; Dechery and MacLean, 2018; Sporns and Kotter, 2004; Jansen *et al.*, 2021). Here, we have provided a direct avenue for these investigations and proven the fundamental importance of these topics to any spatiotemporal neural data. Furthermore, the success of using the bispectrum as an input to artificial neural network seizure classifiers (Bou Assi *et al.*, 2018) suggests that the equivalently unique and also-meaningful triple correlation might also prove a good feature space on which to train machine learning algorithms. While we applied triple correlation to simulated and experimental spiking activity, our methodology can extend beyond spike rasters to even higher dimensionality rasters and to continuous-valued signals, such as multi-electrode LFP data or EEG recordings (see proof section "Proof in Online Materials"). Ultimately, just as frequency bands have been considered fundamental components of brain activity with Fourier transform, here we propose triplet motifs as new fundamental building blocks, one step more complex, that hold promise as an innovative approach to analyzing spatiotemporal neural activity across the breadth of recording modalities.

CHAPTER 4

INSIGHTS INTO NEURAL NETWORK BEHAVIOR USING 4D ENTROPY: A NOVEL QUANTITATIVE METRIC OF NETWORK ACTIVITY BASED ON TRIPLE CORRELATION¹

4.1 Summary

The human brain comprises an intricate web of connections, which in sum, generate complex neural networks capable of storing and processing information. This information depends on multiple factors, including underlying network structure, connectivity, and interactions; and thus, methods to characterize neural networks typically aim to unravel and interpret a combination of these factors. We have previously shown that third-order motifs are sufficient to characterize neural network activity fully and uniquely from the Triple Correlation Uniqueness (TCU) theorem (Deshpande *et al.*, 2023). Triple correlation relates three nodes separated by up to four spatiotemporal lags (n_1 , n_2 , t_1 , & t_2), generating fourteen qualitatively distinct motif classes (Deshpande *et al.*, 2023). Here, we build from this approach to develop a method to compute the 4D entropy from the spatiotemporal lag probability distribution function (PDF). Given a spike² raster, we compute the triple correlation by iterating over time and space, and if a three-node configuration (motif) is found, we store the spatiotemporal lag combination that determined that motif. Counting the frequency of these motifs over each of the lags

¹This chapter builds from the following abstract that will be presented at the 32nd Annual Computational Neuroscience (CNS) conference in July 2023:

Deshpande SS, Smith GA, van Drongelen W. *Computing PDFs and Entropy from Triple Correlation: Insights into Neural Network Behavior*. 32nd Annual Computational Neuroscience Meeting. 15-19 July 2023; Leipzig, Germany.

²Note: For the entirety of this dissertation chapter (unless explicitly noted otherwise), the term “spike” refers to an action potential.

generates a spatiotemporal lag distribution, from which we estimate a PDF and compute the 4D entropy. We first simulate isolated feedforward motif-class patterns to validate our approach. We then apply this methodology to spiking activity recorded from rat cortical cultures to measure functional connectivity over time and compare our results to previously published results of pairwise (2D) correlated entropy over time (days *in vitro* (DIV)). From 2-35 DIV, the following triple correlation metrics demonstrate comparable trends to the published pairwise 2D entropy: spike rate (motif class 0), second-order spike propagation (motif class V; cross-correlation), and feedforward motifs (motif class XIII). However, the 4D entropy computation reveals a greater depth of underlying network organization. While the published 2D entropy values decrease from 31-35 DIV, the 4D entropy values do not show this decrease, but instead plateau. The difference between 4D entropy and published 2D entropy highlights the enhanced value of 4D entropy, which is derived from triple correlation, to capture overall network activity. As such, first- and second-order metrics (e.g. spike rate, CorSE, and cross-correlation) do not fully capture the network dynamics reflected in the 4D entropy and the motif-class spectrum.

4.2 Introduction

4.2.1 Methods to characterize neural networks

Network characterization is an important frontier in neuroscience, evolving rapidly to further uncover information hidden within the brain. Currently, there are multiple methods to characterize neural networks, and they typically do so by analyzing network dynamics and structure. Commonly utilized techniques in neuroscience include: (1) network topology & graph theory analysis, (2) functional connectivity analysis, and (3) information theory. These techniques are not necessarily mutually exclusive and are often employed together to

characterize networks (e.g. functional connectivity analyses can involve network topology, graph theory, and information theory approaches).

Network topology and *graph theory* approaches aim to characterize networks based on their underlying structure (using nodes and edges) and employ metrics such as clustering coefficient and average path length to provide insights into organization of network connectivity (Sporns & Zwi, 2004; Rubinov & Sporns, 2010). Clustering coefficient quantifies the extent to which nodes tend to group together (Watts & Strogatz, 1998); as such, a high clustering coefficient would indicate that the nodes are densely connected and form localized communities (Watts & Strogatz, 1998). The average path length quantifies the number of steps required to travel between two nodes and is determined by the average of all the shortest connections between each pair of nodes (Sporns & Tononi, 2000). One notable property used for these investigations is small-world networks (Watts & Strogatz, 1998), which are characterized by both high clustering and short path lengths (indicating rapid communication pathways which allow for efficient information processing) (Watts & Strogatz, 1998). Small-world characteristics have also been used to investigate anatomical and functional connectivity of the brain (Bassett & Bullmore, 2006; Bullmore & Sporns, 2009). In addition to clustering coefficient and average path length, other network properties utilized in graph theory approaches include degree centrality and rich-club organization. Degree centrality measures the number of connections for a node within the network; a high degree centrality indicates a node with multiple connections, which may act as a “hub” or a crucial brain region for information processing (Sporns *et al.*, 2000; van den Heuvel & Sporns, 2011). Building from this, rich club organization indicates that brain regions with high degree centrality form densely connected hubs, allowing for rapid information flow among brain regions (van den Heuvel & Sporns, 2011; Mišić *et al.*, 2014).

These metrics, as employed by network topology and graph theory approaches, analyze information processing in terms of underlying network architecture.

Functional connectivity analyses involve untangling the temporal correlations and statistical dependencies between populations of neurons or brain regions (Friston, 1994; Lang *et al.*, 2012). These methods investigate interactions among brain regions to decipher information flow and processing, identify regions of coordinated activity, and assess the strength of underlying network architecture. Researchers have investigated functional connectivity under different states, such as resting-state (evaluating spontaneous neural activity in the absence of external input) (Biswal *et al.*, 1995) and task- or state-based cases (assessing how network behaviors change in response to specific tasks or stimulation) (Cole *et al.*, 2014).

Information theory methods quantify the amount of information contained within the network and typically employ metrics such as entropy and mutual information to do so (Shannon, 1948; Rieke *et al.*, 1997). The goal of information theory is to assess how information is encoded and decoded (Panzeri, 1999). Shannon’s entropy, as described in his consequential paper “A Mathematical Theory of Communication,” is a metric of the amount of uncertainty contained in a probability distribution function (PDF) (Shannon, 1948). Shannon’s entropy is defined as:

$$H(x) = - \sum_{i=1}^n p_i(x) \log_2 [p_i(x)] \quad (\text{Equation 4.1})$$

where p_i is the PDF, x is a discrete variable, and \log_2 is the base-2 logarithm (Shannon, 1948).

This measurement has since become a crucial element of information theory with applications to multiple fields, including computer science, economics, and biology. In addition, Shannon’s entropy has been used as a powerful tool in neuroscience, with respect to investigating neural information coding (Quiroga *et al.*, 2004; Quiroga & Panzeri, 2009), functional connectivity

(Sporns *et al.*, 2000; Friston *et al.*, 2003; Pereda *et al.*, 2005), complexity (Tognoli *et al.*, 2014), neural variability (Masquelier, 2017), and information flow (Kaminski *et al.*, 1991; Tewarie *et al.*, 2016).

4.2.2 Overview of triple correlation approach

Triple correlation is a signal processing tool that relates three nodes: one reference node and up to two other nodes separated by up to two lags in both space (n_1 & n_2) and time (t_1 & t_2). Given a spike raster (Fig 4.1A, taken from Deshpande *et al.*, 2023), $r(n, t)$, where n is space and t is time, triple correlation (c_3) is defined as:

$$c_3(n_1, t_1, n_2, t_2) = \langle r(n, t) * r(n + n_1, t + t_1) * r(n + n_2, t + t_2) \rangle_{n,t} \quad (\text{Equation 4.2})$$

This generates 169 possible three-node (motif) configurations (Fig. 4.1B, taken from Deshpande *et al.*, 2023). These 169 motif configurations can be collapsed into fourteen qualitatively distinct motif classes based on symmetries that occur in time and space (Fig. 4.1C, taken from Deshpande *et al.*, 2023). From Panel C of Fig. 4.1, these motif classes can embody well-studied neuronal processing properties, such as synchrony (motif classes III-IV), feedback (motif class IX), divergence (motif class XI), convergence (motif class XII), and feedforward (motif class XIII). We have previously developed a metric of quantifying network structure using triple correlation: $\left(\frac{M}{\mu_c}\right) - 1$, in which M is the prevalence of motif classes and μ_c is the conditioned theoretical expectation value which takes into account the prevalence of first-order (motif class 0: spike rate; green highlighted box in Fig. 4.1C) and second-order motif classes (motif class I: autocorrelation; motif class III: synchrony; and motif class V: cross correlation; yellow highlighted areas in Fig. 4.1C) (Deshpande *et al.*, 2023). For example, computing μ_c for motif class VI is based on the prevalences of motif classes 0, I, III, and V (as motif class VI is

comprised of each of these lower-order classes). Hence, values of $\left(\frac{M}{\mu_c}\right) - 1$ greater than 0 indicate the presence of network structure whereas values of $\left(\frac{M}{\mu_c}\right) - 1$ less than 0 indicate network activity comparable to chance levels. Network activity across each of these fourteen motif classes is termed the motif-class spectrum.

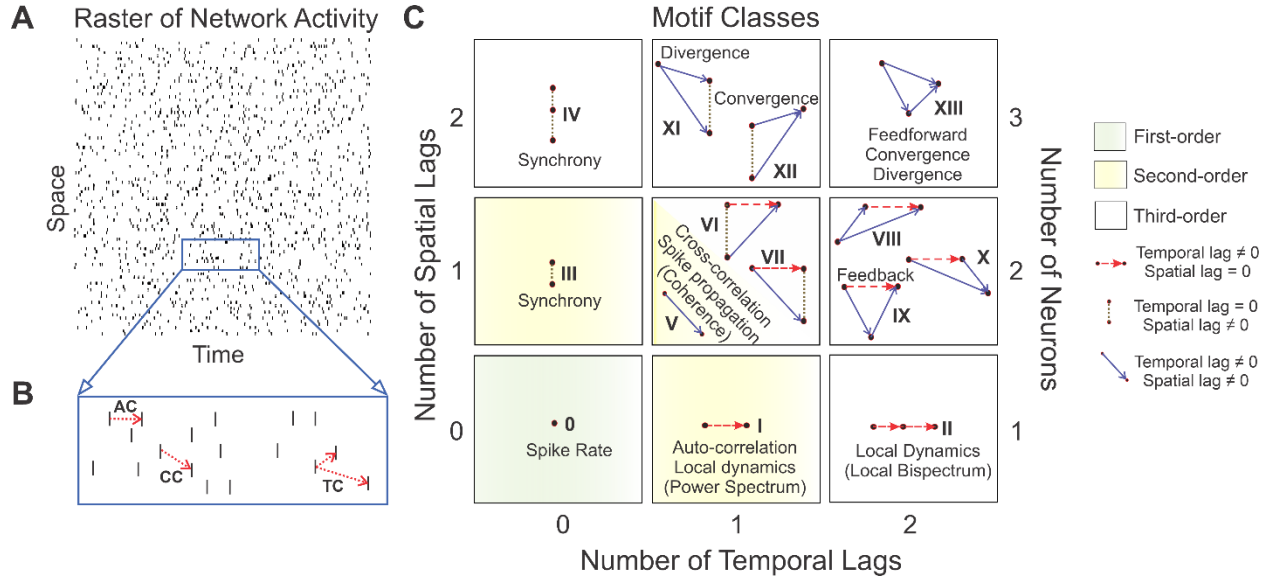


Figure 4.1 (from Deshpande *et al.*, 2023): The fourteen motif classes from triple correlation. **A)** Given a spike raster, **B)** autocorrelation (AC) relates two nodes separated by one temporal lag, cross-correlation (CC) relates two nodes separated by one spatial and one temporal lag, and triple correlation (TC) relates three nodes separated by up to two spatial and two temporal lags. These three-node configurations can be collapsed into **C)** fourteen motif classes which can embody well-studied neuronal processing properties. *This figure is also presented in Chapter 3 (Fig. 3.1) of this dissertation.*

4.3 Methods

4.3.1 Estimating 4D PDF and computing the 4D entropy

Here, we build from the triple correlation approach and compute the entropy of a network from its spatiotemporal lag distribution. Given a spike raster (Fig. 4.2A), we compute the triple correlation by iterating through each spatial and temporal lag. If the triple correlation is nonzero

(e.g. if a motif configuration is found) in the raster, we store the spatial and temporal lag combination that determined that configuration. After iterating over the entire raster, we count the frequency of spatial and temporal lag combinations, generating a four dimensional (4D) spatiotemporal lag distribution (n_1, n_2, t_1, t_2). From this distribution, we estimate a 4D probability distribution function (PDF; Fig. 4.2B). We can generate the marginal PDFs by summing the PDF over each lag variable (n_1, n_2, t_1, t_2), which results in a marginal PDF of the remaining three lag variables; doing so for each lag variable combination generates four marginal PDFs. The PDF of the product of the marginal distributions (Fig. 4.2C) can be useful for analysis as it provides insight into the independence of the discrete variables. Following a similar procedure, we can also generate a PDF for a spike-rate matched surrogate (or noise) raster (Fig. 4.2D-E; $n=100$ iterations), in which the events of the raster are shuffled over time and space. Lastly, we can generate a PDF of a uniform distribution, in which all values of the PDF are equal (Fig. 4.1F). From these 4 PDFs (Panel B: the network PDF; Panel C: the product of the marginal distributions; Panel D: mean surrogate PDF; and Panel E: uniform PDF), we can compute Shannon's entropy (Panel G). Note that for purely visualization purposes, we show a 2D PDF (one spatial lag and one temporal lag) in Panels B, C, E, and F of Fig. 4.2, whereas the PDF and associated entropy from the spatiotemporal lag distribution is four dimensional. From Panel G, the entropy of the feedforward network is lowest, as expected, given the isolated motif class network structure. The entropy of the product of the marginal distribution is higher, but not as high as the entropy of the uniform distribution, which is defined by maximal entropy as all events are decorrelated. The entropy generated from the surrogate distribution is higher than that of the raster, but not equivalent to that of the uniform distribution, suggesting that the surrogate raster does not decorrelate all events. Comparing the entropy of the raster to that of the product

of the marginal distributions provides insight into the statistical independence of the variables. This ideal simulated raster of isolated feedforward motifs (Fig. 4.2A) was used to validate our methodology. We then sought to test this approach on real-world experimental dataset.

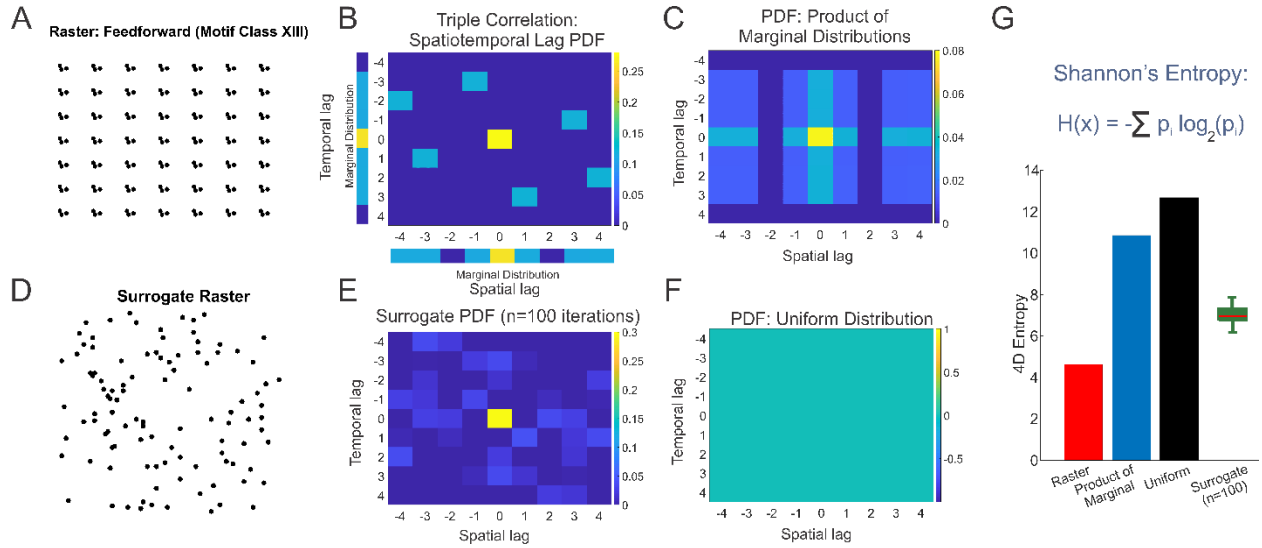


Figure 4.2: Overview of method to compute PDF and entropy. **A)** Given a spike raster of isolated feedforward motif class patterns, we compute triple correlation across the spike raster and **B)** generate a probability distribution function (PDF). From this PDF, we take the sum across each lag, generating a marginal probability distribution for each dimension, shown in the margins of Panel B. **C)** If the PDF of the product of the marginal distributions is equal to the PDF of the network, it suggests that the discrete variables (the lags in this case) are statistically independent. **D)** A spike-rate matched surrogate (noise) raster can be generated by shuffling the spikes across time and space, generating **E)** a mean surrogate PDF (n=100 iterations) using a similar protocol. **F)** The PDF of a uniform distribution is one in which all elements are equal. **G)** From each of these PDFs, Shannon's entropy can be computed. Note that the entropy of the feedforward raster is the lowest value, the entropy of the product of the marginal distributions is higher, and the entropy of the uniform distribution is the maximum (by definition). In addition, we can appreciate that the entropy of the surrogate distribution is not equivalent to that of the uniform distribution, which suggests that the surrogate distribution does not decorrelate all elements of the network.

4.4 Results

4.4.1 Rat cortical cultures: 4D entropy and motif-class spectrum over time

We then applied our approach to an open-source dataset of spiking activity from microelectrode array recordings of rat cortical neurons (Hyvärinen *et al.*, 2017; Kapucu *et al.*, 2022). Briefly, cortical tissue was extracted from rat embryos (embryonic days 17-18) and plated on MEA well plates (12 wells per plate; 8x8 array of 64 electrodes per well) (Hyvärinen *et al.*, 2017; Kapucu *et al.*, 2022). Spiking activity was recorded from 2-35 days *in vitro* (DIV). Triple correlation was computed across the spike raster using spatial lags that cover all 64 electrodes and temporal lags from -50 ms:50 ms. This temporal window of 100 ms covers monosynaptic excitatory (AMPA- & peak of NMDA-mediated) postsynaptic potentials and inhibitory (GABA_A- & GABA_B-mediated) postsynaptic potentials. The published spike rate (Fig. 4.3A), the spike rate computed by triple correlation (Fig. 4.3B), the published pairwise (2D) correlated spectral entropy (CorSE) (Fig. 4.3C), and the prevalence of motif class V (a pairwise, 2D metric of spike propagation) (Fig. 4.3D) show similar trends in that the activity gradually increases, peaks around 24-28 DIV, and decreases from 31-35 DIV. Following the procedure described in Section 4.3.1, the spatiotemporal lag PDF and associated 4D entropy (Fig. 4.3E) were computed using triple correlation, which also yielded the fourteen individual motif-class profiles (Fig. 4.3F). The 4D entropy (Fig. 4.3E) shows a plateau from 31-35 DIV, instead of a decrease in values, as observed by the trends in the first-order and second-order metrics (Fig. 4.3A-D). Furthermore, several third-order motifs (motif classes II and VII) show an overall increase across time, instead of a peak around 24-28 and a slight decrease around 31-35 DIV (as shown by the remaining motif classes except for motif class VI) (Fig. 4.4).

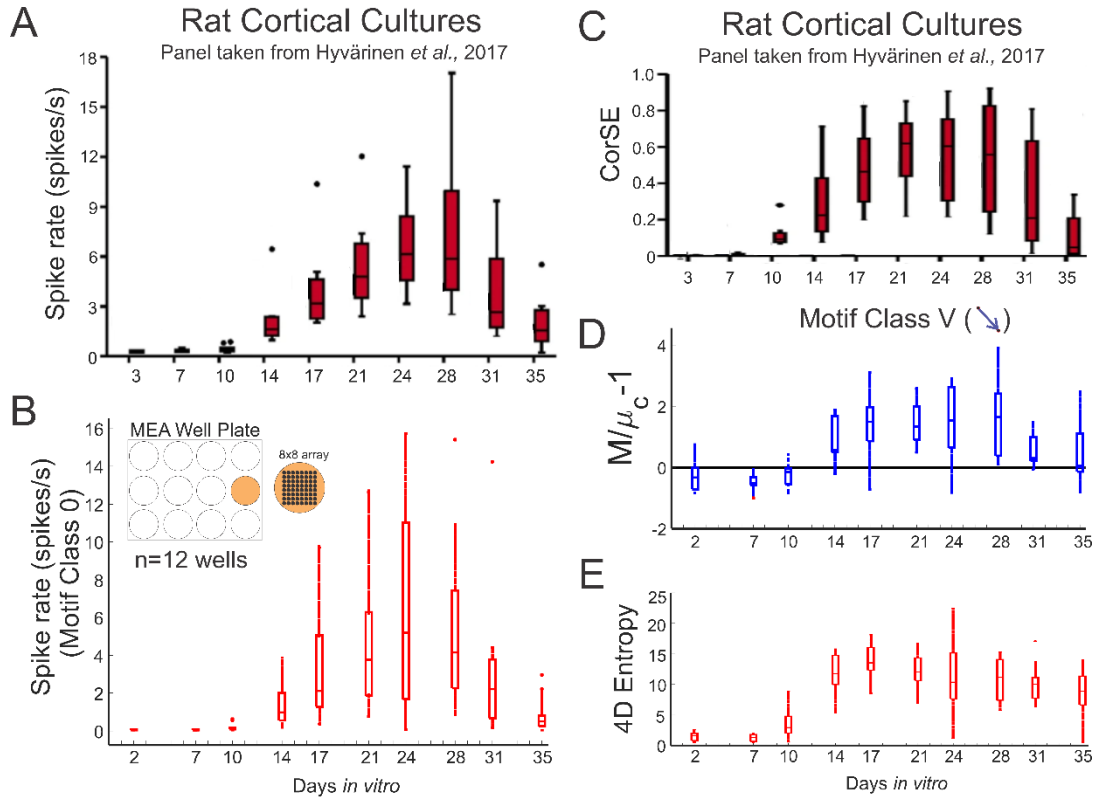


Figure 4.3: Characterizing network activity of rat cortical cultures over time. **A)** The spike rate from the published data (**B**) and triple correlation (motif class 0) show similar trends from 2-35 days *in vitro* (DIV) to that of the published pairwise 2D correlated spectral entropy (CorSE) as well as (**D**) the prevalence of motif class V (pairwise 2D spike propagation). **E)** The 4D entropy computation based on triple correlation shows a comparable trend from 2-28 DIV but plateaus from 31-35 DIV, even though the spike rate (**A-B**) and second-order pairwise metrics (**C-D**) show a decrease from 31-35 DIV.

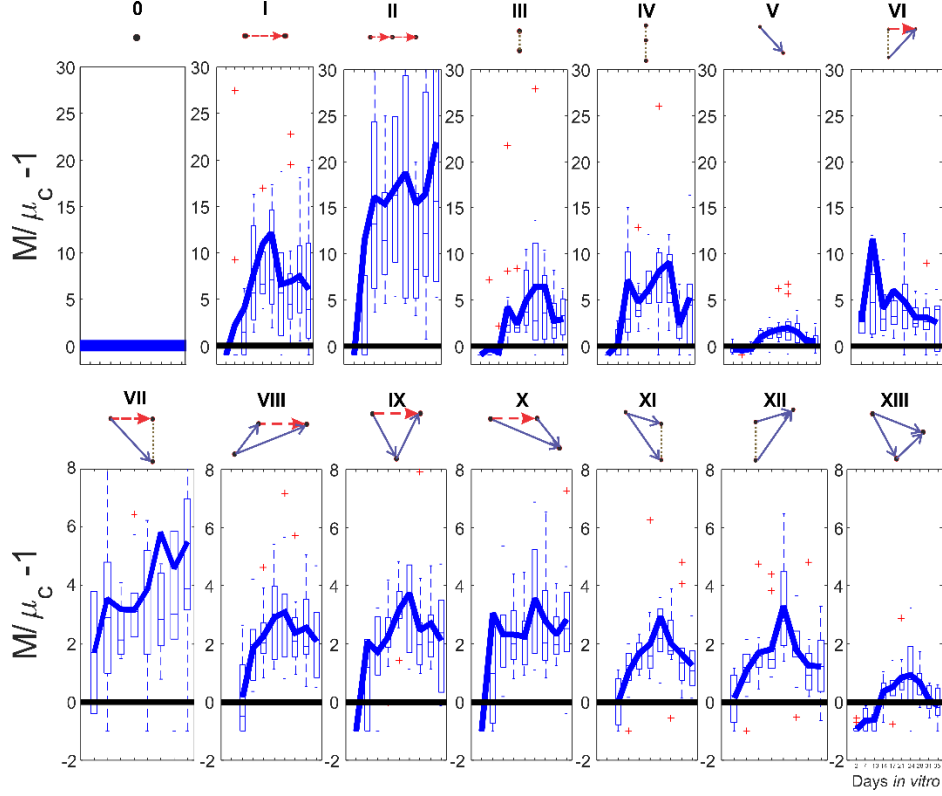


Figure 4.4: The motif-class spectrum for rat cortical neurons over time. The fourteen motif-class profiles from triple correlation provide insight into individual network patterns. Motif classes V (cross-correlation; same as Panel D) and XIII (feedforward spike propagation) show similar trends to that of the published 2D CorSE values in that they gradually increase, peak around 24-28 DIV, and then decrease to network activity comparable to chance. Motif classes XI-XII also peak around 24-28 and decrease from 31-35 DIV, but do not revert to activity comparable to chance from 31-35. In addition, motif classes II and VII (both third-order metrics) show that over time, these network patterns increase.

4.5 Discussion

4.5.1 Overview

Here, we present a novel method to compute the entropy of a neural network based on the 4D spatiotemporal probability distribution function (PDF) generated from triple correlation. This 4D entropy metric is based on the triple correlation spatiotemporal lag PDF, which captures network activity full and uniquely as leveraged by the Triple Correlation Uniqueness theorem (Deshpande *et al.*, 2023). We first validate our approach on a spike raster with isolated

feedforward motif-class patterns. We then apply this approach to an open-source dataset of spiking activity recorded from rat cortical cultures and demonstrate that the 4D entropy value captures underlying network activity from 31-35 DIV, whereas the published 2D entropy shows a decrease. In addition, the trends for motif classes 0 (spike rate), V (cross-correlation), and XIII (feedforward) align with that of the pairwise 2D correlated spectral entropy values. These trends also align with excitatory networks in hippocampal cell cultures, in which maximum excitatory network activity peaks between 14-20 DIV in sparse cultures and between 8-14 DIV for dense cultures (Suresh *et al.*, 2023). Overall, we propose a dual presentation for neural network characterization: 1) 4D entropy as a metric of overall network activity and 2) the fourteen motif-class profiles as metrics of individual network patterns underlying structure.

4.5.2 Limitations and future directions

Like most signal processing tools, there are certain limitations to the application and interpretation of the 4D entropy metric presented in this chapter. The sampling rate as well as and noise embedded within the data are two important criteria to consider prior to analysis: are the data sufficiently sampled to represent the network, and is the signal obscured by noise? These questions, however, are not unique to computing triple correlation or 4D entropy – they should be accounted for with any signal processing and analysis pipeline. Furthermore, while we have developed our metric based on Shannon’s entropy and triple correlation, the researcher should choose the entropy metric based on the question being asked, the type of data, and subsequent analysis. Other entropy metrics include permutation entropy, transfer entropy, and spectral entropy. Permutation entropy is a metric of the predictability of the order of values within the time domain and is particularly useful for analyzing nonlinear signals (Bandt & Pompe, 2000; Paluš & Vejmelka, 2007). Transfer entropy quantifies the flow of information between two

signals by measuring the information from one system to the future behavior of another; thus, this value can help identify causal relationships (Schreiber, 2000). Spectral entropy works in the frequency domain by quantifying the distribution of power across different frequency components (Pincus, 1991). Thus, the choice of entropy, the data type, and the parameters for subsequent processing should be carefully considered before embarking on neural network analysis.

Moreover, interpretation of the entropy metric can be challenging. For example, there have been several studies that interpret higher entropy values as a measure of increased complexity or a measure of functional connectivity within the network (Friston *et al.*, 1994; Achard *et al.*, 2006; Honey *et al.*, 2007; Deco *et al.*, 2008; Pineda-Pardo *et al.*, 2014). Other studies interpret higher entropy values as metrics of randomness and uncertainty (Shannon, 1948; Harris, 2005; Stam *et al.*, 2007; Wu *et al.*, 2008; Tagliazucchi *et al.*, 2012; Betzel *et al.*, 2016). While this is an ongoing question in the literature (how the complexity of a system relates to its entropy), it is important to consider the research question and the context of interpreting entropy values. The work presented in this chapter presents multiple normalization metrics to interpret entropy: entropy of the network relative to that of the product of the marginal distributions, entropy of the network relative to that of the uniform distribution, and entropy of the network relative to that of a surrogate distribution. If the entropy of the network equals the entropy of the product of the marginal distributions, then the discrete variables are statistically independent. Furthermore, we show that entropy of a surrogate distribution, one in which the events of the raster are shuffled across time and space, does not entirely decorrelate all events as the entropy is not maximized from this distribution (Fig. 4.2, Panel G).

Entropy values are typically also intrinsically reductionist – as reducing the complex neural activity to a single scalar value may overlook the intricate dynamics occurring within neural networks. For these reasons, we posit that complementing the 4D entropy value (a measure of the overall network activity) with the individual network-based metrics (the fourteen individual motif-class profiles) provides a more holistic view of network dynamics.

Lastly, future applications of this work abound. The 4D entropy metric can be used to identify distinct dynamical states as well as to map neural networks at multiple scales (from small local circuits with small world properties (Watts & Strogatz, 1998) to large-scale whole brain networks), which could facilitate identification of hubs of brain activity (e.g. rich club organization (van den Heuvel & Sporns, 2011)). In addition, identifying the spatiotemporal lag combination that best captures neural activity from the 4D PDF can guide researchers in evaluating the spatial and temporal scales of activity (e.g. precision of spike timing, synchronization, individual channel activity, and cross-scale activity). In sum, the work presented in this chapter provides an extension of the triple correlation methodology presented in Chapter 3 to ultimately gain insight into overall network structure.

CHAPTER 5

MODELING AND CHARACTERIZING EXCITATORY-INHIBITORY NETWORK ACTIVITY DURING HUMAN FOCAL SEIZURES

5.1 Summary

Computational modeling can serve as a powerful tool to evaluate epileptic mechanisms and can offer valuable insights into the complex and multifaceted phenomena underlying seizures. The goal of the work presented in this chapter is to implement and characterize a Hodgkin-Huxley model of the first three stages of the ictal period: 1) at seizure onset, excitatory and inhibitory populations begin firing in-phase; 2) the inhibitory population then begins to transiently enter and exit neuronal saturation, leading to out-of-phase firing and eventually failure of inhibition; and 3) after excitation dominates, the excitatory populations begins to enter and exit neuronal saturation, generating a characteristic triphasic waveform as observed in multiunit activity recordings. Here, we model the inhibitory population as fast-spiking¹ resonator type neurons and the excitatory population as regular-spiking integrator type neurons. We show that a single-unit Hodgkin-Huxley (HH) model of the first two modeling stages during the ictal pre-recruitment period corroborates the observed transition into out-of-phase firing. Furthermore, we then sought to quantify the network characteristics of the model and of the patient data, and we show agreement between the quantitative network characteristics of the model and patient data. Next, we aimed to replicate the triphasic waveform in multi-unit spike recordings of patients of the third modeling phase during ictal recruitment period. We developed and implemented a multi-unit HH model of the microelectrode, which shows a similar triphasic

¹Note: For the entirety of this dissertation chapter (unless explicitly noted otherwise), the terms “spike” or “ictal spike” refer to action potentials.

waveform. These results suggest that neuronal saturation plays an important role during the three modeling stages: the inhibitory population first undergoes neuronal saturation during the ictal pre-recruitment period, leading to the eventual out-of-phase bursting and uncontrolled excitation. Then, the excitatory population undergoes neuronal saturation during the recruitment period, leading to the characteristic triphasic waveform.

5.2 Introduction

5.2.1 *Regular-spiking and fast-spiking cell types*

Cortical networks consist of 80% excitatory (E) neurons and 20% inhibitory (I) neurons (Meinecke & Peters, 1987; Wonders & Anderson, 2006). Neuronal subtypes within these E-I populations can be diverse in structure, function, electrical & chemical signatures, and firing patterns. Two of these subtypes are termed “regular” spiking (RS) excitatory neurons and “fast” spiking (FS) inhibitory neurons, which are characterized by differences in firing properties and the shape of the action potential waveform (e.g., Izhikevich, 2005). FS inhibitory neurons fire action potentials at higher frequencies and typically have shorter interspike intervals (Izhikevich, 2005). These differences are ultimately determined by the expression of certain ion channels in the cell membranes. Inward currents such as the Kv3.1/Kv3.2 potassium channels expressed in FS inhibitory neurons allow for this sustained high frequency of firing via rapid repolarization of the membrane potential (Erisir *et al.*, 1999; Boddum *et al.*, 2017). The shape of the action potential waveform and firing patterns reflect overall local neuronal activity, and thus, analyses of these neuronal firing patterns can inform us about brain function and structure (Merricks *et al.*, 2015).

5.2.2 Overview of spike sorting

The shape of the action potential waveform is critical for spike sorting. Spike sorting is the process of separating individual action potential spikes in extracellular recordings from multi-unit activity and sorting these individual action potential spikes into groups of putative classes or types of spikes. There is a plethora of methods that have been developed for spike sorting, such as template matching, clustering, and supervised learning methods. Template matching involves matching the shape of an individual action potential spike to a pre-defined reference (template) waveform (Zhang *et al.*, 2004). Clustering methods involve grouping action potential spikes based on waveform characteristics, such as amplitude or spike width (Takahashi *et al.*, 2003; Quiroga *et al.*, 2004). One of the most utilized clustering-based methods is principal component analysis (PCA). PCA is a method of dimensional reduction and works by transforming the dataset to determine the direction of maximum variance in the data distribution (Pearson, 1901). In addition to PCA, additional clustering methods such as k-means clustering and Gaussian mixture models have been utilized to separate groups of action potential spike waveforms (Caro-Martín *et al.*, 2018; Souza *et al.*, 2019). Supervised learning methods involve training a machine learning program to group spikes based on pre-labeled examples (Lewicki, 1998; Chung *et al.*, 2017). Even in measurements with high signal-to-noise levels, these spike sorting methods, however, do not result in accurate sorting of ictal spikes. This failure can be attributed to 1) interference between spike waveforms due to synchrony; and 2) intrinsic changes in waveform morphology features, such as amplitude and spike duration, at the start of the ictal period due to neuronal saturation (Merricks *et al.*, 2015; Merricks *et al.*, 2021). Traditional spike sorting methods depend on reliable, stable spike waveforms, and thus, these methods would not be suitable for ictal spike sorting.

In order to overcome these limitations, a recent study published a novel method to sort spikes from the ictal period (Merricks *et al.*, 2021). Briefly, spike sorting was first performed on the peri-ictal periods (defined as 10 minutes of pre-ictal and 10 minutes of post-ictal periods), as the action potential spikes during these periods are stable. To sort ictal spikes, ictal waveforms were then template matched to their corresponding putative peri-ictal neuron using template matching (Merricks *et al.*, 2021). A 3D convex hull was fit around each single peri-ictal unit in principal component space. The ictal spikes corresponding to the channel of the peri-ictal unit that fit within the convex hull was then template matched to their corresponding peri-ictal unit. A probability density function (PDF) was generated for each sample time point for the peri-ictal waveforms. The ictal waveforms were template-matched to the peri-ictal PDF. Thus, each ictal spike waveform was assigned a match confidence from 0 to 1 (e.g. a higher probability indicates a stronger template match, and a lower probability indicates a weaker template match) (Merricks *et al.*, 2021).

5.2.3 Defining the phases of the ictal period

For human focal seizures, previous studies have proposed the terms pre-recruitment, recruitment, post-recruitment, and pre-termination to describe phases of the ictal period (Schevon *et al.*, 2012; Smith *et al.*, 2016). The ictal wavefront invading the local cortical tissue is known as recruitment, and this phase is characterized by increased neuronal firing and hypersynchronous activity (Fig. 5.1 A-B) (Schevon *et al.*, 2012; Weiss *et al.*, 2013; Smith *et al.*, 2016). The period that precedes recruitment is known as pre-recruitment, and the period that proceeds recruitment is known as post-recruitment (Fig. 5.1A-B). Fig. 5.1A shows a schematic of the first three phases with the expanding ictal wavefront highlighted in red (indicative of recruitment). The surrounding unrecruited territory is indicative of pre-recruitment (highlighted

in the blue color), and the green highlighted color is the brain region that has already been recruited, indicative of post-recruitment (Fig. 5.1A). Multiunit spiking activity recorded from patients implanted with microelectrode arrays showed that during the ictal recruitment period, there is a characteristic triphasic waveform characteristic by a (1) shorter burst of increased firing activity, followed by a (2) period of quiescence, and eventually (3) re-emergence of prolonged lower firing activity (Schevon *et al.*, 2012) (Fig. 5.1B). Analyses of spike sorted results showed that during the ictal pre-recruitment period (the time from seizure onset to recruitment), the excitatory-inhibitory populations begin by bursting in-phase, and eventually, the inhibitory population transitions into an out-of-phase firing (credit: Dr. Edward Merricks at Columbia University, unpublished results) (Fig. 5.1C).

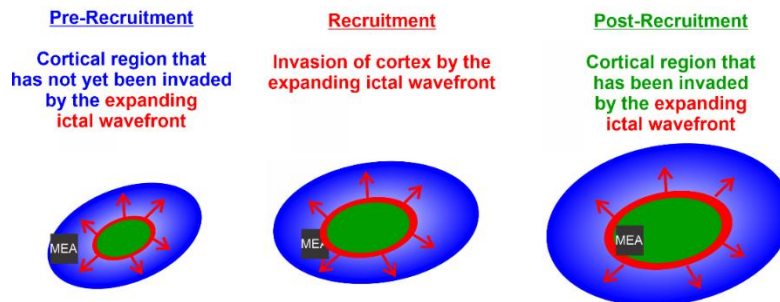
In summary, the overall goal of the work presented in this dissertation chapter is to model the first three stages of cortical seizure activity (Fig. 5.1B-C):

- Stage A: The seizure begins; E-I populations are activated and begin firing in-phase.
- Stage B: As ictal activity progresses, inhibition starts to fail because the inhibitory neurons saturate due to the high levels of activity. This leads the inhibitory neurons to begin firing out-of-phase.
- Stage C: Failure of inhibition is established, and hyperexcitation dominates. The activity patterns are now mainly determined by the excitatory population, which is also subject to neuronal saturation, generating a characteristic triphasic waveform.

Stages A-B (the ictal pre-recruitment period) was modeled with a small population of excitatory and inhibitory neurons (in a ratio of 4:1), and Stage C (the ictal recruitment period) was modeled with an excitatory neuron population captured by a single microelectrode in the MEA.

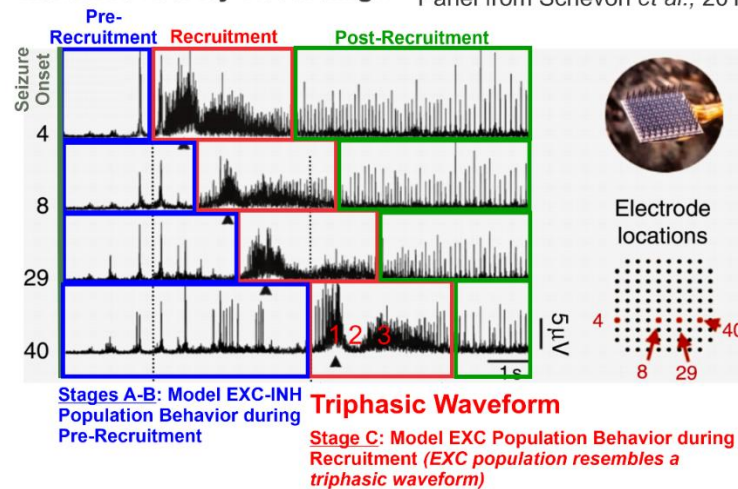
A Defining the Phases of the Ictal Period

Panel adapted from Smith *et al.*, 2016



B Triphasic Waveform of the Recruitment Period from Multiunit Activity Recordings

Panel from Schevon *et al.*, 2012



C Excitatory-Inhibitory Population Activity during the Pre-Recruitment Period

Panel generated by Dr. Ed Merricks

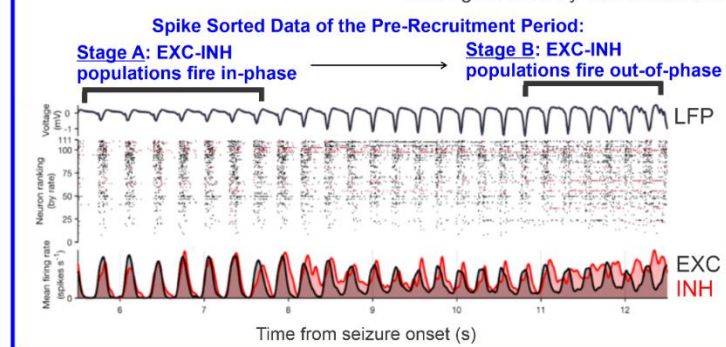


Figure 5.1: Defining the phases of the ictal period. **A)** (Panel adapted from Smith *et al.*, 2016) The recruitment period involves the expanding ictal wavefront (red) invading cortical territory. The region that has not yet been invaded by the seizure wavefront is unrecruited (blue) and is called pre-recruitment. The region that has already been recruited (green) is called post-recruitment. These phases can also be identified on multiunit activity recordings from the microelectrode array (**B** – Panel from Schevon *et al.*, 2012). The recruitment period (highlighted in the red box) shows a characteristic triphasic waveform. The pre-recruitment period (highlighted in the blue box) shows that (**C** – Panel generated by Dr. Ed Merricks) the inhibitory population begins transitioning to out-of-phase firing as the seizure progresses.

5.2.4 Overview of triple correlation²

One aspect of the work presented in this chapter is modeling: specifically, modeling of the first three stages of focal seizure activity. The other aspect of the work presented in this chapter is network characterization. We do so by implementing triple correlation, a signal processing tool that relates three nodes: one reference node and up to two other nodes separated by up to two lags in both space (n_1 & n_2) and time (t_1 & t_2). This generates 169 possible three-node (motif) configurations (Deshpande *et al.*, 2023). These 169 motif configurations can be collapsed into fourteen qualitatively distinct motif classes based on symmetries that occur in time and space (Fig. 5.1, from Deshpande *et al.*, 2023). These motif classes can embody well-studied neuronal processing properties, such as synchrony (motif classes III-IV), feedback (motif class IX), divergence (motif class XI), and convergence (motif class XII). These fourteen motif classes are the motif-class spectrum.

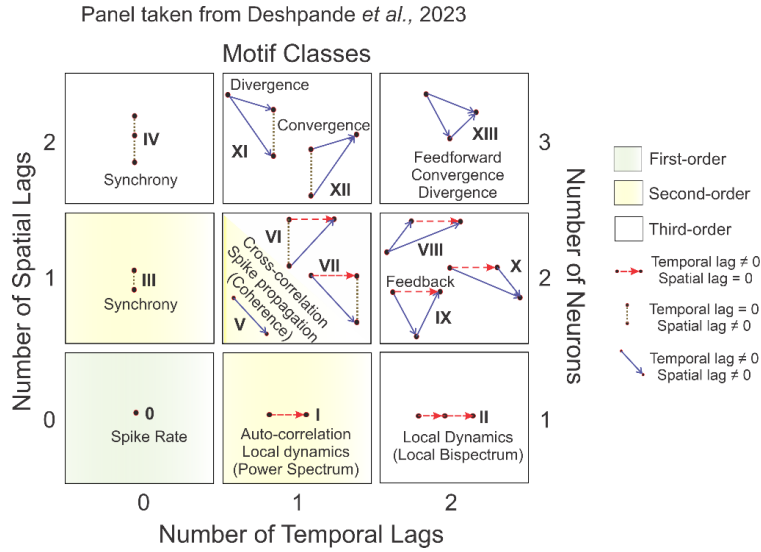


Figure 5.2: The fourteen motif classes generated from triple correlation. Figure from Deshpande *et al.*, 2023 and Chapter 3 of this dissertation.

²This overview of the triple correlation is summarized from Deshpande *et al.*, 2023 and Chapter 3 of this dissertation. A similar summary is provided in Chapter 4 as well.

5.3 Methods

5.3.1 Hodgkin-Huxley formalism

The Hodgkin-Huxley formalism describes the action potential generated by the squid's giant axon. The equation³ is as follows:

$$I = C_m \frac{dV_m}{dt} + \bar{g}_K n^4 (V_m - V_K) + \bar{g}_{Na} m^3 h (V_m - V_{Na}) + \bar{g}_L (V_m - V_L) + g_{syn} (V_m - V_{syn})$$

(Equation 5.1)

in which I is current, C_m is the membrane capacitance, \bar{g} is the maximal conductance, and V_m is the reversal potential, and n , m , and h are dimensionless values associated with potassium channel activation, sodium channel activation, and sodium channel inactivation, respectively.

Hodgkin classified neuronal excitability by the following classes: Type I, Type II, and Type III neural excitability (Hodgkin, 1948; Izhikevich, 2005). Type I neurons can generate action potential spikes that continuously increases from zero injected current, and Type II neurons can generate action potential spikes within a certain frequency band and is discontinuous from zero (Hodgkin, 1948; Izhikevich, 2005). Type III neurons generate a single action potential in response to a current pulse (Hodgkin, 1948; Izhikevich, 2005). Type I neurons (integrators) include excitatory pyramidal neurons, and Type II neurons (resonators) include fast-spiking inhibitory neurons (Hodgkin, 1948; Izhikevich, 2005). Tables 5.1 and 5.2 list the parameters and equations we used to model resonator and integrator type behavior.

³We note that this model is of a single compartment, in which the electrical properties and ion channel densities are uniform throughout the neuron. This differs from a multicompartmental model (De Schutter and Bower, 1994), in which various compartments represent a different part of the neuron (e.g. dendritic structure, soma, axon, etc) (Section 29.3 of van Drongelen, 2018).

Table 5.1: Cellular parameters used in Hodgkin-Huxley model. Values reproduced/scaled from Bukoski *et al.*, 2015.

Cellular Parameters			
	Resonator	Integrator	Units
Capacitance	1	3	$\mu\text{F}/\text{cm}^2$
E_{Na}	55	50	mV
E_{K}	-72	-95	mV
E_{L}	-49.4	-63.7	mV
g_{Na}	120	25	mS/cm^2
g_{K}	36	5	mS/cm^2
g_{L}	0.3	0.1	mS/cm^2

Table 5.2: Gating equations for resonator and integrator classes. This table is reproduced/scaled from Bukoski *et al.*, 2015.

Symbol	Resonator	Integrator
$\alpha_n(V)$	$0.01(V + 50)/\{1 - \exp[-(V + 50)/10]\}$	$-0.032(V + 50)/\{\exp[-(V + 50)/5] - 1\}$
$\alpha_m(V)$	$0.1(V + 35)/\{1 - \exp[-(V + 35)/10]\}$	$-0.0053(V + 52)/\{\exp[-(V + 52)/4] - 1\}$
$\alpha_h(V)$	$0.07 \exp[-(V + 60)/20]$	$0.128 \exp[-(V + 48)/18]$
$\beta_n(V)$	$0.125 \exp[-(V + 60)/80]$	$0.084 \exp[-(V + 55)/40]$
$\beta_m(V)$	$4 \exp[-(V + 60)/18]$	$0.28(V + 25)/\{\exp[(V + 25)/5] - 1\}$
$\beta_h(V)$	$1/\{\exp[-(V + 30)/10] + 1\}$	$4/\{\exp[-(V + 25)/5] + 1\}$

The model neurons were placed in a 10-neuron network (Fig. 5.3). The synaptic currents in the network were determined by the following equation:

$$I_{\text{syn}} = g_{\text{syn}}(V_m - V_{\text{syn}}) \quad (\text{Equation 5.2})$$

in which I_{syn} is the synaptic current, g_{syn} is the synaptic conductance, and V_{syn} is the synaptic reversal potential.

5.3.2 Modeling synaptic conductance

Synaptic conductance (g_{syn}) can be modeled as the sum of functions that depend on the timing of a presynaptic spike. This can be modeled by the following equation:

$$g_{\text{syn}}(t) = \bar{g}_{\text{syn}} \sum_n \delta(t - t_n) \quad (\text{Equation 5.3})$$

where $\sum_n \delta$ is the Dirac delta function modeling the arrival of the n^{th} spike at time t_n .

The alpha function can be used to model g_{syn} and can be determined by the following general form of the equation (Lopes da Silva *et al.*, 1980; Shefchyk & Jordan, 1985; van Drongelen, 2018; Tryba *et al.*, 2019):

$$g_{syn} = \alpha\beta te^{-\alpha\beta t} \quad (\text{Equation 5.4})$$

in which α and β are synapse-specific constants. This can be expressed as the following second-order ODE (Lopes da Silva *et al.*, 1980; van Drongelen, 2018; Tryba *et al.*, 2019):

$$\ddot{y}(t) = \alpha\beta x(t) - 2\beta\dot{y}(t) - \beta^2 y(t) \quad (\text{Equation 5.5})$$

in which $x(t)$ is the presynaptic spike train modeled by the Dirac delta function. Equation 5.5 can be expressed as the following coupled first-order ODEs:

$$\dot{y}(t) = z(t) \quad (\text{Equation 5.6})$$

$$\dot{z}(t) = \alpha\beta x(t) - 2\beta z(t) - \beta^2 y(t) \quad (\text{Equation 5.7})$$

For an excitatory synapse, $\alpha = 25$ and $\beta=0.3 \text{ ms}^{-1}$. For an inhibitory synapse, $\alpha = 3$ and $\beta=0.1 \text{ ms}^{-1}$ (Tryba *et al.*, 2019).

5.4 Results

5.4.1 Stages A-B: Modeling E-I network activity during ictal pre-recruitment

Using previously established parameter sets (Bukoski, 2015), we implemented fast-spiking/resonator behavior for the inhibitory cell type and regular-spiking/integrator activity for the excitatory cell type (Tables 5.1, 5.2; Fig. 5.3A). These cell types were configured in a 4:1 ratio for excitatory and inhibitory neurons respectively (Fig. 5.3B). The cortical model was placed in a passing ictal wave and rhythm, modeled as an exponential growth function and a sinusoidal waveform respectively, and the resulting activity was determined. Assuming an extracellular electrode equidistant from the model neurons, the extracellular network activity (the

population firing rates) was determined as the signal proportional to the sum of the second derivatives of all membrane potentials, representing the transmembrane currents (Clark and Plonsey, 1968). Fig. 5.3C (top row) shows that the extracellular response of the model mimics the observed behavior depicted in Fig. 5.1C: at seizure onset, the inhibitory and excitatory cells burst synchronously in-phase, followed by a phase shift in inhibitory bursting activity, and ultimately leading to out-of-phase inhibitory bursting that begins at 12.0 seconds. Afterwards, the excitatory population begins to enter tonic firing at 14.4 seconds. Intracellularly, we see that the inhibitory population is characterized by decreasing spike amplitudes within bursts starting at 10 seconds as well as decreasing spike amplitudes overall starting at 12 seconds (Fig. 5.3D), indicative of the inhibitory population transiently entering and exiting neuronal saturation.

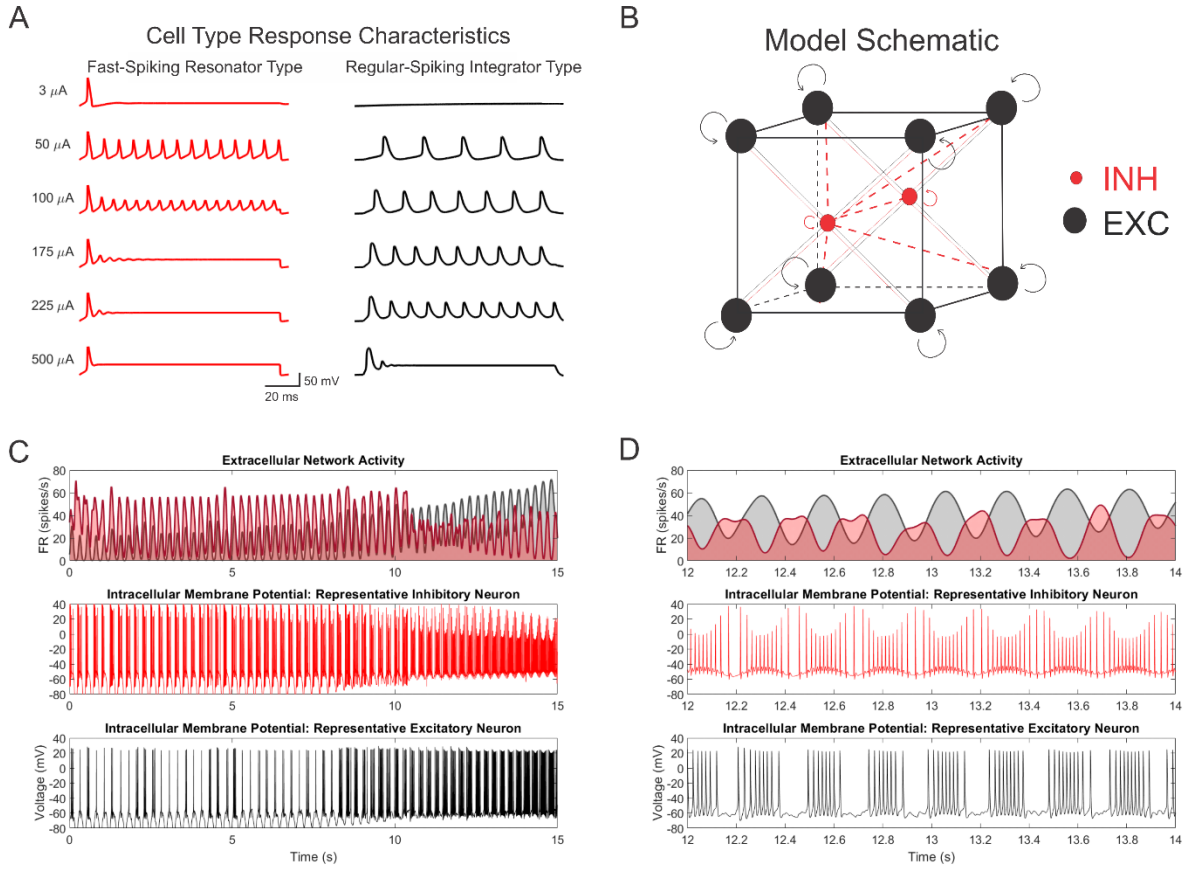


Figure 5.3: Model of the ictal pre-recruitment period corroborates clinical patterns. **A)** Cell type response characteristics for fast-spiking resonator (inhibitory) type neurons (red) and regular-spiking integrator (excitatory) type neurons (black). Fast-spiking resonator type neurons will saturate prior to regular-spiking integrator type neurons at lower input currents. **B)** Model schematic of the 10-neuron model, with excitatory and inhibitory cells in a 4:1 ratio. **C)** The extracellular network activity of the model corroborates the extracellular network activity of the patient data. At seizure onset, the inhibitory and excitatory populations burst in-phase. As the seizure progresses towards ictal recruitment, the inhibitory population begins to burst out-of-phase. This can be attributed to neuronal saturation of the inhibitory population, which can be observed by the decreasing spike amplitudes within bursts and overall in the intracellular membrane potential. **D)** These phenomena can be observed in the zoomed-in view from 12 to 14 seconds.

The results presented in Fig. 5.3 offer a mechanistic basis to qualitatively explain the transition of inhibitory in-phase to out-of-phase firing. Given these results, the next natural extension would be to make a quantitative comparison between the model and patient networks. In order to do so, triple correlation was computed across one second epochs of the spike raster throughout the 15 seconds of the pre-recruitment period (sampled at 500 Hz), with a spatial

window that covered the entirety of the dataset and a temporal window of 100 ms (lags from -50 ms:50 ms). The ratio of late phase (from 9-15 seconds of the pre-recruitment period) motif-class contributions to the early phase (from 1-6 seconds of the pre-recruitment period) motif-class contributions was determined for both the model (blue) and patient (red) networks (Fig. 5.4). Comparison of these networks across the motif-class spectra shows that there is no significant difference between the model and the patient networks (Fig. 5.4A; Mann Whitney U test, $p>0.05^4$ for all 14 motif classes). In addition, these ratios were then collapsed across the motif-class spectra for both the model and patient networks, and there was no significant difference between these distributions (Fig. 5.4B; Kolmogorov-Smirnov test, $p>0.05^4$). This quantitative analysis using triple correlation shows agreement between the model and patient networks within individual motif classes as well as overall network profiles.

We then aimed to show that the phase ratios between the excitatory (EXC) and inhibitory (INH) population firing rates are comparable between the model and patient recordings. To do so, the population firing rates were demeaned to remove the DC component and then filtered using a narrow finite impulse response (FIR) bandpass filter (frequency band: 3-5.5 Hz; 500th order FIR1 filter in Matlab). The Hilbert transform was then applied to the filtered population firing rates, from which the phase angles were computed. The ratio of the phase angles (EXC/INH phase) was determined for both the patient recordings and model over time. The cross-correlation of the phase ratios showed a significant correlation between the patient recording and the model (Fig. 5.5; correlation coefficient (r) = 0.63; $p<0.001$), albeit with a small temporal shift of 39 ms.

⁴The p-values are greater than 0.05 for the Mann-Whitney U test and the Kolmogorov-Smirnov test; hence, we accept the null hypothesis that there is not enough evidence to show that the difference between the two distributions (model and patient recordings) is statistically significant.

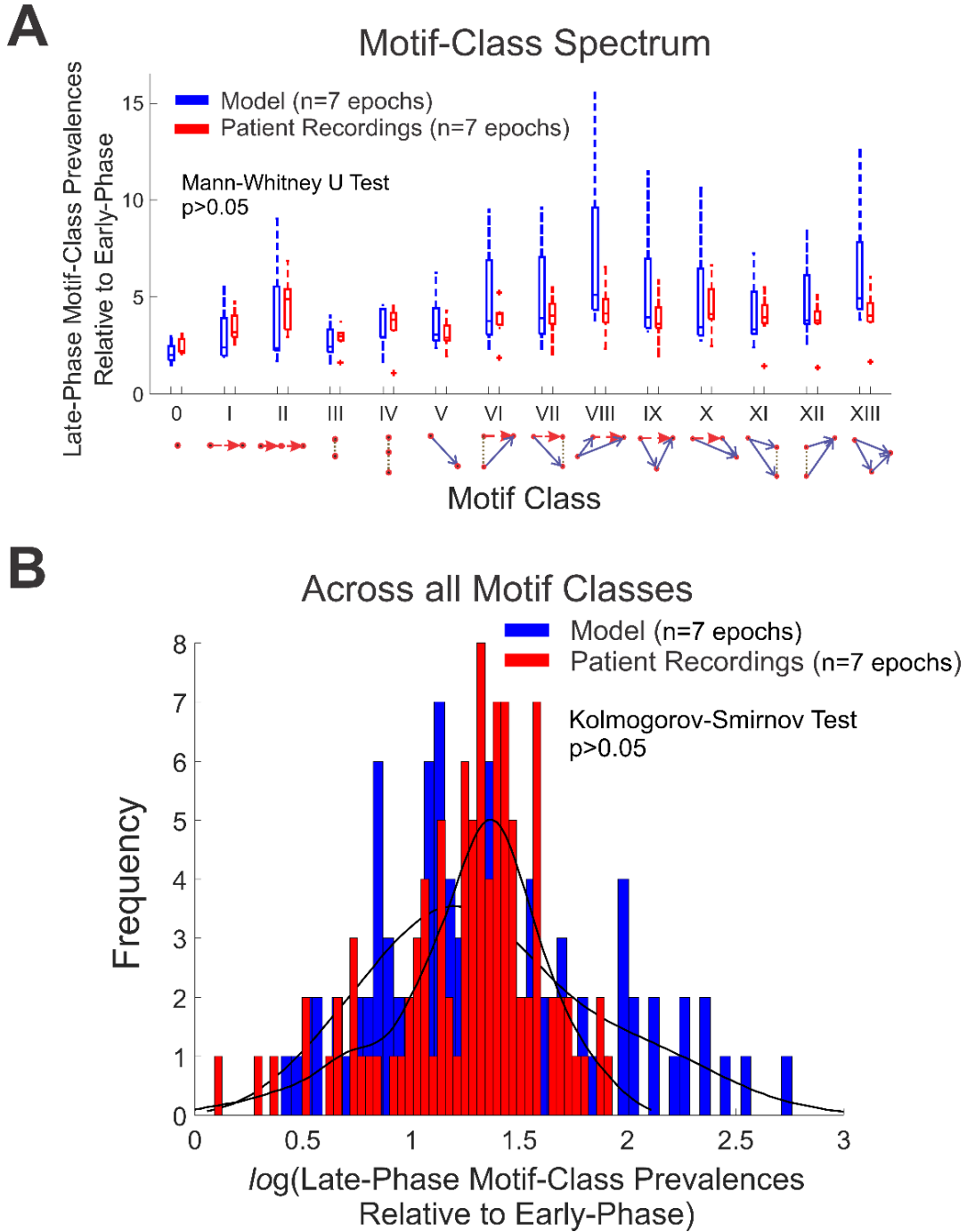


Figure 5.4: Quantitative network comparison using triple correlation. A) There was no significant difference between the ratio of the late-phase (from 9-15 seconds of the ictal pre-recruitment period) motif-class prevalences to the early-phase (from 1-6 seconds of the ictal pre-recruitment period) motif-class prevalences between the model (blue) and patient networks (red) (Mann Whitney U test, $p > 0.05$ for all 14 motif classes). **B)** Collapsing the ratios across all motif classes generates a distribution for the model network and a distribution for the patient network. There is no significant difference between these two distributions (Kolmogorov-Smirnov test, $p > 0.05$).

Cross-correlation of Phase Ratios (EXC/INH for Patient Data & EXC/INH for Model)

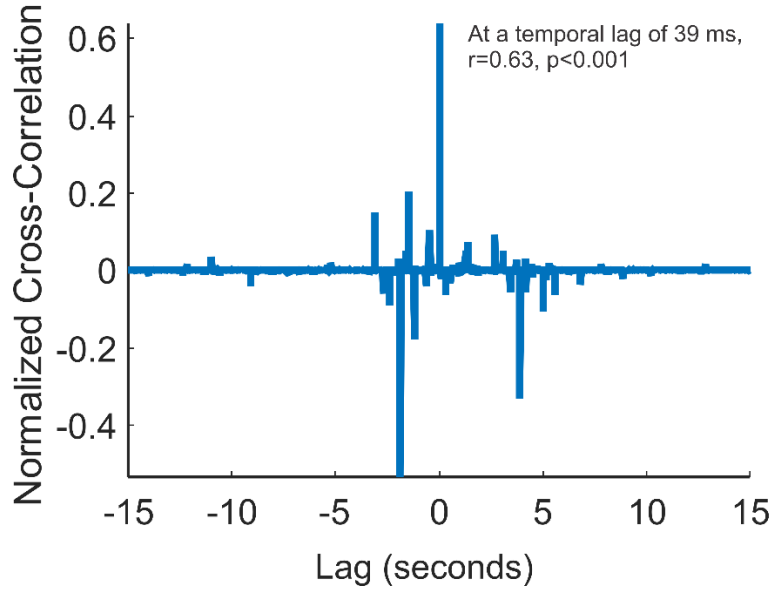


Figure 5.5: Cross-correlation of the phase angle ratios using Hilbert transform. The phase ratios (determined from the excitatory/inhibitory population firing rates) between the model and patient recordings shows a significant correlation ($r=0.63$; $p<0.001$), albeit with a small temporal shift of 39 ms.

We then sought to investigate the effects of adjusting the strength of the connections in the model (as governed by the synaptic weights). There are four synaptic connections in the model: $E \rightarrow E$, $E \rightarrow I$, $I \rightarrow E$, and $I \rightarrow I$. These are represented by the synaptic weight variables w_{EE} , w_{EI} , w_{IE} , and w_{II} , respectively. We evaluated the mean firing rate in response to changes in the cross-synaptic weights (w_{EI} & w_{IE}) (Fig. 5.6). By strengthening w_{EI} , the inhibitory population shows a sharp decrease in firing rate from 10-15 seconds (Fig. 5.6A). This can be attributed to the inhibitory population entering and exiting neuronal saturation quicker, and hence, decreasing the inhibitory firing rate overall. By increasing w_{IE} , the excitatory population decreases in firing rate, as expected (Fig. 5.6B). These phenomena can be further appreciated by the snapshots of the population firing rates with specific combinations of the cross-synaptic weights, which are shown in Fig. 5.6C-E.

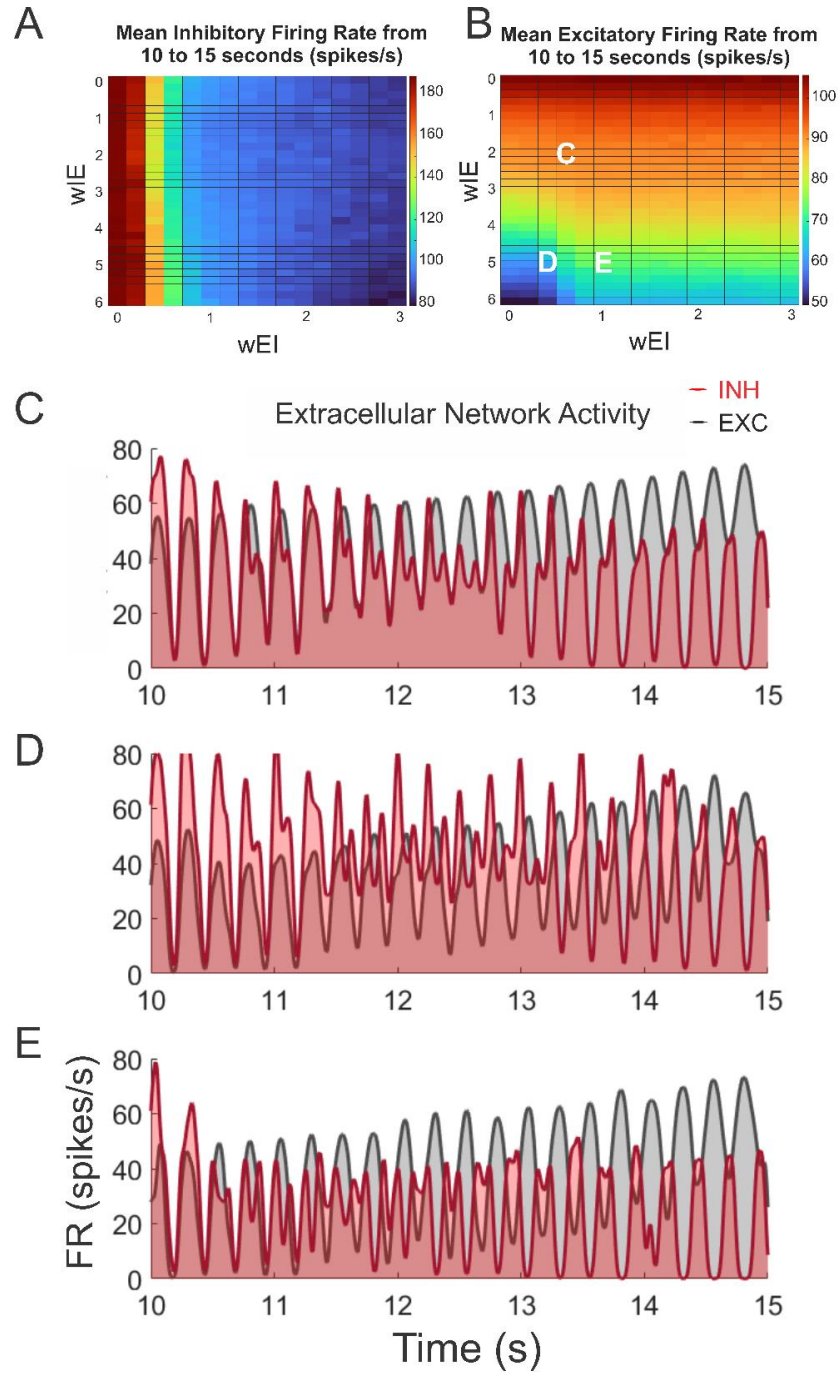


Figure 5.6: Effects of adjusting the cross-synaptic weights. (A) The mean firing rate for the inhibitory (B) and excitatory populations were measured after adjusting the cross-synaptic weights, w_{EI} & w_{IE} , from 0 to 3 and 0 to 6, respectively. The inhibitory population firing rate is strongly affected by the strength of $E \rightarrow I$ synapses as it rapidly decreases when w_{EI} ranges from 0 to 2. The excitatory population firing rate is mainly dependent on the strength of $I \rightarrow E$ synapses. Representative snapshots of various combinations of synaptic weights are shown in Panels C-E. Panel E is the combination of synaptic weights that is shown in Figure 5.3.

5.4.2 Stage C: Simulating excitatory network activity during ictal recruitment

The ictal recruitment period follows the pre-recruitment period and is characterized by invasion of the local tissue by the ictal wavefront, which brings strong excitatory drive to the region (Schevon *et al.*, 2012; Smith *et al.*, 2016). At this stage, inhibition has failed and hyperexcitation dominates (Schevon *et al.*, 2012). In patient recordings, this period is characterized by a triphasic waveform as observed by the multi-unit spiking activity. The three phases of this waveform can be described as follows: 1) a shorter period of higher firing activity, followed by a 2) period of quiescence, and then eventually 3) emergence of a longer but lower firing activity (Schevon *et al.*, 2012). The goal of the following work is to use modeling efforts to explain this pattern.

A Hodgkin-Huxley model representative of a single microelectrode of excitatory neurons (model parameters from Chapter 29 of van Drongelen, 2018) placed in a passing ictal wave (modeled by increasing excitatory drive to the microelectrode) showed that the extracellular network activity of the model resembles the triphasic waveform as seen in clinical recordings (Fig. 5.7). The scope of neural activity captured by the microelectrode is modeled as a sphere with a radius of 200 μm (Fig. 5.7A-B), and the signal captured by the microelectrode attenuates exponentially with distance (e.g., the signals from excitatory neurons farther away from the microelectrode contribute less to the overall signal) (Fig. 5.7C). The extracellular multi-unit activity voltage trace from the model was determined from the first derivative of the sum of the attenuated intracellular membrane potentials across the microelectrode array (as the weighted contributions are proportional to $C \frac{dV}{dt}$) (Anastassiou *et al.*, 2015; López-Jury *et al.*, 2018). The signal trace from the patient recordings (Fig. 5.7D – Panel from Schevon *et al.*, 2012) resembles the extracellular signal from the model during the recruitment period. Specifically, the model

trace captures each component of the triphasic waveform as seen in the patient recordings (Fig. 5.7C-D).

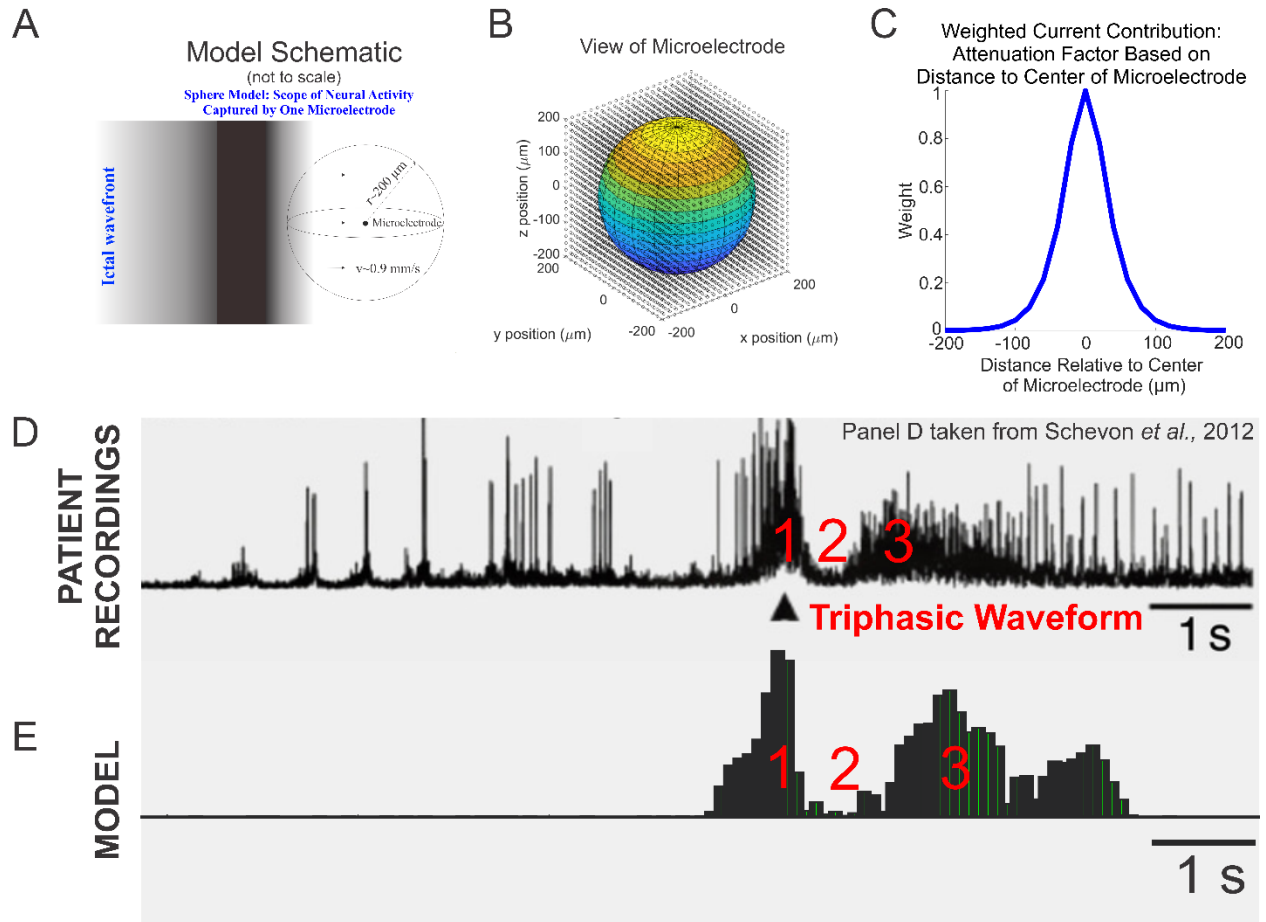


Figure 5.7: Model of the ictal recruitment period. **A)** Schematic of the microelectrode sphere model: the scope of neural activity is captured with the radius of the sphere, which is placed in a passing ictal wavefront (velocity $\sim 0.9 \text{ mm/s}$). **B)** View of one microelectrode (cube) with a sphere radius of $200 \mu\text{m}$ in three dimensions. **C)** The current contributions from each neuron are weighted according to an exponentially modeled attenuation factor based on the distance from the center of the microelectrode (the farther the neuron from the center of the microelectrode, the lower the contribution and vice versa). The ictal recruitment pattern of a triphasic waveform as exhibited by patient recordings (**D**) is corroborated by the extracellular signal of the model (**E**).

5.5 Discussion

5.5.1 Overview

Overall, the modeling work presented in this chapter reflects the first three stages of ictal activity during human focal seizures: Stages A-B capture the transition from in-phase firing of the excitatory-inhibitory populations to out-of-phase firing of the inhibitory population as the seizure progresses during the ictal pre-recruitment period and inhibitory function begins to fail. In addition, Stage C captures the triphasic waveform, characteristic of the ictal recruitment period. In summary, the inhibitory neurons saturate first prior to ictal recruitment, leading to out-of-phase firing characterized by decreasing spike amplitudes within bursts and overall, which eventually results in failure of inhibition during recruitment. Then, the uncontrolled activity of the excitatory neurons enters and exits saturation during recruitment. Stages A-B were modeled by a small population of excitatory and inhibitory neurons in a 4:1 ratio (consistent with the 80:20 putative ratio of E-I populations in the brain), and Stage C, resulting from failed inhibition, was modeled by a larger population of excitatory neurons as captured by one model microelectrode. Both models (of ictal pre-recruitment and ictal recruitment) reflect activity within the ictal core as the ictal wavefront is invading the neuronal populations.

5.5.2 Limitations and future directions

While the work presented in this chapter offers valuable insights into the mechanisms underlying excitatory-inhibitory population activity, there are several limitations. First, we note that parvalbumin-positive interneurons are known as the “fast-spiking” inhibitory cells and consist of ~40% of the inhibitory neurons present in the brain (Rudy *et al.*, 2011). The remaining 60% of inhibitory neurons include somatostatin-positive (SST+) and ionotropic serotonin 5-HT3a-positive interneurons (Rudy *et al.*, 2011). These neurons have different firing

characteristics (Izhikevich, 2005), and thus, a resonator type neuron would not be suitable to model these other inhibitory neurons. As such, the model of the ictal pre-recruitment period, which incorporates Hodgkin's Type I (integrator) and Type II (resonator) classes of neural spiking, does not account for other inhibitory neuron behaviors. One approach to address this limitation would be to incorporate an Izhikevich-type model, which consists of six fundamental classes of firing patterns (Izhikevich, 2005). For the excitatory population, these classes include regular spiking, chattering, and intrinsically bursting (Izhikevich, 2005). For the inhibitory population, these classes include fast spiking, low-threshold spiking (which can be used to model SST+ interneurons), and late spiking (Izhikevich, 2005).

The shape of the characteristic triphasic waveform during ictal recruitment is also indicative of underlying neuronal activity. The model triphasic waveform in Fig. 5.6E appears to have a “bump” towards the tail end of the signal, which could be indicative of activity consistent with post-recruitment discharges (as are visible in the signal trace in Fig. 5.6D). We can appreciate from Fig. 5.1B that various microelectrodes exhibit different qualitative ictal recruitment patterns (as the shapes of the triphasic waveforms in these four microelectrodes are all slightly different), which would explain the slight qualitative differences between the model and patient triphasic waveforms (Fig. 5.7D-E). As such, one limitation of this model of the ictal recruitment period is that it only consists of neuronal activity generated from one single microelectrode placed in recruited territory. Future work may involve modeling the ictal recruitment period across the entire Utah array (10x10, 96-microelectrodes, 4 mm x 4 mm grid) to simulate signals during neuronal recruitment across multiple microelectrodes and for the entirety of the seizure.

Furthermore, we have previously shown in Chapter 2 that human focal seizures may activate mid-range excitatory connections (on the millimeter scale) in the gray matter if the spatiotemporal dynamics resemble sinc-like functions (Lee *et al.*, 2023). This was also corroborated by the multiunit spiking activity across the microelectrode array, in which the propagating ictal wavefront will activate neuronal activity several millimeters away (Schevon *et al.*, 2012; Lee *et al.*, 2023). The modeling work presented in this chapter of the three stages incorporate only short-range synaptic connections (on the microscale). While the models show similar qualitative and quantitative network behavior to that of the patient data (Fig. 5.3, 5.4, 5.5, 5.7), future work may involve adding more parameters to model the effects of connections on the mesoscale (mm-range) and macroscale (cm-range).

CHAPTER 6

CONCLUSIONS

While the contents of the chapters in this dissertation span a range of research topics, there is a common theme among all of them: how can I *characterize* and *model* brain networks in time and space? Overall, the work presented in this dissertation was motivated by the overarching goals of 1) furthering our understanding of epileptiform mechanisms to improve treatment options for drug-resistant epilepsy patients, and 2) unraveling pertinent information from data recording modalities which may have previously been elusive. I tackle these goals from multiple angles by ultimately asking the following questions: what are the spatiotemporal characteristics and mechanisms underlying human focal seizures:

- within the ictal period vs. outside the ictal period (time)?
- within the seizure onset zone and outside the seizure onset zone (space)?
- within excitatory and inhibitory populations (type)?

As such, the main takeaways from this dissertation are: 1) There exists a mathematical symmetry between time and space if the spatiotemporal spike-centered averages (a novel second-order metric of the spike-LFP relationship that considers both spike *timing* and *location* across the microelectrode array) resemble sinc functions. This is also explained by a mathematical model of the underlying network unit impulse response of a macroelectrode of cortex. 2) The novel classification of third-order motifs and the subsequent quantitative network metrics that arise from *triple correlation* (as presented in Chapter 3) offer a complete and unique characterization of network activity, indicating that there is a one-to-one relationship between the network itself and its transformed triple correlation. 3) Measuring functional connectivity of rat

cortical cultures using 4D entropy, which is a novel quantitative metric derived from the spatiotemporal lag PDF from triple correlation, shows that there is added value in the 4D entropy metric compared to published 2D (pairwise) entropy. Since the 4D spatiotemporal PDF and the 4D entropy are derived from triple correlation (which is a complete and unique representation of network activity per the Triple Correlation Uniqueness theorem), these two metrics can capture more comprehensive information regarding network behavior. 4) Lastly, I culminate the work in this thesis by addressing the overarching goals together in Chapter 5, where I implement a Hodgkin-Huxley model to gain mechanistic insight into underlying cell-type network behavior during human focal seizures. The results from the modeling efforts point to neuronal saturation as the underlying mechanism for E-I population activity during the first three stages of the ictal period.

While the primary motivation for the development of the novel signal processing tools in this dissertation was to investigate seizure mechanisms, these methods can be applied to a multitude of datasets to broadly investigate neural activity. Chapter 2 presents a second-order metric for focal epilepsy patients implanted with microelectrode arrays (MEA) for epileptic monitoring and identification of the seizure onset zone. This method can also be applied to MEAs implanted in monkeys to investigate the spike-LFP relationship in response to reach-to-grasp motor tasks (Brochier *et al.*, 2018) or MEAs implanted in humans for intracortical brain-computer interfaces (Homer *et al.*, 2014). Chapter 3 presents a third-order metric that can be applied to much broader recording modalities as triple correlation can be applied to any finite, bounded dataset that can be interpreted as an image, including but not limited to: MEA, EEG, ECoG, and LFP recordings in neuroscience, image analyses, spread of infectious disease, and social networks. Lastly, Chapter 4 presents two metrics of quantitative network activity (4D

spatiotemporal PDF and its associated entropy) based on the triple correlation spatiotemporal lag distribution and can be utilized to analyze spike rasters in terms of underlying behavior, such as functional connectivity, network topology, and information processing. These novel signal processing tools address the gap between current methods of recording signals (especially in the case of seizures) and our ability to interpret and differentiate physiological and pathological states. Furthermore, the proposed methods can be used to study the functional interactions between mesoscale and macroscale networks. The significance of these innovations is that while the tools to acquire data remain the same (EEG, ECoG, and MEA), the results and information achieved from the proposed methods are novel and valuable. Lastly, because the proposed methods work within the scope of already utilized and approved data acquisition tools (EEG, ECoG, and MEA), these methods can be translated to clinical care for a more individualized treatment plan for patients, which is especially relevant for drug-resistant focal epilepsy patients.

6.1 Translational Implications and Future Directions

The work presented in this dissertation offers valuable insights into neural network analyses. Chapters 2 and 5 involve modeling and characterization of brain networks in pathological seizure states, specifically human focal seizures. These data were acquired by implanting microelectrode arrays and electrocorticography electrodes onto the putative seizure onset zone of cortex. We found that there exists a mathematical symmetry between the temporal and spatial domains of the spatiotemporal spike-centered average (st-SCA) if they resemble sinc functions. From this, focal seizures that are spatiotemporally characterized by sinc functions could involve the engagement of mid-range excitatory connections. We found that the st-SCAs of focal seizures with secondary generalization do not resemble sinc functions, but rather a strong excitatory signal centered around the action potential spike. We also show that applying

the st-SCA method to a random subset of 8 microelectrode arrays results in a signal resembling a sinc function in the temporal domain. A natural follow-up question from these findings is: how can we use the information obtained from this tool to guide treatment for pharmacoresistant focal epilepsy? Our results point to the potential of utilizing subpial transections that target mid-range excitatory connections in the gray matter without disrupting the white matter (long-range, cm-scale) tracts (Morrell *et al.*, 1989; Hufnagel *et al.*, 1997) for patients who have st-SCAs resembling sinc functions.

The triple correlation approach presented in Chapter 3 offers a complete and unique characterization of neural networks. For this reason, scientific and translational applications abound. Triple correlation has been used to detect neonatal seizures from EEG recordings (Smith *et al.*, 2023), to characterize electrocorticography (ECoG) signals in epilepsy patients in response to stimulation (unpublished results, collaboration with Dr. Schevon at Columbia University, New York, NY), and to characterize differential network responses between male and female cortical cultures in response to hypoxia (unpublished results, collaboration with Dr. van Putten at the University of Twente, The Netherlands). Indeed, because this approach offers quantitative metrics of underlying network structure that is conditioned to the lower-order constituent motifs, we can gain insight into actual network structure, and not just network activity that can be explained by chance. In addition, the 4D entropy value presented in Chapter 4 can be utilized to gain insight into the complexity and underlying network structure as entropy is considered a fundamental concept in information theory. This 4D entropy value can be used to differentiate physiological states from pathological states (such as seizures), track network activity over time, and facilitate identification of markers of disease states (such as changes in the spike-LFP relationship during seizures).

As a physician-scientist in-training, I hope that the contributions presented in this dissertation not only advance our understanding of neural network science, but also lay the foundation for the development of novel therapies, detection tools, and predictive biomarkers for pathological brain states. In conclusion, I am enthusiastic to present these contributions in the context of the broader framework of current neuroscientific knowledge and medical practices as well as the potential they hold for future applications.

REFERENCES

- Abeles, M. (1982). *Local Cortical Circuits, Studies of Brain Function* (Vol. 6, 1st ed.). Springer. doi: 10.1007/978-3-642-81708-3
- Abeles, M. (1991). *Corticonics: Neural Circuits of the Cerebral Cortex* (1st ed.). Cambridge University Press. doi: 10.1017/CBO9780511574566
- Abeles, M., & Gerstein, G. L. (1988). Detecting spatiotemporal firing patterns among simultaneously recorded single neurons. *Journal of Neurophysiology*, 60(3), 909–924. doi: 10.1152/jn.1988.60.3.909
- Achard, S., Salvador, R., Whitcher, B., Suckling, J., & Bullmore, E. (2006). A resilient, low-frequency, small-world human brain functional network with highly connected association cortical hubs. *Journal of Neuroscience*, 26(1), 63-72. doi: 10.1523/JNEUROSCI.3874-05.2006.
- Amin, U., & Benbadis, S. R. (2019). The Role of EEG in the Erroneous Diagnosis of Epilepsy. *Journal of Clinical Neurophysiology*, 36(4), 294-297. doi: 10.1097/WNP.0000000000000572.
- Anastassiou, C. A., Perin, R., Buzsáki, G., Markram, H., & Koch, C. (2015). Cell type- and activity-dependent extracellular correlates of intracellular spiking. *Journal of neurophysiology*, 114(1), 608–623. doi.org/10.1152/jn.00628.2014
- Baker, S. N., & Lemon, R. N. (2000). Precise spatiotemporal repeating patterns in monkey primary and supplementary motor areas occur at chance levels. *Journal of Neurophysiology*, 84, 1770–1780. doi: 10.1152/jn.2000.84.4.1770.
- Bandt, C., & Pompe, B. (2002). Permutation entropy: A natural complexity measure for time series. *Physical Review Letters*, 88(17), 174102. doi: 10.1103/PhysRevLett.88.174102.
- Bartelt, H., Lohmann, A. W., & Wirtzner, B. (1984). Phase and amplitude recovery from bispectra. *Applied Optics*, 23, 3121–3129. doi: 10.1364/AO.23.003121.
- Bassett, D. S., & Bullmore, E. (2006). Small-world brain networks. *Neuroscientist*, 12(6), 512-523. doi: 10.1177/1073858406293182.
- Bazelot, M., Dinocourt, C., Cohen, I., & Miles, R. (2010). Unitary inhibitory field potentials in the CA3 region of rat hippocampus. *Journal of Physiology*, 588(Pt 12), 2077-2090. <https://doi.org/10.1113/jphysiol.2009.185918>.
- Berg, A. T., Berkovic, S. F., Brodie, M. J., Buchhalter, J., Cross, J. H., van Emde Boas, W., Engel, J., French, J., Glauser, T. A., Mathern, G. W., Moshé, S. L., Nordli, D., Plouin, P., Scheffer, I. E. (2010). Revised terminology and concepts for organization of seizures and epilepsies: Report of the ILAE Commission on Classification and Terminology, 2005-2009. *Epilepsia*, 51(4), 676-685. doi: 10.1111/j.1528-1167.2010.02522.x.
- Berger, H. (1929). Über das elektroencephalogramm des menschen. *Archiv für Psychiatrie und Nervenkrankheiten*, 87(1), 527–570.

- Berkovic, S. F. (2015). Genetics of epilepsy in humans. *Cold Spring Harbor Perspectives in Medicine*. Advance online publication. doi: 10.1101/cshperspect.a022400.
- Bernabei, J. M., Arnold, T. C., Shah, P., Revell, A., Ong, I. Z., Kini, L. G., Stein, J. M., Shinohara, R. T., Lucas, T. H., Davis, K. A., Bassett, D. S., & Litt, B. (2021). Electrocorticography and stereo EEG provide distinct measures of brain connectivity: implications for network models. *Brain Communications*, 3(3), fcab156. doi: 10.1093/braincomms/fcab156.
- Biswal, B., Yetkin, F. Z., Haughton, V. M., & Hyde, J. S. (1995). Functional connectivity in the motor cortex of resting human brain using echo-planar MRI. *Magnetic Resonance in Medicine*, 34(4), 537-541. doi: 10.1002/mrm.1910340409.
- Boashash, B. (2016). Chapter I: The Time-Frequency Approach: Essence and Terminology, *Time-Frequency Signal Analysis and Processing* (Second Edition) (pp. 3-29). Academic Press. <https://doi.org/10.1016/B978-0-12-398499-9.09991-X>
- Boddum, K., Hougaard, C., Xiao-Ying Lin, J., von Schoubye, N. L., Jensen, H. S., Grunnet, M., & Jespersen, T. (2017). Kv3.1/Kv3.2 channel positive modulators enable faster activating kinetics and increase firing frequency in fast-spiking GABAergic interneurons. *Neuropharmacology*, 118, 102-112. doi: 10.1016/j.neuropharm.2017.02.024.
- Bojanek, K., Zhu, Y., & MacLean, J. (2020). Cyclic transitions between higher order motifs underlie sustained asynchronous spiking in sparse recurrent networks. *PLoS Computational Biology*, 16, e1007409. doi: 10.1371/journal.pcbi.1007409.
- Borisyyuk, G. N., Borisyyuk, R. M., Khibnik, A. I., & Roose, D. (1995). Dynamics and bifurcations of two coupled neural oscillators with different connection types. *Bulletin of Mathematical Biology*, 57(6), 809-840. doi: 10.1007/BF02458296.
- Bou Assi, E., Gagliano, L., Rihana, S., Nguyen, D. K., & Sawan, M. (2018). Bispectrum features and multilayer perceptron classifier to enhance seizure prediction. *Scientific Reports*, 8, 15491. doi: 10.1038/s41598-018-33969-9.
- Brent, D. A., Crumrine, P. K., Varma, R., et al. (1990). Phenobarbital treatment and major depressive disorder in children with epilepsy: a naturalistic follow-up. *Pediatrics*, 85(6), 1086-1091.
- Briellmann, R. S., Hopwood, M. J., & Jackson, G. D. (2007). Major depression in temporal lobe epilepsy with hippocampal sclerosis: clinical and imaging correlates. *Journal of Neurology, Neurosurgery & Psychiatry*, 78(11), 1226-1230. doi: 10.1136/jnnp.2006.104521. Epub 2007 Jan 26.
- Britton, J. W., Frey, L. C., Hopp, J. L., Korb, P., Koubeissi, M. Z., Lievens, W. E., Pestana-Knight, E. M., & St. Louis, E. K. (2016). *Electroencephalography (EEG): An Introductory Text and Atlas of Normal and Abnormal Findings in Adults, Children, and Infants*. Chicago: American Epilepsy Society.

- Brochier, T., Zehl, L., Hao, Y., Duret, M., Sprenger, J., Denker, M., Grün, S., & Riehle, A. (2018). Massively parallel recordings in macaque motor cortex during an instructed delayed reach-to-grasp task. *Scientific data*, 5, 180055. doi.org/10.1038/sdata.2018.55
- Bromfield, E. B., Cavazos, J. E., & Sirven, J. I. (Eds.). (2006). *An Introduction to Epilepsy*. West Hartford (CT): American Epilepsy Society.
- Brunel, N. (2000). Dynamics of sparsely connected networks of excitatory and inhibitory spiking neurons. *Journal of Computational Neuroscience*, 8(3), 183-208. doi: 10.1023/a:1008925309027.
- Bullmore, E., & Sporns, O. (2009). Complex brain networks: graph theoretical analysis of structural and functional systems. *Nature Reviews Neuroscience*, 10(3), 186-198. doi: 10.1038/nrn2575.
- Buzsáki, G., & Draguhn, A. (2004). Neuronal oscillations in cortical networks. *Science*, 304, 1926–1929. doi: 10.1126/science.1099745.
- Buzsáki, G., Anastassiou, C. A., & Koch, C. (2012). The origin of extracellular fields and currents--EEG, ECoG, LFP and spikes. *Nature Reviews Neuroscience*, 13(6), 407-420. doi: 10.1038/nrn3241
- Campbell, S., & Wang, D. (1996). Synchronization and desynchronization in a network of locally coupled Wilson-Cowan oscillators. *IEEE Transactions on Neural Networks*, 7(3), 541-554. doi: 10.1109/72.501714.
- Caro-Martín, C. R., Delgado-García, J. M., Gruart, A., & Sánchez-Campusano, R. (2018). Spike sorting based on shape, phase, and distribution features, and K-TOPS clustering with validity and error indices. *Scientific Reports*, 8, 17796. doi: 10.1038/s41598-018-35491-4.
- Chung, J. E., Magland, J. F., Barnett, A. H., Tolosa, V. M., Tooker, A. C., Lee, K. Y., Shah, K. G., Felix, S. H., Frank, L. M., & Greengard, L. F. (2017). A Fully Automated Approach to Spike Sorting. *Neuron*, 95(6), 1381-1394.e6. doi: 10.1016/j.neuron.2017.08.030.
- Cole, M. W., Bassett, D. S., Power, J. D., Braver, T. S., & Petersen, S. E. (2014). Intrinsic and task-evoked network architectures of the human brain. *Neuron*, 83(1), 238-251. doi: 10.1016/j.neuron.2014.05.014.
- Cule, J. (1973). *The Falling Sickness: A History of Epilepsy from the Greeks to the Beginnings of Modern Neurology*, Owsei Temkin, 2nd ed. rev., Baltimore and London, Johns Hopkins Press, 1971, pp. xv, 467, illus., £7.15. *Medical History*, 17(2), 214-215. doi: 10.1017/S0025727300018640
- Czapinski, P., Terczynski, A., & Czapinska, E. (1997). Randomised 36-month comparative study of valproic acid (VPA), phenytoin (PHT), phenobarbital (PHB) and carbamazepine (CBZ) efficacy in patients with newly diagnosed epilepsy with partial complex seizures. *Journal of the Neurological Sciences*, 150, 162-163.

Czornyj, L., Auzmendi, J., & Lazarowski, A. (2022). Transporter hypothesis in pharmacoresistant epilepsies. Is it at the central or peripheral level? *Epilepsia Open*, 7(Suppl 1), S34-S46. doi: 10.1002/epi4.12537. Epub 2021 Oct 29.

Davies, J. A. (1995). Mechanisms of action of antiepileptic drugs. *Seizure*, 4(4), 267-271. doi: 10.1016/s1059-1311(95)80003-4.

Dechery, J. B., & MacLean, J. N. (2018). Functional triplet motifs underlie accurate predictions of single-trial responses in populations of tuned and untuned V1 neurons. *PLoS Computational Biology*, 14, e1006153. doi: 10.1371/journal.pcbi.1006153.

Deco, G., Ponce-Alvarez, A., Mantini, D., Romani, G. L., Hagmann, P., & Corbetta, M. (2013). Resting-state functional connectivity emerges from structurally and dynamically shaped slow linear fluctuations. *The Journal of Neuroscience*, 33(27), 11239-11252. doi: 10.1523/JNEUROSCI.1091-13.2013.

Depannemaecker, D., Destexhe, A., Jirsa, V., & Bernard, C. (2021). Modeling seizures: From single neurons to networks. *Seizure*, 90, 4-8. doi: 10.1016/j.seizure.2021.06.015. Epub 2021 Jun 17.

Deshpande, S. S., Smith, G. A., & van Drongelen, W. (2023). Third-order motifs are sufficient to fully and uniquely characterize spatiotemporal neural network activity. *Scientific Reports*, 13(1), 238. doi: 10.1038/s41598-022-27188-6.

De Schutter, E., & Bower, J. M. (1994). An active membrane model of the cerebellar Purkinje cell II. Simulation of synaptic responses. *Journal of neurophysiology*, 71(1), 401-419. <https://doi.org/10.1152/jn.1994.71.1.401>

Destexhe, A., Rudolph, M., Fellous, J. M., & Sejnowski, T. J. (2001). Fluctuating synaptic conductances recreate in vivo-like activity in neocortical neurons. *Neuroscience*, 107(1), 13-24. doi: 10.1016/s0306-4522(01)00344-x.

Destexhe, A., Mainen, Z., & Sejnowski, T. (1998). Kinetic models of synaptic transmission. In C. Koch & I. Segev (Eds.), *Methods in Neuronal Modelling* (pp. 1-25). Cambridge, MA: MIT Press.

Diesmann, M., Gewaltig, M. O., & Aertsen, A. (1999). Stable propagation of synchronous spiking in cortical neural networks. *Nature*, 402, 529-533. doi: 10.1038/990101.

Dimitrov, A. G., Lazar, A. A., & Victor, J. D. (2011). Information theory in neuroscience. *Journal of Computational Neuroscience*, 30(1), 1-5. doi: 10.1007/s10827-011-0314-3.

Eissa, T. L., Schevon, C. A., Emerson, R. G., McKhann, G. M., Jr., Goodman, R. R., & Van Drongelen, W. (2017). Cross-scale effects of neural interactions during human neocortical seizure activity. *Proceedings of the National Academy of Sciences*, 114(40), 10761-10766. doi: 10.1073/pnas.1702490114.

Eissa, T. L., Schevon, C. A., Emerson, R. G., McKhann, G. M., Jr., Goodman, R. R., & Van Drongelen, W. (2018). The Relationship Between Ictal Multi-Unit Activity and the

Electrocorticogram. *International Journal of Neural Systems*, 28(10), 1850027. doi: 10.1142/S0129065718500272.

Eissa, T. L., Tryba, A. K., Marcuccilli, C. J., Ben-Mabrouk, F., Smith, E. H., Lew, S. M., Goodman, R. R., McKhann, G. M., Jr., Frim, D. M., Pesce, L. L., Kohrman, M. H., Emerson, R. G., Schevon, C. A., & van Drongelen, W. (2016). Multiscale Aspects of Generation of High-Gamma Activity during Seizures in Human Neocortex. *eNeuro*, 3(2). doi: 10.1523/ENEURO.0141-15.2016.

Erisir, A., Lau, D., Rudy, B., & Leonard, C. S. (1999). Function of specific K(+) channels in sustained high-frequency firing of fast-spiking neocortical interneurons. *Journal of Neurophysiology*, 82(5), 2476-2489. doi: 10.1152/jn.1999.82.5.2476.

Ermentrout, G. B., Galán, R. F., & Urban, N. N. (2008). Reliability, synchrony and noise. *Trends in Neurosciences*, 31(8), 428-434. doi: 10.1016/j.tins.2008.06.002. Epub 2008 Jul 5.

Extercatte, J., de Haan, G. J., & Gaitatzis, A. (2015). Teaching Video NeuroImages: Frontal opercular seizures with Jacksonian march. *Neurology*, 84(11), e83-e84. doi: 10.1212/wnl.0000000000001363.

Eyo, U. B., Murugan, M., & Wu, L. J. (2016). Microglia-Neuron Communication in Epilepsy. *Glia*, 65(1), 5-18. doi: 10.1002/glia.23006. Epub 2016 May 18.

Fattorusso, A., Matricardi, S., Mencaroni, E., Dell'Isola, G. B., Di Cara, G., Striano, P., & Verrotti, A. (2021). The Pharmacoresistant Epilepsy: An Overview on Existant and New Emerging Therapies. *Frontiers in Neurology*, 12, 674483. doi: 10.3389/fneur.2021.674483.

Ferrie, C. D. (2006). Preventing misdiagnosis of epilepsy. *Archives of Disease in Childhood*, 91(3), 206-209. doi: 10.1136/adc.2005.088906.

Fiest, K. M., Sauro, K. M., Wiebe, S., Patten, S. B., Kwon, C. S., Dykeman, J., Pringsheim, T., Lorenzetti, D. L., & Jetté, N. (2017). Prevalence and incidence of epilepsy: A systematic review and meta-analysis of international studies. *Neurology*, 88(3), 296-303. doi: 10.1212/WNL.0000000000003509.

Fisher, R. S., Acevedo, C., Arzimanoglou, A., Bogacz, A., Cross, J. H., Elger, C. E., Engel, J. Jr, Forsgren, L., French, J. A., Glynn, M., Hesdorffer, D. C., Lee, B. I., Mathern, G. W., Moshé, S. L., Perucca, E., Scheffer, I. E., Tomson, T., Watanabe, M., & Wiebe, S. (2014). ILAE official report: A practical clinical definition of epilepsy. *Epilepsia*, 55(4), 475-482. <https://doi.org/10.1111/epi.12550>.

Fisher, R. S., van Emde Boas, W., Blume, W., Elger, C., Genton, P., Lee, P., Engel, J. Jr. (2005). Epileptic seizures and epilepsy: definitions proposed by the International League Against Epilepsy (ILAE) and the International Bureau for Epilepsy (IBE). *Epilepsia*, 46(4), 470-472. doi: 10.1111/j.0013-9580.2005.66104.x.

FitzHugh, R. (1961). Impulses and physiological states in theoretical models of nerve membrane. *Biophysical Journal*, 1(6), 445-466.

- Friston, K. J., Harrison, L., & Penny, W. (2003). Dynamic causal modelling. *NeuroImage*, 19(4), 1273-1302. doi: 10.1016/S1053-8119(03)00202-7.
- Friston, K. J. (2011). Functional and effective connectivity: a review. *Brain Connectivity*, 1(1), 13-36. doi: 10.1089/brain.2011.0008.
- Gagliano, L., Bou Assi, E., Nguyen, D. K., & Sawan, M. (2019). Bispectrum and recurrent neural networks: Improved classification of interictal and preictal states. *Scientific Reports*, 9, 15649. doi: 10.1038/s41598-019-52152-2.
- Gerster, M., Berner, R., Sawicki, J., Zakharova, A., Škoch, A., Hlinka, J., & Schöll, E. (2020). FitzHugh-Nagumo oscillators on complex networks mimic epileptic-seizure-related synchronization phenomena. *Chaos*, 30(12), 123130. doi: 10.1063/5.0021420.
- Glickfeld, L. L., Roberts, J. D., Somogyi, P., & Scanziani, M. (2009). Interneurons hyperpolarize pyramidal cells along their entire somatodendritic axis. *Nature Neuroscience*, 12(1), 21-23. doi: 10.1038/nn.2230.
- Glykys, J., Dzhalal, V., Egawa, K., Kahle, K. T., Delpire, E., & Staley, K. (2017). Chloride Dysregulation, Seizures, and Cerebral Edema: A Relationship with Therapeutic Potential. *Trends in Neurosciences*, 40(5), 276-294.
- Goodkin, H. P., Sun, C., Yeh, J. L., Mangan, P. S., & Kapur, J. (2007). GABA(A) receptor internalization during seizures. *Epilepsia*, 48(Suppl 5), 109-113. doi: 10.1111/j.1528-1167.2007.01297.x.
- Grenier, F., Timofeev, I., Crochet, S., & Steriade, M. (2003). Spontaneous field potentials influence the activity of neocortical neurons during paroxysmal activities in vivo. *Neuroscience*, 119(1), 277-291.
- Grün, S. (2009). Data-driven significance estimation for precise spike correlation. *Journal of Neurophysiology*, 101, 1126–1140. doi.org/10.1152/jn.00093.2008
- Haider, H. A., Esteller, R., Hahn, C. D., Westover, M. B., Halford, J. J., Lee, J. W., Shafi, M. M., Gaspard, N., Herman, S. T., Gerard, E. E., Hirsch, L. J., Ehrenberg, J. A., & LaRoche, S. M. (2016). Sensitivity of quantitative EEG for seizure identification in the intensive care unit. *Neurology*, 87(9), 935-944. doi.org/10.1212/WNL.0000000000003034
- Han, P., Trinidad, B. J., & Shi, J. (2015). Hypocalcemia-induced seizure: demystifying the calcium paradox. *ASN Neuro*, 7(2), 1759091415578050.
- Harris, S. A., Sands, Z. A., & Laughton, C. A. (2005). Molecular dynamics simulations of duplex stretching reveal the importance of entropy in determining the biomechanical properties of DNA. *Biophysical Journal*, 88(3), 1684-1691. doi.org/10.1529/biophysj.104.046912
- Hebb, D. O. (1949). *The Organization of Behavior: A Neuropsychological Theory* (1st ed.). Wiley.

- Hellwig, S., Mamalis, P., Feige, B., Schulze-Bonhage, A., & van Elst, L. T. (2012). Psychiatric comorbidity in patients with pharmacoresistant focal epilepsy and psychiatric outcome after epilepsy surgery. *Epilepsy Behavior*, 23(3), 272-279. doi.org/10.1016/j.yebeh.2011.12.001.
- Hermann, B., Seidenberg, M., Lee, E. J., Chan, F., & Rutecki, P. (2007). Cognitive phenotypes in temporal lobe epilepsy. *Journal of the International Neuropsychological Society*, 13(1), 12-20. doi.org/10.1017/S135561770707004X
- Herreras, O. (2016). Local Field Potentials: Myths and Misunderstandings. *Frontiers in Neural Circuits*, 10, 101. doi.org/10.3389/fncir.2016.00101
- Hertz, J., & Prügel-Bennett, A. (1996). Learning synfire chains: Turning noise into signal. *International Journal of Neural Systems*, 7, 445-450. <https://doi.org/10.1142/s0129065796000427>
- Hodgkin, A. L. (1948). The local electric changes associated with repetitive action in a non-medullated axon. *Journal of Physiology*, 107(2), 165-181. doi.org/10.1113/jphysiol.1948.sp004260
- Homer, M. L., Nurmikko, A. V., Donoghue, J. P., & Hochberg, L. R. (2013). Sensors and decoding for intracortical brain computer interfaces. *Annual review of biomedical engineering*, 15, 383–405. doi.org/10.1146/annurev-bioeng-071910-124640
- Honey, C. J., Kötter, R., Breakspear, M., & Sporns, O. (2007). Network structure of cerebral cortex shapes functional connectivity on multiple time scales. *Proceedings of the National Academy of Sciences of the United States of America*, 104(24), 10240-10245. doi.org/10.1073/pnas.0701519104
- Hong, S. J., Bernhardt, B. C., Gill, R. S., Bernasconi, N., & Bernasconi, A. (2017). The spectrum of structural and functional network alterations in malformations of cortical development. *Brain*, 140(8), 2133-2143. doi.org/10.1093/brain/awx145
- Hotka, M., & Kubista, H. (2019). The paroxysmal depolarization shift in epilepsy research. *International Journal of Biochemistry & Cell Biology*, 107, 77-81.
- Huff, J. S., & Murr, N. (2022). Psychogenic Nonepileptic Seizures. In *StatPearls*. Retrieved from StatPearls Publishing.
- Hufnagel, A., Zentner, J., Fernandez, G., Wolf, H. K., Schramm, J., & Elger, C. E. (1997). Multiple subpial transection for control of epileptic seizures: effectiveness and safety. *Epilepsia*, 38(6), 678–688. doi.org/10.1111/j.1528-1157.1997.tb01237.x
- Hyvärinen, T., Hlushchuk, Y., Ristola, M., et al. (2019). Functional characterization of human pluripotent stem cell-derived cortical networks differentiated on laminin-521 substrate: Comparison to rat cortical cultures. *Scientific Reports*, 9, 17125. doi.org/10.1038/s41598-019-53647-8
- Hyvärinen, A., Karhunen, J., & Oja, E. (2001). *Independent Component Analysis*. Wiley.

- Ibrahim, M. M., Kamran, M. A., Mannan, M. M. N., Jung, I. H., & Kim, S. (2021, February 16). Lag synchronization of coupled time-delayed FitzHugh-Nagumo neural networks via feedback control. *Scientific Reports*, 11(1), 3884. doi.org/10.1038/s41598-021-82886-x.
- Ikegaya, Y., Tamura, H., Ogawa, M., & Yamaguchi, Y. (2004). Synfire chains and cortical songs: Temporal modules of cortical activity. *Science*, 304, 559-564. doi.org/10.1126/science.1093173
- Iorio, F., Saez-Rodriguez, J., & Bernardo, D. (2013). Network based elucidation of drug response: From modulators to targets. *BMC Systems Biology*, 7, 139. doi.org/10.1186/1752-0509-7-139
- Iqbal, M., Rehan, M., Khaliq, A., Saeed-ur-Rehman, & Hong, K. S. (2014). Synchronization of coupled different chaotic FitzHugh-Nagumo neurons with unknown parameters under communication-direction-dependent coupling. *Computational and Mathematical Methods in Medicine*, 2014, 367173. doi.org/10.1155/2014/367173
- Isnard, J., Guénot, M., Sindou, M., & Mauguière, F. (2004). Clinical manifestations of insular lobe seizures: A stereo-electroencephalographic study. *Epilepsia*, 45(9), 1079-1090. doi.org/10.1111/j.0013-9580.2004.68903.x
- Ito, J. (2015). Spike Triggered Average. In D. Jaeger & R. Jung (Eds.), *Encyclopedia of Computational Neuroscience* (pp. 2832-2835). Springer New York. doi.org/10.1007/978-1-4614-6675-8_407
- Izhikevich, E. M. (2003). Simple model of spiking neurons. *IEEE Transactions on Neural Networks*, 14(6), 1569-1572. doi.org/10.1109/TNN.2003.820440
- Jansen, N. A., Perez, C., Schenke, M., van Beurden, A. W., Dehghani, A., Voskuyl, R. A., Thijs, R. D., Ullah, G., van den Maagdenberg, A. M. J. M., & Tolner, E. A. (2021). Impaired θ - γ Coupling Indicates Inhibitory Dysfunction and Seizure Risk in a Dravet Syndrome Mouse Model. *The Journal of Neuroscience*, 41(3), 524-537. doi.org/10.1523/JNEUROSCI.2132-20.2020
- Jayakar, P., Gaillard, W. D., Tripathi, M., Libenson, M. H., Mathern, G. W., & Cross, J. H. (2014). Diagnostic test utilization in evaluation for resective epilepsy surgery in children. *Epilepsia*, 55(4), 507-518. doi.org/10.1111/epi.12544
- Jehi, L. (2018). The Epileptogenic Zone: Concept and Definition. *Epilepsy Currents*, 18(1), 12-16. doi.org/10.5698/1535-7597.18.1.12
- Jensen, F. E. (2011). Epilepsy as a spectrum disorder: Implications from novel clinical and basic neuroscience. *Epilepsia*, 52(Suppl 1), 1-6. doi.org/10.1111/j.1528-1167.2010.02904.x
- Jeong, W., Jin, S. H., Kim, M., Kim, J. S., & Chung, C. K. (2014). Abnormal functional brain network in epilepsy patients with focal cortical dysplasia. *Epilepsy Research*, 108(9), 1618-1626. doi.org/10.1016/j.eplepsyres.2014.09.006

- Jiang, M., Gao, X., An, H., Li, H., & Sun, B. (2017). Reconstructing complex network for characterizing the time-varying causality evolution behavior of multivariate time series. *Scientific Reports*, 7, 10486. doi.org/10.1038/s41598-017-10759-3
- Jirsa, V. K., Stacey, W. C., Quilichini, P. P., Ivanov, A. I., & Bernard, C. (2014). On the nature of seizure dynamics. *Brain*, 137, 2210-2230. https://doi.org/10.1093/brain/awu133
- Jovanović, S., & Rotter, S. (2016). Interplay between graph topology and correlations of third order in spiking neuronal networks. *PLoS Computational Biology*, 12, e1004963. doi.org/10.1371/journal.pcbi.1004963
- Julesz, B., Gilbert, E. N., Shepp, L. A., & Frisch, H. L. (1973). Inability of humans to discriminate between visual textures that agree in second-order statistics-revisited. *Perception*, 2, 391-405. doi.org/10.1068/p020391
- Julesz, B. (1962). Visual pattern discrimination. *IRE Transactions on Information Theory*, 8, 84-92. doi.org/10.1109/TIT.1962.1057698
- Kahn, E., Lane, M., & Sagher, O. (2017). Eloquent: history of a word's adoption into the neurosurgical lexicon. *Journal of neurosurgery*, 127(6), 1461–1466. doi.org/10.3171/2017.3.JNS17659
- Kamiński, M. J., & Blinowska, K. J. (1991). A new method of the description of the information flow in the brain structures. *Biological Cybernetics*, 65(3), 203-210. doi.org/10.1007/BF00198091
- Kanner, A. M. (2004). Recognition of the various expressions of anxiety, psychosis, and aggression in epilepsy. *Epilepsia*, 45(Suppl 2), 22-27. doi.org/10.1111/j.0013-9580.2004.452004.x
- Kapucu, F. E., Vinogradov, A., Hyvärinen, T., Ylä-Outinen, L., & Narkilahti, S. (2022). Comparative microelectrode array data of the functional development of hPSC-derived and rat neuronal networks. *Scientific Data*, 9, 1-10. doi.org/10.1038/s41597-022-01242-4
- Keeley, S., Byrne, Á., Fenton, A., & Rinzel, J. (2019). Firing rate models for gamma oscillations. *Journal of Neurophysiology*, 121(6), 2181-2190. doi.org/10.1152/jn.00741.2018
- Kreuz, T., Chicharro, D., Greschner, M., & Andrzejak, R. G. (2011). Time-resolved and time-scale adaptive measures of spike train synchrony. *Journal of Neuroscience Methods*, 195, 92-106. doi.org/10.1016/j.jneumeth.2010.11.020
- Kreuz, T., Chicharro, D., Houghton, C., Andrzejak, R. G., & Mormann, F. (2013). Monitoring spike train synchrony. *Journal of Neurophysiology*, 109, 1457-1472. doi.org/10.1152/jn.00873.2012
- LaFrance, W. C. Jr., Kanner, A. M., & Hermann, B. (2008). Psychiatric comorbidities in epilepsy. *International Review of Neurobiology*, 83, 347-383. doi.org/10.1016/S0074-7742(07)83018-3

- Lee, S., Deshpande, S. S., Merricks, E. M., Schlafly, E., Goodman, R., McKhann, G. M., Eskandar, E. N., Madsen, J. R., Cash, S. S., van Putten, M. J. A. M., Schevon, C. A., & van Drongelen, W. (2023). Spatiotemporal spike-centered averaging reveals symmetry of temporal and spatial components of the spike-LFP relationship during human focal seizures. *Communications Biology*, 6, 317. doi.org/10.1038/s42003-023-04696-3
- Lewicki, M. S. (1998). A review of methods for spike sorting: the detection and classification of neural action potentials. *Network: Computation in Neural Systems*, 9(4), R53-R78. doi.org/10.1088/0954-898X_9_4_001
- López-Jury, L., Meza, R. C., Brown, M. T. C., Henny, P., & Canavier, C. C. (2018). Morphological and Biophysical Determinants of the Intracellular and Extracellular Waveforms in Nigral Dopaminergic Neurons: A Computational Study. *The Journal of neuroscience*, 38(38), 8295–8310. doi.org/10.1523/JNEUROSCI.0651-18.2018
- Li, X., Li, Z., Yang, W., Wu, Z., & Wang, J. (2022). Bidirectionally Regulating Gamma Oscillations in Wilson-Cowan Model by Self-Feedback Loops: A Computational Study. *Frontiers in Systems Neuroscience*, 16, 723237. doi.org/10.3389/fnsys.2022.723237
- Lopes da Silva, F. H., Vos, J. E., Mooibroek, J., & Van Rotterdam, A. (1980). Relative contributions of intracortical and thalamo-cortical processes in the generation of alpha rhythms, revealed by partial coherence analysis. *Electroencephalography and Clinical Neurophysiology*, 50(5-6), 449-456. doi.org/10.1016/0013-4694(80)90011-5
- Luders, H. O., Engel, J., & Munari, C. (1993). General principles. In J. J. Engel (Ed.), *Surgical Treatment of the Epilepsies* (2nd ed., pp. 137-153). Raven Press.
- Lytton, W. W. (1998). Adapting a feedforward heteroassociative network to Hodgkin-Huxley dynamics. *Journal of Computational Neuroscience*, 5(4), 353-364. doi.org/10.1023/A:1026456411040
- Masquelier, T. (2018). STDP Allows Close-to-Optimal Spatiotemporal Spike Pattern Detection by Single Coincidence Detector Neurons. *Neuroscience*, 389, 133-140. doi.org/10.1016/j.neuroscience.2017.06.032
- Matsumoto, H., & Ajmone Marsan, C. (1964). Cortical cellular phenomena in experimental epilepsy: Interictal manifestations. *Experimental Neurology*, 9, 286-304. doi.org/10.1016/0014-4886(64)90025-1
- McCulloch, W. S., & Pitts, W. (1943). A logical calculus of the ideas immanent in nervous activity. *Bulletin of Mathematical Biophysics*, 5, 115–133. doi: 10.1007/BF02478259.
- Meijer, H. G., Eissa, T. L., Kiewiet, B., Neuman, J. F., Schevon, C. A., Emerson, R. G., Goodman, R. R., McKhann, G. M. Jr., Marcuccilli, C. J., Tryba, A. K., Cowan, J. D., van Gils, S. A., & van Drongelen, W. (2015). Modeling focal epileptic activity in the Wilson-cowan model with depolarization block. *Journal of Mathematical Neuroscience*, 5, 7. doi: 10.1186/s13408-015-0019-4.

- Merricks, E. M., Smith, E. H., McKhann, G. M., Goodman, R. R., Bateman, L. M., Emerson, R. G., Schevon, C. A., & Trevelyan, A. J. (2015). Single unit action potentials in humans and the effect of seizure activity. *Brain*, 138(Pt 10), 2891-2906. doi: 10.1093/brain/awv208.
- Merricks, E. M., Smith, E. H., Emerson, R. G., Bateman, L. M., McKhann, G. M., Goodman, R. R., Sheth, S. A., Greger, B., House, P. A., Trevelyan, A. J., & Schevon, C. A. (2021). Neuronal Firing and Waveform Alterations through Ictal Recruitment in Humans. *Journal of Neuroscience*, 41(4), 766-779. doi: 10.1523/JNEUROSCI.0417-20.2020.
- Milo, R., et al. (2002). Network motifs: Simple building blocks of complex networks. *Science*, 298, 824–827. doi: 10.1126/science.298.5594.824.
- Mišić, B., Goñi, J., Betzel, R. F., Sporns, O., & McIntosh, A. R. (2014). A network convergence zone in the hippocampus. *PLoS Computational Biology*, 10(12), e1003982. doi: 10.1371/journal.pcbi.1003982.
- Misra, A., Burke, J. F., Ramayya, A. G., Jacobs, J., Sperling, M. R., Moxon, K. A., Kahana, M. J., Evans, J. J., & Sharan, A. D. (2014). Methods for implantation of micro-wire bundles and optimization of single/multi-unit recordings from human mesial temporal lobe. *Journal of Neural Engineering*, 11(2), 026013. doi: 10.1088/1741-2560/11/2/026013.
- Morrell, F., Whisler, W. W., & Bleck, T. P. (1989). Multiple subpial transection: A new approach to the surgical treatment of focal epilepsy. *Journal of Neurosurgery*, 70(2), 231-239. doi: 10.3171/jns.1989.70.2.0231.
- Morris, C., & Lecar, H. (1981). Voltage oscillations in the barnacle giant muscle fiber. *Biophysical Journal*, 35(1), 193-213. doi: 10.1016/S0006-3495(81)84782-0.
- Nagumo, J., Arimoto, S., & Yoshizawa, S. (1962). An active pulse transmission line simulating nerve axon. *Proceedings of the IRE*, 50(10), 2061-2070.
- Naze, S., Bernard, C., & Jirsa, V. (2015). Computational modeling of seizure dynamics using coupled neuronal networks: Factors shaping epileptiform activity. *PLoS Computational Biology*, 11(5), e1004209. doi: 10.1371/journal.pcbi.1004209.
- Nieuwenhuys, R. (1994). The neocortex. An overview of its evolutionary development, structural organization and synaptology. *Anatomy and Embryology*, 190(4), 307-337. doi: 10.1007/bf00187291.
- Nunez, P. L., Srinivasan, R., & Press, O. U. (2006). *Electric Fields of the Brain: The Neurophysics of EEG*. Oxford University Press.
- Oberlaender, M., Boudewijns, Z. S., Kleele, T., Mansvelder, H. D., Sakmann, B., & de Kock, C. P. (2011). Three-dimensional axon morphologies of individual layer 5 neurons indicate cell type-specific intracortical pathways for whisker motion and touch. *Proceedings of the National Academy of Sciences*, 108(10), 4188-4193. doi: 10.1073/pnas.1100647108.

- Palus, M., & Vejmelka, M. (2007). Directionality of coupling from bivariate time series: How to avoid false causalities and missed connections. *Physical Review E*, 75(5 Pt 2), 056211. doi: 10.1103/PhysRevE.75.056211.
- Panzeri, S., Schultz, S. R., Treves, A., & Rolls, E. T. (1999). Correlations and the encoding of information in the nervous system. *Proceedings of the Royal Society B: Biological Sciences*, 266(1423), 1001-1012. doi: 10.1098/rspb.1999.0736.
- Pearson, K. (1901). On lines and planes of closest fit to systems of points in space. *The London, Edinburgh, and Dublin Philosophical Magazine and Journal of Science*, 2(11), 559–572. doi: 10.1080/14786440109462720.
- Penfield, W., & Jasper, H. (1954). *Epilepsy and the functional anatomy of the human brain*. Little, Brown & Co.
- Pichon, F., Nikonenko, I., Kraftsik, R., & Welker, E. (2012). Intracortical connectivity of layer VI pyramidal neurons in the somatosensory cortex of normal and barrelless mice. *European Journal of Neuroscience*, 35(6), 855-869. doi: 10.1111/j.1460-9568.2012.08011.x
- Pincus, S. M. (1991). Approximate entropy as a measure of system complexity. *Proceedings of the National Academy of Sciences*, 88(6), 2297-2301. doi: 10.1073/pnas.88.6.2297
- Pineda-Pardo, J. A., Bruña, R., Woolrich, M., Marcos, A., Nobre, A. C., Maestú, F., & Vidaurre, D. (2014). Guiding functional connectivity estimation by structural connectivity in MEG: An application to discrimination of conditions of mild cognitive impairment. *NeuroImage*, 101, 765-777. doi: 10.1016/j.neuroimage.2014.08.002
- Poduri, A., & Lowenstein, D. (2011). Epilepsy genetics--past, present, and future. *Current Opinion in Genetics & Development*, 21(3), 325-332. doi: 10.1016/j.gde.2011.01.005.
- Quiroga, R. Q., & Panzeri, S. (2009). Extracting information from neuronal populations: Information theory and decoding approaches. *Nature Reviews Neuroscience*, 10(3), 173-185. doi: 10.1038/nrn2578
- Quiroga, R. Q., Nadasdy, Z., & Ben-Shaul, Y. (2004). Unsupervised spike detection and sorting with wavelets and superparamagnetic clustering. *Neural Computation*, 16(8), 1661-1687. doi: 10.1162/089976604774201631
- Rajakulendran, S., & Hanna, M. G. (2016). The Role of Calcium Channels in Epilepsy. *Cold Spring Harbor Perspectives in Medicine*, 6(1), a022723. doi: 10.1101/cshperspect.a022723.
- Rezayev, A., Feldman, H. A., Levman, J., & Takahashi, E. (2018). Bilateral thalamocortical abnormalities in focal cortical dysplasia. *Brain Research*, 1694, 38-45. doi: 10.1016/j.brainres.2018.05.005
- Riehle, A., Grün, S., Diesmann, M., & Aertsen, A. (1997). Spike synchronization and rate modulation differentially involved in motor cortical function. *Science*, 278, 1950–1953. doi: 10.1126/science.278.5345.1950
- Rogawski, M. A. (2013). AMPA receptors as a molecular target in epilepsy therapy. *Acta Neurologica Scandinavica Supplementum*, (197), 9-18. doi: 10.1111/ane.12099

- Roscoe, D. D., Hamm, T. M., Reinking, R. M., & Stuart, D. G. (1985). Detection of synchrony in the discharge of a population of neurons. II. Implementation and sensitivity of a synchronization index. *Journal of Neuroscience Methods*, 13, 51–64. doi: 10.1016/0165-0270(85)90043-3
- Rubinov, M., & Sporns, O. (2010). Complex network measures of brain connectivity: Uses and interpretations. *NeuroImage*, 52(3), 1059-1069. doi: 10.1016/j.neuroimage.2009.10.003
- Rudy, B., Fishell, G., Lee, S., & Hjerling-Leffler, J. (2011). Three groups of interneurons account for nearly 100% of neocortical GABAergic neurons. *Developmental Neurobiology*, 71(1), 45-61. doi: 10.1002/dneu.20853
- Russo, E., & Durstewitz, D. (2017). Cell assemblies at multiple time scales with arbitrary lag constellations. *eLife*, 6, e19428. doi: 10.7554/eLife.19428
- Rust, N. C., Schwartz, O., Movshon, J. A., & Simoncelli, E. (2004). Spike-triggered characterization of excitatory and suppressive stimulus dimensions in monkey V1. *Neurocomputing*, 58-60, 793-799. doi: 10.1016/j.neucom.2004.01.128
- Rutecki, P. A., Lebeda, F. J., & Johnston, D. (1985). Epileptiform activity induced by changes in extracellular potassium in hippocampus. *Journal of Neurophysiology*, 54(5), 1363-1374.
- Ryvlin, P., & Rheims, S. (2008). Epilepsy surgery: Eligibility criteria and presurgical evaluation. *Dialogues in Clinical Neuroscience*, 10(1), 91-103. doi: 10.31887/DCNS.2008.10.1/ryvlin
- Saenger, V. M., Ponce-Alvarez, A., Adhikari, M., Hagmann, P., Deco, G., & Corbetta, M. (2018). Linking entropy at rest with the underlying structural connectivity in the healthy and lesioned brain. *Cerebral Cortex*, 28(8), 2948-2958. doi: 10.1093/cercor/bhx176
- Salfenmoser, L., & Obermayer, K. (2022). Nonlinear optimal control of a mean-field model of neural population dynamics. *Frontiers in Computational Neuroscience*, 16, 931121. doi: 10.3389/fncom.2022.931121
- Salpekar, J. (2016). Mood disorders in epilepsy. *Focus (American Psychiatric Publishing)*, 14(4), 465-472. doi: 10.1176/appi.focus.20160017
- Saper, C. B., Fuller, P. M., Pedersen, N. P., Lu, J., & Scammell, T. E. (2010). Sleep state switching. *Neuron*, 68, 1023–1042. doi: 10.1016/j.neuron.2010.11.032
- Scheffer, I. E., Berkovic, S., Capovilla, G., Connolly, M. B., French, J., Guilhoto, L., ... Zuberi, S. M. (2017). ILAE classification of the epilepsies: Position paper of the ILAE Commission for Classification and Terminology. *Epilepsia*, 58(4), 512-521. doi: 10.1111/epi.13709
- Schevon, C. A., Weiss, S. A., McKhann, G. Jr., Goodman, R. R., Yuste, R., Emerson, R. G., & Trevelyan, A. J. (2012). Evidence of an inhibitory restraint of seizure activity in humans. *Nature Communications*, 3, 1060. doi: 10.1038/ncomms2056

- Schneidman, E., Berry, M. J., Segev, R., & Bialek, W. (2006). Weak pairwise correlations imply strongly correlated network states in a neural population. *Nature*, 440, 1007–1012. doi: 10.1038/nature04701
- Schreiber, T. (2000). Measuring information transfer. *Physical Review Letters*, 85(2), 461-464. doi: 10.1103/PhysRevLett.85.461
- Shamim, S., Hasler, G., Liew, C., Sato, S., & Theodore, W. H. (2009). Temporal lobe epilepsy, depression, and hippocampal volume. *Epilepsia*, 50(5), 1067-1071. doi: 10.1111/j.1528-1167.2008.01883.x
- Shannon, C. E. (1948). The mathematical theory of communication. *MD Computing: Computers in Medical Practice*, 14(4), 306-317.
- Shefchyk, S. J., & Jordan, L. M. (1985). Excitatory and inhibitory postsynaptic potentials in alpha-motoneurons produced during fictive locomotion by stimulation of the mesencephalic locomotor region. *Journal of Neurophysiology*, 53(6), 1345-1355. doi: 10.1152/jn.1985.53.6.1345
- Singer, W. (1999). Neuronal synchrony: A versatile code for the definition of relations? *Neuron*, 24, 49-65. doi: 10.1016/S0896-6273(00)80821-1
- Skaggs, W. E., & McNaughton, B. L. (1996). Replay of neuronal firing sequences in rat hippocampus during sleep following spatial experience. *Science*, 271, 1870-1873. doi: 10.1126/science.271.5257.1870
- Smith, E. H., Liou, J. Y., Davis, T. S., Merricks, E. M., Kellis, S. S., Weiss, S. A., ... Schevon, C. A. (2016). The ictal wavefront is the spatiotemporal source of discharges during spontaneous human seizures. *Nature Communications*, 7, 11098. doi: 10.1038/ncomms11098
- Souza, B. C., Lopes-Dos-Santos, V., Bacelo, J., & Tort, A. B. L. (2019). Spike sorting with Gaussian mixture models. *Scientific Reports*, 9(1), 3627. doi: 10.1038/s41598-019-39986-6
- Spencer, S. S. (2002). When should temporal-lobe epilepsy be treated surgically? *The Lancet Neurology*, 1(6), 375-382. doi: 10.1016/S1474-4422(02)00163-1
- Sporns, O., Kötter, R. (2004). Motifs in brain networks. *PLoS Biology*, 2(11), e369. doi: 10.1371/journal.pbio.0020369
- Sporns, O., Tononi, G., & Edelman, G. M. (2000). Connectivity and complexity: The relationship between neuroanatomy and brain dynamics. *Neural Networks*, 13(8-9), 909-922. doi: 10.1016/S0893-6080(00)00053-8
- Sporns, O., Zwi, J. D. (2004). The small world of the cerebral cortex. *Neuroinformatics*, 2(2), 145-162. doi: 10.1385/NI:2:2:145
- Stafstrom, C. E., & Carmant, L. (2015). Seizures and epilepsy: An overview for neuroscientists. *Cold Spring Harbor Perspectives in Medicine*, 5(6), a022426.

- Staley, K. J., & Dudek, F. E. (2006). Interictal spikes and epileptogenesis. *Epilepsy Currents*, 6(6), 199-202.
- Staley, K. J. (2006). Wrong-way chloride transport: is it a treatable cause of some intractable seizures? *Epilepsy Currents*, 6(4), 124-127.
- Stam, C. J., van Straaten, E. C., Van Dellen, E., Tewarie, P., Gong, G., Hillebrand, A., ... Van Mieghem, P. (2016). The relation between structural and functional connectivity patterns in complex brain networks. *International Journal of Psychophysiology*, 103, 149-160. doi: 10.1016/j.ijpsycho.2015.02.011
- Stella, A., Bouss, P., Palm, G., & Grün, S. (2022). Comparing surrogates to evaluate precisely timed higher-order spike correlations. *eNeuro*, doi: 10.1523/ENEURO.0505-21.2022
- Strack, B., Jacobs, K. M., & Cios, K. J. (2013). Biological restraint on the Izhikevich neuron model essential for seizure modeling. *International IEEE EMBS Conference on Neural Engineering*, 395-398. doi: 10.1109/ner.2013.6695955
- Smith, G. A., Henry, J., van Drongelen, W. (2023). Detecting heterogeneous seizures in newborn infants using triple correlation. *medRxiv* 2023.06.09.23291216; doi: <https://doi.org/10.1101/2023.06.09.23291216>.
- Suresh, J., Radojicic, M., Pesce, L. L., Bhansali, A., Wang, J., Tryba, A. K., Marks, J. D., & van Drongelen, W. (2016). Network burst activity in hippocampal neuronal cultures: the role of synaptic and intrinsic currents. *Journal of neurophysiology*, 115(6), 3073–3089. doi.org/10.1152/jn.00995.2015
- Suresh, J., Saddler, M., Bindokas, V., Bhansali, A., Pesce, L., Wang, J., Marks, J., van Drongelen, W. (2023). Emerging activity patterns and synaptogenesis in dissociated hippocampal cultures. *bioRxiv*. 05.18.541345. doi: <https://doi.org/10.1101/2023.05.18.541345>
- Tagliazucchi, E., Behrens, M., & Laufs, H. (2013). Sleep neuroimaging and models of consciousness. *Frontiers in Psychology*, 4, 256. doi: 10.3389/fpsyg.2013.00256
- Takahashi, S., Anzai, Y., & Sakurai, Y. (2003). A new approach to spike sorting for multi-neuronal activities recorded with a tetrode--how ICA can be practical. *Neuroscience Research*, 46(3), 265-272. doi: 10.1016/s0168-0102(03)00103-2
- Tang, F., Hartz, A. M. S., & Bauer, B. (2017). Drug-Resistant Epilepsy: Multiple Hypotheses, Few Answers. *Frontiers in Neurology*, 8, 301. doi: 10.3389/fneur.2017.00301
- Taylor, P. N., Han, C. E., Schoene-Bake, J. C., Weber, B., & Kaiser, M. (2015). Structural connectivity changes in temporal lobe epilepsy: Spatial features contribute more than topological measures. *NeuroImage: Clinical*, 8, 322-328. doi: 10.1016/j.nicl.2015.02.004
- Telenczuk, B., Dehghani, N., Le Van Quyen, M., Cash, S. S., Halgren, E., Hatsopoulos, N. G., & Destexhe, A. (2017). Local field potentials primarily reflect inhibitory neuron activity in human and monkey cortex. *Scientific Reports*, 7, 40211. doi: 10.1038/srep40211

- Thijs, R. D., Surges, R., O'Brien, T. J., & Sander, J. W. (2019). Epilepsy in adults. *The Lancet*, 393(10172), 689-701. doi: 10.1016/S0140-6736(18)32596-0
- Tononi, G., & Edelman, G. M. (1998). Consciousness and complexity. *Science*, 282, 1846–1851. doi: 10.1126/science.282.5395.1846
- Tononi, G., & Koch, C. (2015). Consciousness: Here, there and everywhere? *Philosophical Transactions of the Royal Society B: Biological Sciences*, 370, 20140167. doi: 10.1098/rstb.2014.0167
- Tort, A. B. L., Komorowski, R. W., Manns, J. R., Kopell, N. J., & Eichenbaum, H. (2009). Theta-gamma coupling increases during the learning of item-context associations. *Proceedings of the National Academy of Sciences*, 106, 20942–20947. doi: 10.1073/pnas.0911331106
- Traub, R. D., Wong, R. K., Miles, R., & Michelson, H. (1991). A model of a CA3 hippocampal pyramidal neuron incorporating voltage-clamp data on intrinsic conductances. *Journal of Neurophysiology*, 66(2), 635-650. doi: 10.1152/jn.1991.66.2.635
- Traub, R. D., & Wong, R. K. (1982). Cellular mechanism of neuronal synchronization in epilepsy. *Science*, 216(4547), 745-747. doi: 10.1126/science.7079735
- Trevelyan, A. J., Sussillo, D., Watson, B. O., & Yuste, R. (2006). Modular propagation of epileptiform activity: evidence for an inhibitory veto in neocortex. *The Journal of Neuroscience*, 26(48), 12447-12455. doi: 10.1523/JNEUROSCI.2787-06.2006
- Truccolo, W., Ahmed, O. J., Harrison, M. T., Eskandar, E. N., Cosgrove, G. R., Madsen, J. R., Blum, A. S., Potter, N. S., Hochberg, L. R., & Cash, S. S. (2014). Neuronal ensemble synchrony during human focal seizures. *The Journal of Neuroscience*, 34(30), 9927-9944. doi: 10.1523/JNEUROSCI.4567-13.2014
- Truccolo, W., Donoghue, J. A., Hochberg, L. R., Eskandar, E. N., Madsen, J. R., Anderson, W. S., Brown, E. N., Halgren, E., & Cash, S. S. (2011). Single-neuron dynamics in human focal epilepsy. *Nature Neuroscience*, 14(5), 635-641. doi: 10.1038/nn.2782
- Tryba, A. K., Merricks, E. M., Lee, S., Pham, T., Cho, S., Nordli, D. R., Jr., Eissa, T. L., Goodman, R. R., McKhann, G. M., Jr., Emerson, R. G., Schevon, C. A., & van Drongelen, W. (2019). Role of paroxysmal depolarization in focal seizure activity. *Journal of Neurophysiology*, 122(5), 1861-1873. doi: 10.1152/jn.00392.2019
- van den Heuvel, M. P., & Sporns, O. (2011). Rich-club organization of the human connectome. *Journal of Neuroscience*, 31(44), 15775-15786. doi: 10.1523/JNEUROSCI.3539-11.2011
- van Drongelen, W. (2018). *Signal Processing for Neuroscientists: Introduction to the Analysis of Physiological Signals* (2nd ed.). Elsevier/Academic Press.
- van Elst, L. T., Thiel, T., Hesslinger, B., Lieb, K., Bohus, M., Hennig, J., & Ebert, D. (2001). Subtle prefrontal neuropathology in a pilot magnetic resonance spectroscopy study in patients with borderline personality disorder. *Journal of Neuropsychiatry and Clinical Neurosciences*, 13(4), 511-514. doi: 10.1176/jnp.13.4.511

- Victor, J. D. (1994). Images, statistics, and textures: Implications of triple correlation uniqueness for texture statistics and the Julesz conjecture: Comment. *Journal of the Optical Society of America A*, 11, 1680-1684. doi: 10.1364/JOSAA.11.001680
- Vining, E. P. (1986). Use of barbiturates and benzodiazepines in treatment of epilepsy. *Neurologic Clinics*, 4, 617-632.
- Wasterlain, C. G., & Chen, J. W. (2008). Mechanistic and pharmacologic aspects of status epilepticus and its treatment with new antiepileptic drugs. *Epilepsia*, 49(Suppl 9), 63-73. doi: 10.1111/j.1528-1167.2008.01928.x
- Watts, D. J., & Strogatz, S. H. (1998). Collective dynamics of 'small-world' networks. *Nature*, 393(6684), 440-442. doi: 10.1038/30918
- Weiss, S. A., Banks, G. P., McKhann, G. M., Jr., Goodman, R. R., Emerson, R. G., Trevelyan, A. J., & Schevon, C. A. (2013). Ictal high frequency oscillations distinguish two types of seizure territories in humans. *Brain*, 136(Pt 12), 3796-3808. doi: 10.1093/brain/awt276
- Wendling, F., Bartolomei, F., Bellanger, J. J., & Chauvel, P. (2002). Epileptic fast activity can be explained by a model of impaired GABAergic dendritic inhibition. *European Journal of Neuroscience*, 15(9), 1499-1508. doi: 10.1046/j.1460-9568.2002.01985.x
- Wilson, H. R., & Cowan, J. D. (1972). Excitatory and inhibitory interactions in localized populations of model neurons. *Biophysical Journal*, 12(1), 1-24. doi: 10.1016/S0006-3495(72)86068-5
- Yellott, J. I., & Iverson, G. J. (1992). Uniqueness properties of higher-order autocorrelation functions. *Journal of the Optical Society of America A*, 9, 388-404. doi: 10.1364/JOSAA.9.000388
- Yellott, J. I. (1993). Implications of triple correlation uniqueness for texture statistics and the Julesz conjecture. *Journal of the Optical Society of America A*, 10, 777-793. doi: 10.1364/JOSAA.10.000777
- Ying, T., Grayden, D. B., Burkitt, A. N., & Kamenova, T. (2015). An increase in the extracellular potassium concentration can cause seizures. *BMC Neuroscience*, 16(Suppl 1), P113.
- Yu, S., et al. (2011). Higher-order interactions characterized in cortical activity. *Journal of Neuroscience*, 31, 17514-17526. doi: 10.1523/JNEUROSCI.3127-11.2011
- Zhang, P. M., Wu, J. Y., Zhou, Y., Liang, P. J., & Yuan, J. Q. (2004). Spike sorting based on automatic template reconstruction with a partial solution to the overlapping problem. *Journal of Neuroscience Methods*, 135(1-2), 55-65. doi: 10.1016/j.jneumeth.2003.12.001
- Zhang, Z. W., & Deschênes, M. (1997). Intracortical axonal projections of lamina VI cells of the primary somatosensory cortex in the rat: a single-cell labeling study. *Journal of Neuroscience*, 17(16), 6365-6379. doi: 10.1523/jneurosci.17-16-06365.1997

APPENDIX

A.1 Application of Triple Correlation to MEA Spiking Activity

A.1.1 *Rhesus macaques completing an instructed, reach-to-grasp task*

Since the publishing of Chapter 3, we have been working on applying the triple correlation work to various datasets. One such open-source dataset is of action potential spiking activity recorded from a Utah array (10x10, 96-channel, 4 mm x 4 mm array) implanted in motor cortex of rhesus macaques completing a reach-to-grasp task (Brochier *et al.*, 2018). Triple correlation was computed across four conditions: the cue period, delay period, reaction time, and reach-to-grasp time (Fig. A.1). Motif classes I & II (indicative of second-order and third-order autocorrelation) show the highest values, suggesting that individual channel activity mostly governs the underlying network structure. In addition, motif classes III (second-order synchrony), IV (third-order synchrony), V (spike propagation), XI (divergence), XII (convergence), and XIII (feedforward) fluctuate around 0 for each of the four conditions, which indicate that these network structures are comparable to chance. Lastly, while the reach-to-grasp period does show the highest network structure for motif classes VI-X (which are triplet motifs), they do not deviate from 0 as much as motif class I & II, which suggests that inter-channel interactions do not govern the overall network activity as much as individual channel activity. This could be attributed to inter-electrode distance among the microelectrodes within the Utah array; the microelectrodes are spaced $\sim 400\ \mu\text{m}$ apart. These preliminary results suggest that MEAs with smaller inter-electrode distances (as shown in the culture data from Fig. 3.5 in Chapter 3 and Fig. 4.3 in Chapter 4) would capture inter-neuronal or inter-channel network structure.

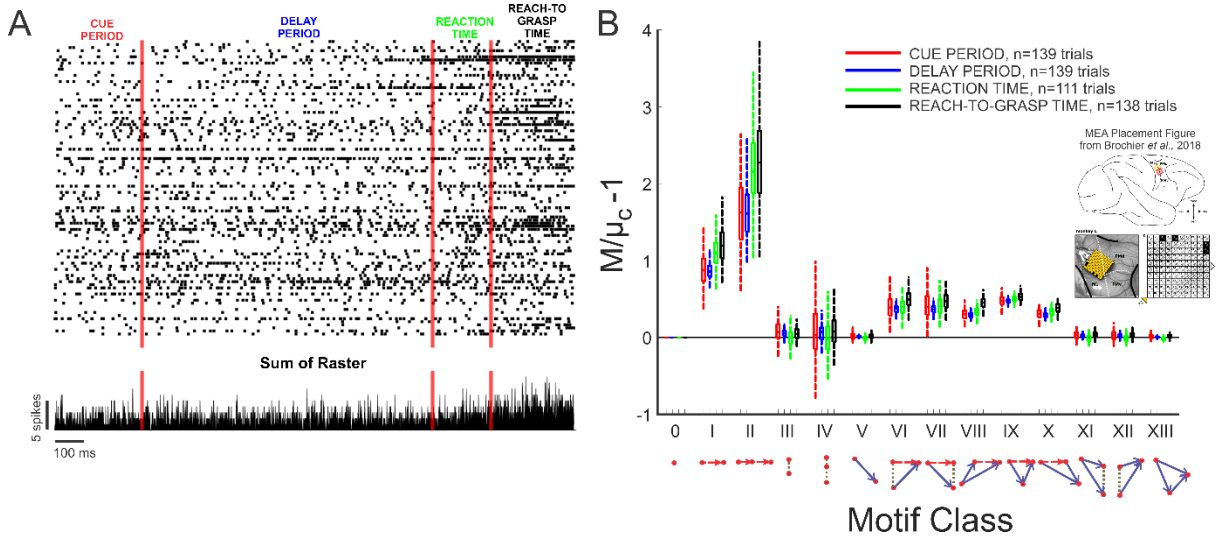


Figure A.1: Network characterization of monkey spiking activity from completing a reach-to-grasp task using triple correlation. A) Example spike raster and sum of raster for each of the four conditions. B) Triple correlation shows the highest network structure during the reach-to-grasp time for all fourteen motif classes (one-way ANOVA, $*p < 0.05$). In addition, network dynamics are highest for motif classes I & II, indicative of individual channel activity.

A.2 Supplemental Materials for Triple Correlation¹

A.2.1 Uniqueness of Triple Correlation for Network Spiking Activity

We represent neuronal activity as a typical two-dimensional raster, $x(n, t)$, where n is neuron location and t is time. We assume that the raster is a binary (black and white, cf. Fig. 1A), meaning $x(n, t) = 1$ if neuron n fires at time t , and $x(n, t) = 0$ otherwise. We note that the reasoning in the proofs below works just as well for any raster taking bounded values analogous to a greyscale image, such as would be the case with local field potential recordings or the electroencephalogram. The reasoning below applies to any finite bounded dataset. The triple correlation of $x(n, t)$ is:

¹The mathematics derived in Sections A.2.1, A.2.2, A.2.3, A.2.8, A.2.9, and A.2.10 were generated by Graham Smith (a fellow lab member in van Drongelen lab) and are included here in the Appendix for reference purposes as a continuation from Chapter 3.

$$c_3(v_1, \tau_1, v_2, \tau_2) = \iint x(n, t)x(n + v_1, t + \tau_1)x(n + v_2, t + \tau_2)dn dt \quad (\text{Equation A.2})$$

for spatial lags v_1, v_2 and temporal lags τ_1, τ_2 . This is the triple correlation function that the TCU theorem shows uniquely characterizes the spike raster. We define $\mathcal{F}[c_3]$ as the Fourier transform of c_3 , which means:

$$\begin{aligned} \mathcal{F}[c_3](\sigma_1, \omega_1, \sigma_2, \omega_2) = \\ \iiint c_3(v_1, \tau_1, v_2, \tau_2)e^{-j\sigma_1 v_1}e^{-j\omega_1 \tau_1}e^{-j\sigma_2 v_2}e^{-j\omega_2 \tau_2}dv_1 d\tau_1 dv_2 d\tau_2 \end{aligned} \quad (\text{Equation A.3})$$

We can rewrite this integral in terms of the Fourier transform of x by substituting Equation A.2 into Equation A.3 and rearranging the integration order to find

$$\begin{aligned} \mathcal{F}[c_3](\sigma_1, \omega_1, \sigma_2, \omega_2) \\ = \iiint x(n, t)x(n + v_2, t + \tau_2) \left[\iint x(n + v_1, t + \tau_1)e^{-j\sigma_1 v_1}e^{-j\omega_1 \tau_1}dv_1 d\tau_1 \right] \\ e^{-j\sigma_2 v_2}e^{-j\omega_2 \tau_2}dv_2 d\tau_2 dn dt \end{aligned} \quad (\text{Equation A.4})$$

The part in between the $[\dots]$ in Equation A.4 can be rewritten as $e^{j\omega_1 t}e^{j\sigma_1 n}X(\sigma_1, \omega_1)$, with $X(\sigma_1, \omega_1)$ denoting the two dimensional Fourier transform of $x(v_1, \tau_1)$. Similarly, the part of Equation A.4 for v_2 and τ_2 and their double integral can be arranged to evaluate to $e^{j\omega_2 t}e^{j\sigma_2 n}X(\sigma_2, \omega_2)$. Substitution of these results in Equation A.4 results in:

$$\mathcal{F}[c_3](\sigma_1, \omega_1, \sigma_2, \omega_2) = X(\sigma_1, \omega_1)X(\sigma_2, \omega_2)\iint x(n, t)e^{j(\omega_1 + \omega_2)t}e^{j(\sigma_1 + \sigma_2)n}dn dt \quad (\text{Equation A.5})$$

The double integral evaluates to $X(-\sigma_1 - \sigma_2, -\omega_1 - \omega_2) = X^*(\sigma_1 + \sigma_2, \omega_1 + \omega_2)$, where the asterisk denotes a complex conjugate. Thus we see that the Fourier transform of c_3 is the bispectrum:

$$\mathcal{F}[c_3(v_1, \tau_1, v_2, \tau_2)] = X(\sigma_1, \omega_1)X(\sigma_2, \omega_2)X^*(\sigma_1 + \sigma_2, \omega_1 + \omega_2) \quad (\text{Equation A.6})$$

This relationship between triple correlation and the bispectrum is the third-order equivalent of the Wiener-Khinchin-Einstein theorem.

Since images have a finite support and all of the above integration limits are implicitly at $(-\infty, \infty)$, we can modify the results for finite support by multiplying the spatiotemporal domain data by a two-dimensional boxcar window, w , limited between $(-\Sigma, \Sigma, -\Omega, \Omega)$ (or any other window with that support): $= xw$. The frequency domain results are then characterized by the Fourier transforms convolved (denoted by \circledast) with the boxcar's Fourier transform (W) (or that of the window applied) denoted by: $= X \circledast W$. By using this notation, the results in equations A.3-A.2 would be adapted by adding the b and B subscripts.

Yellott and Iverson (1992) show in a constructive proof that a finite image (in our case a spike raster of a finite size) can be uniquely reconstructed from its third-order correlation. These authors also show and discuss how this does not hold for images of infinite size. Here we do not further discuss this aspect because the size of a spike raster (or a snapshot of any modality of neural activity) is always finite.

One critically important message of this paper is that the time domain's triple correlation and the corresponding bispectrum in the frequency domain uniquely determine the firing pattern of a network. Yellott (1993) presents this as the TCU theorem. If we apply Yellott's TCU theorem to a spike raster, we get the following.

Theorem 1. If $x(n, t)$ is a raster with bounded support and another raster $y(n, t)$ has the same triple correlation function as that of x , then $y(n, t) = x(n + a, t + b)$ for a pair of constants a, b .

Theorem 2. If $x(\mathbf{s})$ is a raster with bounded support in N spatial dimensions and another raster $y(\mathbf{s})$ has the same triple correlation function as that of x , then $y(\mathbf{s}) = x(\mathbf{s} + \mathbf{a})$ for a vector of constants \mathbf{a} .

Here we present proofs in line with the proof in Yellott and Iverson's (1992) for two- and N -dimensional spatiotemporal data.

A.2.2 Proof of Theorem 1 (two dimensions)

Given the equality of third-order correlation functions, we can use Equation A.2 to find that

$$\begin{aligned} X(\sigma_1, \omega_1)X(\sigma_2, \omega_2)X(-\sigma_1 - \sigma_2, -\omega_1 - \omega_2) = \\ Y(\sigma_1, \omega_1)Y(\sigma_2, \omega_2)Y(-\sigma_1 - \sigma_2, -\omega_1 - \omega_2) \end{aligned} \quad (\text{Equation A.7})$$

To borrow some convenient results from probability theory (see any introductory text, e.g.), we note that X and Y can be considered characteristic functions since we can consider x and y probability distributions: as finite images, x and y are bounded and nonnegative, and without loss of generality we can normalize them such that their integral is 1. Characteristic functions (the Fourier transforms of probability distributions) have two properties that are convenient for our purposes, the first of which is that they are non-zero in a region around the origin, thus allowing us the following division (for further considerations of rigor in the one-dimensional case, see Moszner, 1980):

$$\frac{X(\sigma_1, \omega_1)X(\sigma_2, \omega_2)}{Y(\sigma_1, \omega_1)Y(\sigma_2, \omega_2)} = \frac{Y(-\sigma_1 - \sigma_2, -\omega_1 - \omega_2)}{X(-\sigma_1 - \sigma_2, -\omega_1 - \omega_2)} \quad (\text{Equation A.8})$$

Next we rewrite both complex functions in terms of their amplitude and phase, i.e. $X(\sigma, \omega) = |X(\sigma, \omega)| e^{j\phi(X(\sigma, \omega))}$, where ϕ gives the phase. So we can rewrite the right-hand side of Equation A.8 as:

$$\frac{X(\sigma_1, \omega_1)X(\sigma_2, \omega_2)}{Y(\sigma_1, \omega_1)Y(\sigma_2, \omega_2)} = \frac{|Y(-\sigma_1 - \sigma_2, -\omega_1 - \omega_2)|e^{j\phi(Y(-\sigma_1 - \sigma_2, -\omega_1 - \omega_2))}}{|X(-\sigma_1 - \sigma_2, -\omega_1 - \omega_2)|e^{j\phi(X(-\sigma_1 - \sigma_2, -\omega_1 - \omega_2))}}$$

(Equation A.9)

Here we use the second convenient property of characteristic functions, namely

that they are Hermitian, i.e. $X(-\sigma, -\omega) = X^*(\sigma, \omega)$. By setting $\sigma_2 = 0, \omega_2 = 0$ in (A.9),

we can use this Hermitian property to derive the fact that $|X(\sigma_1, \omega_1)|^2 = |Y(\sigma_1, \omega_1)|^2$

for any σ_1, ω_1 . In particular, $|X(-\sigma_1 - \sigma_2, -\omega_1 - \omega_2)| = |Y(-\sigma_1 - \sigma_2, -\omega_1 - \omega_2)|$ so

we can flip those terms.

$$= \frac{|X(-\sigma_1 - \sigma_2, -\omega_1 - \omega_2)|e^{j\phi(Y(-\sigma_1 - \sigma_2, -\omega_1 - \omega_2))}}{|Y(-\sigma_1 - \sigma_2, -\omega_1 - \omega_2)|e^{j\phi(X(-\sigma_1 - \sigma_2, -\omega_1 - \omega_2))}}$$

(Equation A.10)

We can also rewrite those same terms thanks to the same Hermitian property.

$$= \frac{|X^*(\sigma_1 + \sigma_2, \omega_1 + \omega_2)|e^{j\phi(Y^*(\sigma_1 + \sigma_2, \omega_1 + \omega_2))}}{|Y^*(\sigma_1 + \sigma_2, \omega_1 + \omega_2)|e^{j\phi(X^*(\sigma_1 + \sigma_2, \omega_1 + \omega_2))}}$$

(Equation A.11)

Simple complex properties are $|X| = |X^*|$ and $\phi(X) = -\phi(X^*)$, which give us

$$= \frac{|X(\sigma_1 + \sigma_2, \omega_1 + \omega_2)|e^{j\phi(Y(\sigma_1 + \sigma_2, \omega_1 + \omega_2))}}{|Y(\sigma_1 + \sigma_2, \omega_1 + \omega_2)|e^{j\phi(X(\sigma_1 + \sigma_2, \omega_1 + \omega_2))}}$$

(Equation A.12)

Next, we return from the amplitude and phase notation to the complex functions themselves:

$$= \frac{X(\sigma_1 + \sigma_2, \omega_1 + \omega_2)}{Y(\sigma_1 + \sigma_2, \omega_1 + \omega_2)}$$

(Equation A.13)

Now we define $H(\sigma, \omega) = \frac{X(\sigma, \omega)}{Y(\sigma, \omega)}$ so we can rewrite Equation A.13 as

$$H(\sigma_1, \omega_1)H(\sigma_2, \omega_2) = H(\sigma_1 + \sigma_2, \omega_1 + \omega_2) \quad (\text{Equation A.14})$$

Therefore, by a basic result of complex analysis $H(\sigma, \omega) = e^{j(a\sigma+b\omega)}$, and thus

$$Y(\sigma, \omega) = X(\sigma, \omega)e^{j(a\sigma+b\omega)} \quad (\text{Equation A.15})$$

This holds in a region near the origin, and another property of characteristic functions is that, if their probability distribution has finite support, the probability distribution is uniquely determined by the value of the characteristic function in a region of the origin. Thus, in the spatiotemporal domain,

$$y(n, t) = x(n + a, t + b) \text{ with constants } a, b \quad (\text{Equation A.16})$$

A.2.3 Proof of Theorem 2 (N dimensions)

Here we extend the preceding proof to N dimensions. This would be necessary for analysing many clinical and experimental data sources, e.g. the plane of a two-dimensional micro-electrode array produces $2 + 1$ dimensional data (as in our example presented in Fig. A.5). Even higher dimensions may be useful in the case where long-range connections can be represented as a hidden dimension (e.g. orientation tuning in V1). The proof is generic enough that in practice the result applies to all finite datasets.

Note that the number of motifs (i.e. the size of the triple correlation matrix) scales with exponent $2N + 2$.

We define the $N + 1$ -dimensional spatiotemporal vector variable $\mathbf{s} = (x_1, x_2, \dots, x_N, t)$. Then we notate the triple correlation of an N dimensional raster as $c_T(\mathbf{s}_1, \mathbf{s}_2)$. We notate the $N + 1$ -dimensional variable's Fourier transform as

$$\mathcal{F}[\mathbf{s}] = \mathbf{\Omega} = (\sigma_1, \sigma_2, \dots, \sigma_N, \omega) \quad (\text{Equation A.17})$$

and the corresponding bispectrum as $c_T(\mathbf{\Omega}_1, \mathbf{\Omega}_2)$.

Since the properties of characteristic functions that are key to this proof still hold in N dimensions (see any introductory probability theory text, e.g. Feller, 1950), the proof proceeds identically to that in two dimensions, but with vector notation.

Given the equality of third-order correlation functions, we can use Equation A.17 to find that $X(\mathbf{\Omega}_1)X(\mathbf{\Omega}_2)X(-\mathbf{\Omega}_1 - \mathbf{\Omega}_2) = Y(\mathbf{\Omega}_1)Y(\mathbf{\Omega}_2)Y(-\mathbf{\Omega}_1 - \mathbf{\Omega}_2)$ (Equation A.18)

To borrow some convenient results from probability theory, we note that X and Y can be considered characteristic functions since we can consider x and y probability distributions: as finite images, x and y are bounded and nonnegative, and without loss of generality we can normalize them such that their integral is 1. Characteristic functions (the Fourier transforms of probability distributions) have two properties that are convenient for our purposes, the first of which is that they are non-zero in a region around the origin, thus allowing us the following division (for further considerations of rigor in the one-dimensional case, see Moszner, 1980):

$$\frac{X(\mathbf{\Omega}_1)X(\mathbf{\Omega}_2)}{Y(\mathbf{\Omega}_1)Y(\mathbf{\Omega}_2)} = \frac{Y(-\mathbf{\Omega}_1 - \mathbf{\Omega}_2)}{X(-\mathbf{\Omega}_1 - \mathbf{\Omega}_2)} \quad (\text{Equation A.19})$$

Next, we rewrite both complex functions in terms of their amplitude and phase, i.e.

i.e. $X(\mathbf{\Omega}) = |X(\mathbf{\Omega})| e^{j\phi(X(\mathbf{\Omega}))}$, where ϕ gives the phase. So then we can rewrite the

right-hand side of Equation A.19:

$$\frac{X(\mathbf{\Omega}_1)X(\mathbf{\Omega}_2)}{Y(\mathbf{\Omega}_1)Y(\mathbf{\Omega}_2)} = \frac{|Y(-\mathbf{\Omega}_1 - \mathbf{\Omega}_2)| e^{j\phi(X(-\mathbf{\Omega}_1 - \mathbf{\Omega}_2))}}{|X(-\mathbf{\Omega}_1 - \mathbf{\Omega}_2)| e^{j\phi(Y(-\mathbf{\Omega}_1 - \mathbf{\Omega}_2))}} \quad (\text{Equation A.20})$$

Here we use the second convenient property of characteristic functions, namely that they are Hermitian, i.e. $X(-\mathbf{\Omega}) = X^*(\mathbf{\Omega})$. By setting $\mathbf{\Omega}_2 = 0$ in (A.20), we can use this Hermitian property to derive the fact that $|X(\mathbf{\Omega}_1)|^2 = |Y(\mathbf{\Omega}_1)|^2$ for any $\mathbf{\Omega}_1$. In particular, $|X(-\mathbf{\Omega}_1 - \mathbf{\Omega}_2)| = |Y(-\mathbf{\Omega}_1 - \mathbf{\Omega}_2)|$ so we can flip those terms:

$$= \frac{|X(-\mathbf{\Omega}_1 - \mathbf{\Omega}_2)| e^{j\phi(Y(-\mathbf{\Omega}_1 - \mathbf{\Omega}_2))}}{|Y(-\mathbf{\Omega}_1 - \mathbf{\Omega}_2)| e^{j\phi(X(-\mathbf{\Omega}_1 - \mathbf{\Omega}_2))}} \quad (\text{Equation A.21})$$

We can also rewrite those same terms thanks to the same Hermitian property.

$$= \frac{|X^*(\mathbf{\Omega}_1 + \mathbf{\Omega}_2)| e^{j\phi(Y^*(\mathbf{\Omega}_1 + \mathbf{\Omega}_2))}}{|Y^*(\mathbf{\Omega}_1 + \mathbf{\Omega}_2)| e^{j\phi(X^*(\mathbf{\Omega}_1 + \mathbf{\Omega}_2))}} \quad (\text{Equation A.22})$$

Simple complex properties are $|X| = |X^*|$ and $\phi(X) = -\phi(X^*)$, which give us:

$$= \frac{|X(\mathbf{\Omega}_1 + \mathbf{\Omega}_2)| e^{j\phi(X(\mathbf{\Omega}_1 + \mathbf{\Omega}_2))}}{|Y(\mathbf{\Omega}_1 + \mathbf{\Omega}_2)| e^{j\phi(Y(\mathbf{\Omega}_1 + \mathbf{\Omega}_2))}} \quad (\text{Equation A.23})$$

Next, we return from the amplitude and phase notation to the complex functions themselves:

$$= \frac{X(\mathbf{\Omega}_1 + \mathbf{\Omega}_2)}{Y(\mathbf{\Omega}_1 + \mathbf{\Omega}_2)} \quad (\text{Equation A.24})$$

Now we define $H(\mathbf{\Omega}) = \frac{X(\mathbf{\Omega})}{Y(\mathbf{\Omega})}$ so we can rewrite Equation A.24 as

$$H(\mathbf{\Omega}_1)H(\mathbf{\Omega}_2) = H(\mathbf{\Omega}_1 + \mathbf{\Omega}_2) \quad (\text{Equation A.25})$$

Therefore, by a basic result of complex analysis $H(\mathbf{\Omega}) = e^{j\mathbf{k} \cdot \mathbf{\Omega}}$, and thus

$$Y(\mathbf{\Omega}) = X(\mathbf{\Omega}) e^{j\mathbf{k} \cdot \mathbf{\Omega}} \quad (\text{Equation A.26})$$

This holds in a region near the origin, and another property of characteristic functions is that, if their probability distribution has finite support, the probability distribution is uniquely determined by the value of the characteristic function in a region of the origin. Thus, in the spatiotemporal domain,

$$\mathbf{y}(\mathbf{s}) = \mathbf{x}(\mathbf{s} + \mathbf{a}) \text{ with vector of constants } \mathbf{a} \quad (\text{Equation A.27})$$

A.2.4 Computing the triple correlation

For computational applications presented here, we consider third-order correlation analysis applied to a discrete raster with neuron rows n , $1:N$, and time columns t , $1:T$, where each pixel $r(n, t)$ is filled with a 0 (white for no activity) or 1 (black for spike). The complete triple correlation function, while formally requisite, incurs substantial computational cost while

adding increasingly noisy information. We limit our computation to lag windows $-W_t:W_t$ and $-W_n:W_n$ chosen such that two local synaptic connections could not take longer than W_t , and two neurons are unlikely to be connected further than W_n . With this restricted lag window, we do not zero pad our raster (as in Yellot and Iverson, 1992) but instead use boundary conditions periodic in space (since our spatial ordering was already arbitrary) and restrict our calculation to a subset of time such that no motifs extend beyond time zero or the raster’s duration. In this case, discrete equivalent cd_3 of the triple correlation expression c_3 (Equation A.1) or the short form reported in the main text, $c_3(n_1, t_1, n_2, t_2) = \langle r(n, t)r(n + n_1, t + t_1)r(n + n_2, t + t_2) \rangle_{n,t}$, is

$$cd_3(n_1, t_1, n_2, t_2) = \frac{1}{\#(W_n, W_t, N, T)} \sum_{t=1+W_t}^{T-W_t} \sum_{n=1}^N r(n, t)r((n + n_1 - 1)\%N + 1, t + t_1)r((n + n_2 - 1)\%N + 1, t + t_2)$$

(Equations A.28-29)

We scale by the number of spike bins in the summation:

$$\#(W_n, W_t, N, T) = (T - 2W_t)(N) \quad \text{(Equation A.30)}$$

Equations A.28 and A.30 were used in all our simulations.

Note that in the text we report triple correlations “using lags up to X in time and space.” This corresponds to $W_n = X/2$ and $W_t = X/2$. When X is odd, we use the more general lag windows $-\text{floor}(X/2):\text{ceil}(X/2)$, with corresponding changes to the summation bounds and scaling instead by $(T - X)(N)$. We report the maximum lag as X because, e.g., $cd_3(-10, t_1, 10, t_2)$ has a maximum temporal separation between spikes of 20, despite the fact that technically the lag arguments are at most 10.

A.2.5 Summarizing triple correlation into motif classes

We summarized the triple correlation as fourteen motif-classes (Fig. 3.1). The main text discusses the reasoning for this particular choice, and here we describe the details.

Let $[n_1, t_1 | n_2, t_2]$ denote a motif, i.e. an argument to triple correlation, which would have a value $c_3(n_1, t_1, n_2, t_2)$. We want to group together these motifs according to what we can qualitatively distinguish. We only hold two qualitative distinctions:

1. temporal: we distinguish between before, simultaneous, and after (temporal coordinate less than, equal to, or greater)
2. spatial: we distinguish between the same and different (spatial coordinate equal and spatial coordinate not equal)

We will interpret the motif as a three-node graph: one base node implicitly $(0,0)$, and two other nodes, (n_1, t_1) and (n_2, t_2) . Note that neither of our qualitative distinctions involves node identity. So, for example, we would not distinguish between $[0,1|0,2]$ and $[0,2|0,1]$, even though one the first node follows the second, and in the other the reverse is true. In both, the motif includes nodes at the same spatial coordinate in sequence, so we do not distinguish between them.

By grouping motifs that are indistinguishable under these criteria, we develop motif classes. We enumerate these motif classes in Table A.1. From that enumeration, it is clear that no motif can belong to two motif classes. To show that this enumeration is complete (there are no more motif classes and all motifs fall into one of these classes), we count the number of motif classes below. To begin, we count “lag-sign” motifs, which is to say, if we only care about the sign of the lags, how many motifs are there. This first step avoids some of the small complications in our

definition, i.e. the different treatments of space and time, as well as the subtle ways they interact when we discard node identity. Having counted lag-sign motifs, we then reduce these lag-sign motifs by discounting spatial direction and node identity to finally arrive at the number of motif classes.

A.2.6 The number of lag-sign motifs

Given that three node combinations determine c_3 , we want to know how many ways there are to order them in time and space, with the caveat that we may also place one node on top of another in either time, or space, or both (to account for zero lag). To count this, we divide the cases according to how many different temporal and spatial bins the nodes have between them. For example, if all the nodes are completely distinct in time and space, then there are both three spatial bins and three temporal bins between the three nodes. On the other hand, if we overlap all three nodes in both time and space, then there is only one spatial bin and one temporal bin between them. All the cases are labeled in Table A1. Note that the cases are symmetric, so we will calculate the values as if in the lower left half of the table, i.e. where the number of spatial bins is greater than or equal to the number of time bins. The arrangement of this table is the same as in Figure 3.1C. As described above, we call this arrangement of nodes separated by lags a motif. When we only note the sign of the lags, we call it a lag-sign motif.

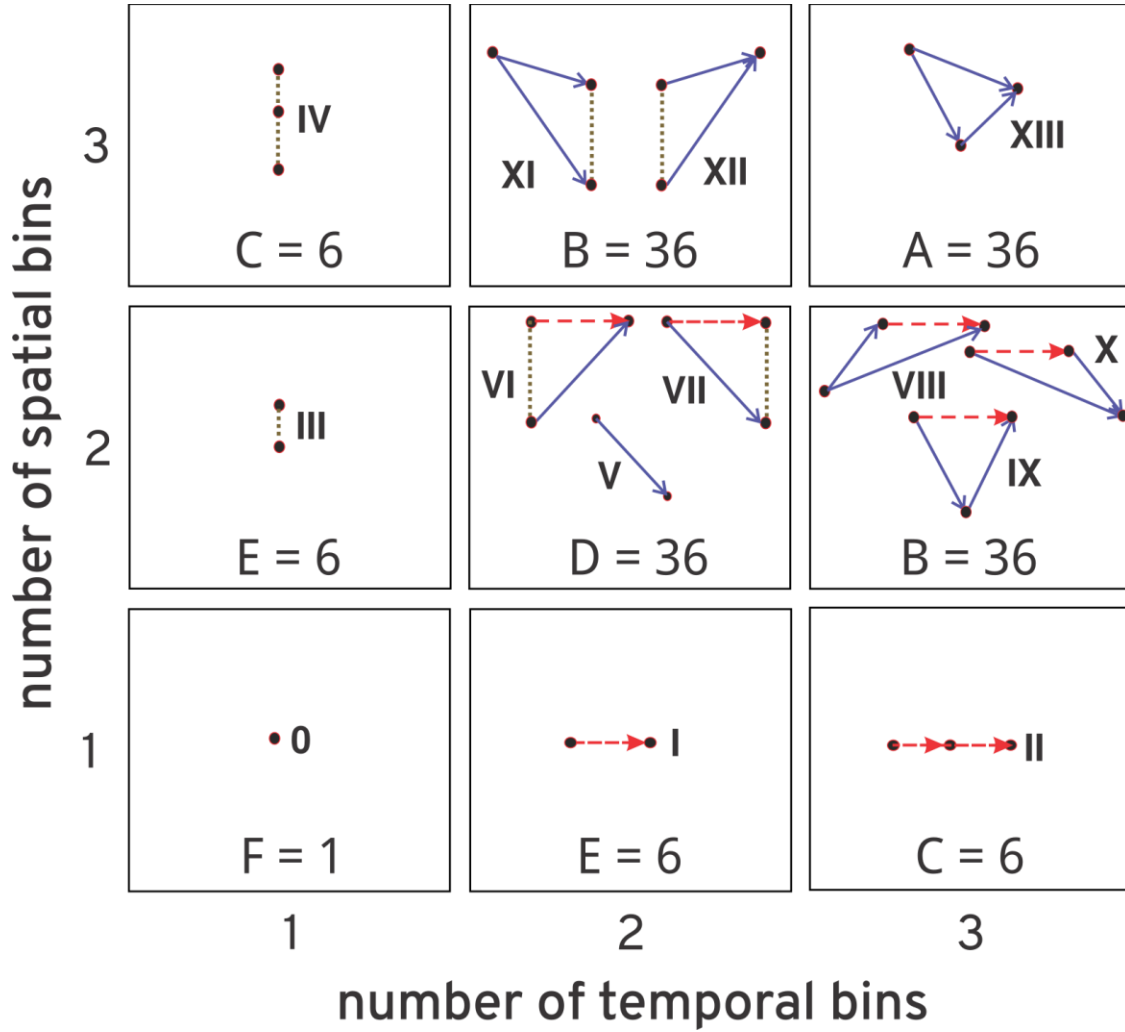
1. In the case where no nodes share a spatial bin (neuron), there are $3!$ ways to order them in space. Similarly if the nodes share no time bins, then there are $3!$ ways to order the time bins. So, if no spatial bins nor time bins are shared, then there are $3! 3! = 36$ orderings.
2. Given that the nodes only have two distinct spatial bins between them, there are three ways to choose which nodes share the same spatial bin, and then two ways to choose whether the remaining node has a spatial bin before or after the identical nodes' spatial bin, for $3 \cdot 2 = 6$

spatial orderings. As above, if no time bins are identical, then there are $3!$ temporal orderings. So there are $3 \cdot 2 \cdot 3! = 36$ orderings.

3. If nodes share the same spatial bin, then there is only one way to order that neuron. As above, if no time bins are identical then there are $3!$ temporal orderings, giving a total of $1 \cdot 3! = 6$ orderings. The same is true in the symmetric case when the nodes share the same time bin, but all have different neurons.
4. We already established that for the case where two spatial bins are the same, there are $3 \cdot 2 = 6$ orderings. The same is true when the nodes only have two distinct time bins. So there are $3 \cdot 2 \cdot 3 \cdot 2 = 36$ orderings.
5. We already established that for the case where two spatial bins are the same, there are $3 \cdot 2 = 6$ orderings, and for the case where all time bins are the same, there is only one ordering. So there are $3 \cdot 2 \cdot 1 = 6$ orderings.
6. In the case where all spatial bins and all time bins are the same, there is only one ordering.

We sum up the table: $A + 2B + 2C + D + 2E + F = 36 + 2 \cdot 36 + 2 \cdot 6 + 36 + 2 \cdot 6 + 1 = 169$ lag-sign motifs.

Table A.1: Counting the number of lag-sign motifs per motif class. The number of possible orderings in space and time given two possible time lags and two possible spatial lags, which corresponds to up to three possible bins in both time and space. Note that in case of a spike raster of single unit activity, each spatial bin corresponds to one neuron. This table corresponds to Fig. 3.1C.



A.2.7 The number of motif classes

To complete our summary, we reduce the 169 lag-sign motifs listed in Table A.2 by appealing to two symmetries: one in space, and one in permutation. The spatial one is straightforward: since we have not assigned meaning to space, reordering the spatial bins does not change our interpretation. The permutation symmetry is more technical: the way triple correlation is calculated, the ordering of the nodes matters. In second-order correlation (call it ρ),

this is even symmetry: $\rho(x) = \rho(-x)$. More generally, a motif has some polygonal structure (or possibly a point or a line; treat these as straightforward special cases of the following argument). Each vertex of the polygon has a node identity: in the triple correlation case, one is the base node, one is the first node, given by the base node plus (n_1, t_1) , and one is the second node, given by the base node plus (n_2, t_2) . But we don't actually care which is the base, which is the first, and which is the second node: triple correlation is invariant under permutation of these nodes. We reduce the number of lag-sign motifs by accounting for these symmetries. Again working from Table A.1:

- There are $3!$ ways to permute node identity, and $3!$ ways to permute neuron identity, independently, giving a product of 36 permutations. So all 36 lag-sign motifs in category A reduce to 1 motif class (Fig. 3.1C, XIII).
- For category B with two time bins, there are $3!$ node permutations, and only 3 spatial permutations: two spatial bins share a time bin, and the third spatial bin may appear above, between, or below these two spatial bins (due to the fact that we are reducing from lag-sign motifs, not from lag-motifs). The product is 18 total permutations, so the 36 lag-sign motifs in category B reduce to 2 motif classes (Fig. 3.1C, XI and XII).
- For category B with two spatial bins, there are only two spatial permutations: one spatial bin has two time bins, and the remaining spatial bin can either be above or below. There are still $3!$ node permutations, leading to a total of 12 permutations. Therefore, the 36 lag-sign motifs in category B reduce to 3 motif classes (Fig. 3.1C, VIII, IX, and X).
- By the same argument as in B, there are two spatial permutations, and again $3!$ node permutations, leading to a total of 12 permutations. Therefore the 36 lag-sign motifs in category D reduce to 3 motif classes (Fig. 3.1C, V, VI, and VII).

- When there is only one time bin, spatial permutation is the same as node permutation, so there are only the $3! = 6$ permutations. Therefore the 6 lag-sign motifs in category C(1T) reduce to 1 motif class (Fig. 3.1C, IV).
- As in C, all 6 reduce to 1 motif class (Fig. 3.1C, III).
- When there is only one spatial bin, the lag-sign motifs have no spatial permutations, only node permutations, so the 6 lag-sign motifs in category C reduce to 1 motif class (Fig. 3.1C, II).
- As in C, all 6 reduce to 1 motif class (Fig. 3.1C, I)
- In the case where all lags are zero, triple correlation has no symmetric entries but the zero entry, so there are no permutations, and the 1 lag-sign motif (which also contains only one lag-motif) remains 1 motif class (Fig. 3.1C, 0).

The above sum to 14 motif classes, as depicted in Figure A.1.

A.2.8 Expected contributions per motif class

Because it is important to assess how these motif-class contributions be explained by chance (or not), we simulate 100 activity matched noise rasters for each raster under investigation, and compare the raster's motif-class spectrum with that of its noise matched rasters. In the following, we derive the theoretical expectations for rasters governed by noise.

Let r be a raster with N neurons and T time bins. In a binary raster, a spike is indicated by $r(n, t) = 1$, else $r(n, t) = 0$. We calculate the triple correlation c_3 over the whole raster with periodic boundary conditions (i.e. $r(n + \eta, t + \tau) = r((n + \eta) \bmod N, (t + \tau) \bmod T)$, with an additional 1 offset). Define $\pi(\mathbf{x}, \boldsymbol{\lambda}) = r(\mathbf{x})r(\mathbf{x} + \boldsymbol{\lambda}_1)r(\mathbf{x} + \boldsymbol{\lambda}_2)$ and for shorthand $\pi(\boldsymbol{\lambda}) = \pi(0, \boldsymbol{\lambda})$. In general with lags $\boldsymbol{\lambda} = (\eta_1, \tau_1, \eta_2, \tau_2)$

$$\begin{aligned}
c_3(\boldsymbol{\lambda}) &= c_3(\eta_1, \tau_1, \eta_2, \tau_2) \\
&= \sum_{(n,t) \in I(r)} r(n,t) r(n + \eta_1, t + \tau_1) r(n + \eta_2, t + \tau_2) \\
&= \sum_{\mathbf{x} \in I(r)} \pi(\mathbf{x}, \boldsymbol{\lambda})
\end{aligned}$$

where $I(r)$ is the set of all indices of r , in this case $I(r) = (1:N) \times (1:T)$. We are interested in the motif class contributions, which are the sums of triple correlations for lags that constitute each of the fourteen motifs. So, if $\boldsymbol{\lambda} \in \Delta(M_i)$ denotes that the lags $\boldsymbol{\lambda}$ constitute a triplet in motif class i , then we define the motif class contribution as

$$M_i(r) = \sum_{\boldsymbol{\lambda} \in \Delta(M_i)} c_3(\boldsymbol{\lambda})$$

The expectation then is given by

$$\begin{aligned}
\langle M_i(r) \rangle &= \left\langle \sum_{\boldsymbol{\lambda} \in \Delta(M_i)} c_3(\boldsymbol{\lambda}) \right\rangle \\
&= \left\langle \sum_{\boldsymbol{\lambda} \in \Delta(M_i)} \sum_{\mathbf{x} \in I(r)} \pi(\mathbf{x}, \boldsymbol{\lambda}) \right\rangle \\
&= \sum_{\boldsymbol{\lambda} \in \Delta(M_i)} \sum_{\mathbf{x} \in I(r)} \langle \pi(\mathbf{x}, \boldsymbol{\lambda}) \rangle \\
&= \sum_{\mathbf{x} \in I(r)} \sum_{\boldsymbol{\lambda} \in \Delta(M_i)} \langle \pi(\mathbf{x}, \boldsymbol{\lambda}) \rangle \\
&= NT \sum_{\boldsymbol{\lambda} \in \Delta(M_i)} \langle \pi(\boldsymbol{\lambda}) \rangle
\end{aligned}$$

In fact, $\langle \pi(\boldsymbol{\lambda}) \rangle$ is constant for all $\boldsymbol{\lambda} \in \Delta(M_i)$ for a given i , so

$$\langle M_i(r) \rangle = NT \#(\Delta(M_i)) \langle \pi(\lambda_i) \rangle.$$

We can easily calculate $\langle \pi(\boldsymbol{\lambda}) \rangle$ if we assume independent bins. See below for the calculation in each of the cases of independent Bernoullis.

$\#(\Delta(M_i))$ is the more challenging problem, which we calculate case-by-case below in the section “The number of triplet motifs.”

A.2.9 Independent spiking with constant probability (Bernoulli)

For a simple spiking raster, we assume all bins have independent probability p of spiking, i.e. they are all independent Bernoullis, which also indicates that all the neurons are simulated Poisson processes with identical rates.

This lets us substitute the following probabilities

$$\begin{aligned}\langle \pi(\lambda_0) \rangle &= p \\ \langle \pi(\lambda_i) \rangle &= p^2 && \text{for } i = I, III, V \\ \langle \pi(\lambda_i) \rangle &= p^3 && \text{for } i = II, IV, VI, VII, VIII, IX, X, XI, XII, XIII\end{aligned}$$

where λ_i is a representative triplet of motif class i . This representative is sufficient because the expectation of the product of bins purely depends on the number of distinct bins multiplied. Within a motif class, all triplets have the same number of distinct bins, with motif class 0 having only one spike, motif classes I, III , and IV having two spikes, and the remaining motif classes having three spikes. Knowing these values, we have the expectations of each motif class.

A.2.10 The number of triplet motifs

The quantity $\#(\Delta(M_i))$ simply counts the number of motifs in a given motif class. This is independent of the data’s distribution, but dependent on the data’s shape. Let Λ_t be the number of time lags considered and let Λ_t^\pm , Λ_t^+ , and Λ_t^- be the number of time lags that are nonzero, positive, and negative respectively. Similarly define Λ_n , Λ_n^\pm , Λ_n^+ , and Λ_n^- .

Our first step for each motif class will be to define $\Delta(M_i)$, for which purpose we will define a notation to indicate the sign and equality of each part of the two spatiotemporal lags (the third lag implicitly zero). For example, in the case of motif class XIII, we write $\Delta(M_{XIII}) =$

$[x^\pm, t^\pm | y^\pm, s^\pm]$. This indicates that all four lags are nonzero (\pm superscript) and none are equal ($x \neq y$ and $t \neq s$). In contrast, we could write $[0, t^+ | 0, t^+]$ to indicate both spatial lags are zero, and the temporal lags are both positive and equal. We add a coefficient “2” to indicate that we want to additionally include set of lags symmetric with the notated lag, i.e. flipping which lag is first and which is second, e.g. $2[0,0 | 0, t^\pm] = [0,0 | 0, t^\pm] + [0, t^\pm | 0,0]$.

- I. Motif class I consists in lags $\Delta(M_I) = 2[0,0 | 0, t^\pm] + [0, t^\pm | 0, t^\pm]$. We count these as follows: there is only one way to choose the $(0,0)$ lag, and Λ_t^\pm ways to choose a $(0, t^\pm)$ lag. Therefore there are $1 \cdot \Lambda_t^\pm$ lags in $[0,0 | 0, t^\pm]$. By symmetry there are the same number in $[0, t^\pm | 0,0]$, so the coefficient 2 works as advertised, giving $2\Lambda_t^\pm$ lags in $2[0, t^\pm | 0,0]$. For the second addend, there are Λ_t^\pm ways to choose the $(0, t^\pm)$ lag. Since the lags are equal there is only one choice for the second lag, leading to a Λ_t^\pm lags in $[0t^\pm | 0t^\pm]$. In total then, there are $3\Lambda_t^\pm$ lags in $\Delta(M_I) = 2[0,0 | 0, t^\pm] + [0t^\pm | 0t^\pm]$. We write this

$$\begin{aligned} \#(\Delta(M_I)) &= \#(2[0,0 | 0, t^\pm] + [0t^\pm | 0t^\pm]) \\ &= 2(1 \cdot \Lambda_t^\pm) + (\Lambda_t^\pm \cdot 1) \\ &= 3\Lambda_t^\pm \end{aligned}$$

- II. For motif class II, we have $\Delta(M_{II}) = [0, t^\pm | 0, s^\pm]$. This time for our second lag, we have one fewer choice because we must have that the temporal lags do not equal. So we find

$$\begin{aligned} \#(\Delta(M_{II})) &= \#([0, t^\pm | 0, s^\pm]) \\ &= \Lambda_t^\pm (\Lambda_t^\pm - 1) \end{aligned}$$

- III. For motif class III, the situation is the same as motif class I, but with n rather than t , so $\Delta(M_{III}) = 2[0,0 | x^\pm, 0] + [x^\pm, 0 | x^\pm, 0]$, giving

$$\begin{aligned}
\#(\Delta(M_{III})) &= \#(2[0,0 \mid x^\pm, 0] + [x^\pm, 0 \mid x^\pm, 0]) \\
&= 2(1 \cdot \Lambda_n^\pm) + (\Lambda_n^\pm \cdot 1) \\
&= 3\Lambda_n^\pm
\end{aligned}$$

IV. Similarly motif class IV has $\#(\Delta(M_{III})) = \Lambda_n^\pm(\Lambda_n^\pm - 1)$.

V.

$$\begin{aligned}
\Delta(M_V) &= 2[0,0 \mid x^\pm, t^\pm] + [x^\pm, t^\pm \mid x^\pm, t^\pm] \\
\#(\Delta(M_V)) &= 2\Lambda_n^\pm \Lambda_t^\pm + \Lambda_n^\pm \Lambda_t^\pm \\
&= 3\Lambda_n^\pm \Lambda_t^\pm
\end{aligned}$$

VI.

$$\begin{aligned}
\Delta(M_{VI}) &= 2[0, t^+ \mid x^\pm, 0] + 2[x^\pm, 0 \mid x^\pm t^+] + 2[0, t^- \mid x^\pm t^-] \\
\#(\Delta(M_{VI})) &= 2(\Lambda_t^+ \Lambda_n^\pm) + 2(\Lambda_n^\pm \Lambda_t^+) = 2(\Lambda_t^- \Lambda_n^\pm) \\
&= 4(\Lambda_n^\pm \Lambda_t^+) + 2(\Lambda_n^\pm \Lambda_t^-)
\end{aligned}$$

VII. By symmetry with VI,

$$\#(\Delta(M_{VII})) = 4(\Lambda_n^\pm \Lambda_t^-) + 2(\Lambda_n^\pm \Lambda_t^+)$$

VIII.

$$\begin{aligned}
\Delta(M_{VIII}) &= [x^\pm, t^+ \mid x^\pm, s^+] + 2[x^\pm, t^- \mid 0, s^+] + 2[x^\pm, t^- \mid 0, s^-(> t^-)] \\
\#(\Delta(M_{VIII})) &= \Lambda_n^\pm \Lambda_t^+ (\Lambda_t^+ - 1) + 2\Lambda_n^\pm \Lambda_t^- \Lambda_t^+ + 2\Lambda_n^\pm \sum_{\Lambda_t^- < t^- < -1} \#s: t^- < s < 0 \\
&= \Lambda_n^\pm \Lambda_t^+ (\Lambda_t^+ - 1) + 2\Lambda_n^\pm \Lambda_t^- \Lambda_t^+ + 2\Lambda_n^\pm \sum_{-\Lambda_t^- < t^- < -1} |t^-| - 1 \\
&= \Lambda_n^\pm \Lambda_t^+ (\Lambda_t^+ - 1) + 2\Lambda_n^\pm \Lambda_t^- \Lambda_t^+ + 2\Lambda_n^\pm \sum_{(-\Lambda_t^- - 1) > t > 1} t \\
&= \Lambda_n^\pm \Lambda_t^+ (\Lambda_t^+ - 1) + 2\Lambda_n^\pm \Lambda_t^- \Lambda_t^+ + 2\Lambda_n^\pm (\Lambda_t^- - 1) \frac{(\Lambda_t^- - 1) + 1}{2} \\
&= \Lambda_n^\pm \Lambda_t^+ (\Lambda_t^+ - 1) + 2\Lambda_n^\pm \Lambda_t^- \Lambda_t^+ + \Lambda_n^\pm \Lambda_t^- (\Lambda_t^- - 1)
\end{aligned}$$

IX.

$$\begin{aligned}
\Delta(M_{IX}) &= 2[0, t^+ | x^\pm, s^+ < t^+] + 2[0, t^- | x^\pm, s^- > t^-] + 2[x^\pm, t^- | x^\pm, s^+] \\
\#(\Delta(M_{IX})) &= 2\Lambda_n^\pm \sum_{1 \leq t \leq \Lambda_t^+} (t-1) + 2\Lambda_n^\pm \sum_{-\Lambda_t^- \leq t \leq -1} (|t|-1) + 2\Lambda_n^\pm \Lambda_t^- \Lambda_t^+ \\
&= 2\Lambda_n^\pm \left(\Lambda_t^+ \frac{(\Lambda_t^+ - 1) + 0}{2} \right) + 2\Lambda_n^\pm \left(\Lambda_t^- \frac{(\Lambda_t^- - 1) + 0}{2} \right) + 2\Lambda_n^\pm \Lambda_t^- \Lambda_t^+ \\
&= \Lambda_n^\pm \Lambda_t^+ (\Lambda_t^+ - 1) + \Lambda_n^\pm \Lambda_t^- (\Lambda_t^- - 1) + 2\Lambda_n^\pm \Lambda_t^- \Lambda_t^+
\end{aligned}$$

X. By symmetry with VIII

$$\begin{aligned}
\Delta(M_X) &= [x^\pm, t^- | x^\pm, s^-] + 2[x^\pm, t^+ | 0, s^-] + 2[x^\pm, t^+ | 0, s^+ (< t^+)] \\
\#(\Delta(M_X)) &= \Lambda_n^\pm \Lambda_t^- (\Lambda_t^- - 1) + 2\Lambda_n^\pm \Lambda_t^+ \Lambda_t^- + \Lambda_n^\pm \Lambda_t^+ (\Lambda_t^+ - 1)
\end{aligned}$$

XI.

$$\begin{aligned}
\Delta(M_{XI}) &= [x^\pm, t^+ | y^\pm, t^+] + 2[x^\pm, 0 | y^\pm, t^-] \\
\#(\Delta(M_{XI})) &= \Lambda_n^\pm (\Lambda_n^\pm - 1) \Lambda_t^+ + 2\Lambda_n^\pm (\Lambda_n^\pm - 1) \Lambda_t^-
\end{aligned}$$

XII.

$$\begin{aligned}
\Delta(M_{XII}) &= [x^\pm, t^- | y^\pm, t^-] + 2[x^\pm, 0 | y^\pm, t^+] \\
\#(\Delta(M_{XII})) &= \Lambda_n^\pm (\Lambda_n^\pm - 1) \Lambda_t^- + 2\Lambda_n^\pm (\Lambda_n^\pm - 1) \Lambda_t^+
\end{aligned}$$

XIII.

$$\begin{aligned}
\Delta(M_{XIII}) &= [x^\pm, t^\pm | y^\pm, s^\pm] \\
\#(\Delta(M_{XIII})) &= \Lambda_n^\pm \Lambda_t^\pm (\Lambda_n^\pm - 1) (\Lambda_t^\pm - 1)
\end{aligned}$$

Table A.2: The 169 possible lag-sign motifs. In the triple correlation equation, there are four lags that can be either zero or non-zero. Accordingly, the rows in this table are ordered in 16 (2^4) groups while the subgroups within these groups, represent the arrangement of the non-zero lags. The total number of rows is 169 lag-sign motifs for three-node motifs with distinct lag signs. Each row represents a single three-node lag-sign motif, which are differentiated by the spike sequencing. The base node implicitly has lags $n_0 = 0$ and $t_0 = 0$, and the four lags of the other two nodes (n_1, n_2, t_1, t_2) are those in Equation 3.1. In the lag columns, '0' entries denote that the lag is zero while '+' entries denote a positive value, and '-' entries denote a negative value (respectively greater or less relative to the base node's spatiotemporal position). Note that in case where one modality (space or time) shares the same (non-zero) sign, we need additional constraints to specify the spike sequence, given by the column "Constraints." The 14 motif classes are labelled by Roman numerals in the third column group, "Motif Class". The "Configuration" column illustrates a representative schematic of the lag-motif, where the solid dot, small open circle, and large open circle indicate the base, second, and third nodes, respectively.






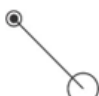




Lag-Sign Motif	n_1	t_1	n_2	t_2	Constraints	Motif Class	Configuration
0	0	0	0	0		0	
1.0	0	0	0	+		I	
1.1	0	0	0	-		I	
2.0	0	0	+	0		III	
2.1	0	0	-	0		III	
3.0	0	0	+	+		V	
3.1	0	0	+	-		V	
3.2	0	0	-	+		V	
3.3	0	0	-	-		V	
4.0	0	+	0	0		I	

Table A.2 continued:









4.1	0	-	0	0		I	
5.0.0	0	+	0	+	$ t_1 = t_2 $	I	
5.0.1	0	+	0	+	$ t_1 > t_2 $	II	
5.0.2	0	+	0	+	$ t_1 < t_2 $	II	
5.1	0	+	0	-		II	
5.2	0	-	0	+		II	
5.3.0	0	-	0	-	$ t_1 = t_2 $	I	
5.3.1	0	-	0	-	$ t_1 > t_2 $	II	

Table A.2 continued:


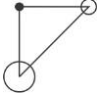
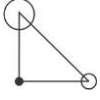
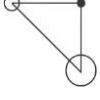
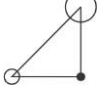
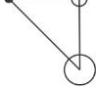



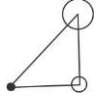
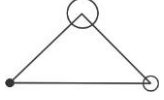
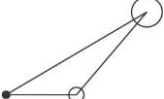
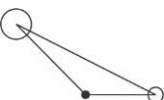
5.3.2	0	-	0	-	$ t_1 < t_2 $	II	
6.0	0	+	+	0		VI	
6.1	0	+	-	0		VI	
6.2	0	-	+	0		VII	
6.3	0	-	-	0		VII	
7.0.0	0	+	+	+	$ t_1 = t_2 $	VII	
7.0.1	0	+	+	+	$ t_1 > t_2 $	IX	
7.0.2	0	+	+	+	$ t_1 < t_2 $	X	
7.1	0	+	+	-		VIII	
7.2.0	0	+	-	+	$ t_1 = t_2 $	VII	
7.2.1	0	+	-	+	$ t_1 > t_2 $	IX	
7.2.2	0	+	-	+	$ t_1 < t_2 $	X	
7.3	0	+	-	-		VIII	

Table A.2 continued:



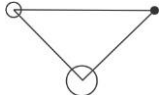
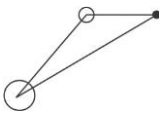
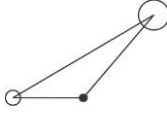
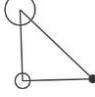
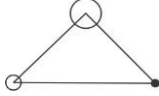
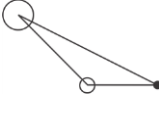


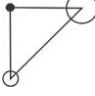
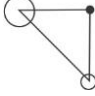
7.4	0	-	+	+		X	
7.5.0	0	-	+	-	$ t_1 = t_2 $	VI	
7.5.1	0	-	+	-	$ t_1 > t_2 $	IX	
7.5.2	0	-	+	-	$ t_1 < t_2 $	VIII	
7.6	0	-	-	+		X	
7.7.0	0	-	-	-	$ t_1 = t_2 $	VI	
7.7.1	0	-	-	-	$ t_1 > t_2 $	IX	
7.7.2	0	-	-	-	$ t_1 < t_2 $	VIII	
8.0	+	0	0	0		III	
8.1	-	0	0	0		III	
9.0	+	0	0	+		VI	
9.1	+	0	0	-		VII	

Table A.2 continued:

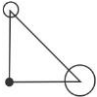
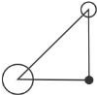







9.2	-	0	0	+		VI	
9.3	-	0	0	-		VII	
10.0.0	+	0	+	0	$ n_1 = n_2 $	III	
10.0.1	+	0	+	0	$ n_1 > n_2 $	IV	
10.0.2	+	0	+	0	$ n_1 < n_2 $	IV	
10.1	+	0	-	0		IV	
10.2	-	0	+	0		IV	
10.3.0	-	0	-	0	$ n_1 = n_2 $	III	
10.3.1	-	0	-	0	$ n_1 > n_2 $	IV	

Table A.2 continued:


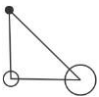

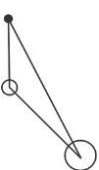
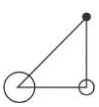
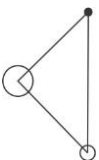
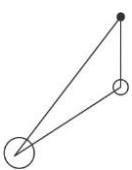


10.3.2	-	0	-	0	$ n_1 < n_2 $	IV	
11.0.0	+	0	+	+	$ n_1 = n_2 $	VI	
11.0.1	+	0	+	+	$ n_1 > n_2 $	XII	
11.0.2	+	0	+	+	$ n_1 < n_2 $	XII	
11.1.0	+	0	+	-	$ n_1 = n_2 $	VII	
11.1.1	+	0	+	-	$ n_1 > n_2 $	XI	
11.1.2	+	0	+	-	$ n_1 < n_2 $	XI	
11.2	+	0	-	+		XII	
11.3	+	0	-	-		XI	

Table A.2 continued:

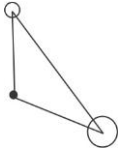

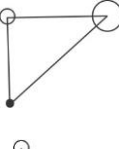
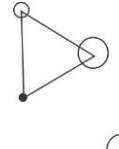

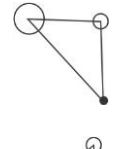
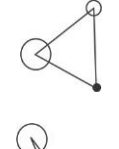
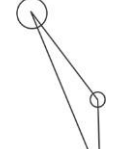


11.4	-	0	+	+		XII	
11.5	-	0	+	-		XI	
11.6.0	-	0	-	+	$ n_1 = n_2 $	VI	
11.6.1	-	0	-	+	$ n_1 > n_2 $	XII	
11.6.2	-	0	-	+	$ n_1 < n_2 $	XII	
11.7.0	-	0	-	-	$ n_1 = n_2 $	VII	
11.7.1	-	0	-	-	$ n_1 > n_2 $	XI	
11.7.2	-	0	-	-	$ n_1 < n_2 $	XI	
12.0	+	+	0	0		V	
12.1	+	-	0	0		V	

Table A.2 continued:

12.2	-	+	0	0		V	
12.3	-	-	0	0		V	
13.0.0	+	+	0	+	$ t_1 = t_2 $	VII	
13.0.1	+	+	0	+	$ t_1 > t_2 $	X	
13.0.2	+	+	0	+	$ t_1 < t_2 $	IX	
13.1	+	+	0	-		X	
13.2	+	-	0	+		VIII	
13.3.0	+	-	0	-	$ t_1 = t_2 $	VI	
13.3.1	+	-	0	-	$ t_1 > t_2 $	VIII	
13.3.2	+	-	0	-	$ t_1 < t_2 $	IX	
13.4.0	-	+	0	+	$ t_1 = t_2 $	VII	
13.4.1	-	+	0	+	$ t_1 > t_2 $	X	

Table A.2 continued:

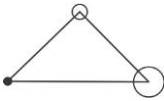
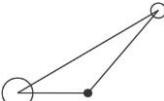



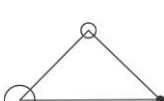
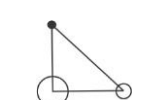


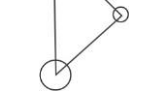
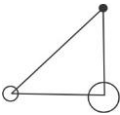
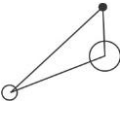
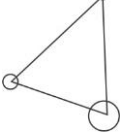


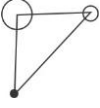
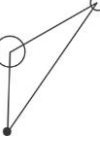
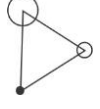

13.4.2	-	+	0	+	$ t_1 < t_2 $	IX	
13.5	-	+	0	-		X	
13.6	-	-	0	+		VIII	
13.7.0	-	-	0	-	$ t_1 = t_2 $	VI	
13.7.1	-	-	0	-	$ t_1 > t_2 $	VIII	
13.7.2	-	-	0	-	$ t_1 < t_2 $	IX	
14.0.0	+	+	+	0	$ n_1 = n_2 $	VI	
14.0.1	+	+	+	0	$ n_1 > n_2 $	XII	
14.0.2	+	+	+	0	$ n_1 < n_2 $	XII	
14.1	+	+	-	0		XII	

Table A.2 continued:

14.2.0	+	-	+	0	$ n_1 = n_2 $	VII	
14.2.1	+	-	+	0	$ n_1 > n_2 $	XI	
14.2.2	+	-	+	0	$ n_1 < n_2 $	XI	
14.3	+	-	-	0		XI	
14.4	-	+	+	0		XII	
14.5.0	-	+	-	0	$ n_1 = n_2 $	VI	
14.5.1	-	+	-	0	$ n_1 > n_2 $	XII	
14.5.2	-	+	-	0	$ n_1 < n_2 $	XII	
14.6	-	-	+	0		XI	

14.7.0	-	-	-	0	$ n_1 = n_2 $	VII	
14.7.1	-	-	-	0	$ n_1 > n_2 $	XI	
14.7.2	-	-	-	0	$ n_1 < n_2 $	XI	
15.0.0	+	+	+	+	$ n_1 = n_2 $ $ t_1 = t_2 $	V	
15.0.1	+	+	+	+	$ n_1 = n_2 $ $ t_1 > t_2 $	VIII	
15.0.2	+	+	+	+	$ n_1 = n_2 $ $ t_1 < t_2 $	VIII	
15.0.3	+	+	+	+	$ n_1 > n_2 $ $ t_1 = t_2 $	XI	
15.0.4	+	+	+	+	$ n_1 > n_2 $ $ t_1 > t_2 $	XIII	
15.0.5	+	+	+	+	$ n_1 > n_2 $ $ t_1 < t_2 $	XIII	
15.0.6	+	+	+	+	$ n_1 < n_2 $ $ t_1 = t_2 $	XI	

Table A.2 continued:

15.0.7	+	+	+	+	$ n_1 < n_2 $ $ t_1 > t_2 $	XIII	
15.0.8	+	+	+	+	$ n_1 < n_2 $ $ t_1 < t_2 $	XIII	
15.1.0	+	+	+	-	$ n_1 = n_2 $	IX	
15.1.1	+	+	+	-	$ n_1 > n_2 $	XIII	
15.1.2	+	+	+	-	$ n_1 < n_2 $	XIII	
15.2.0	+	+	-	+	$ t_1 = t_2 $	XI	
15.2.1	+	+	-	+	$ t_1 > t_2 $	XIII	
15.2.2	+	+	-	+	$ t_1 < t_2 $	XIII	
15.3	+	+	-	-		XIII	

Table A.2 continued:

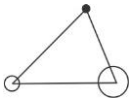
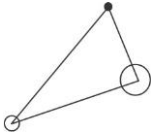


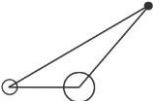
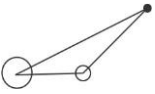
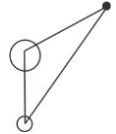

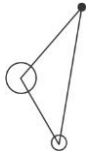
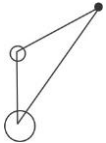
15.4.0	+	-	+	+	$ n_1 = n_2 $	IX	
15.4.1	+	-	+	+	$ n_1 > n_2 $	XIII	
15.4.2	+	-	+	+	$ n_1 < n_2 $	XIII	
15.5.0	+	-	+	-	$ n_1 = n_2 $ $ t_1 = t_2 $	V	
15.5.1	+	-	+	-	$ n_1 = n_2 $ $ t_1 > t_2 $	X	
15.5.2	+	-	+	-	$ n_1 = n_2 $ $ t_1 < t_2 $	X	
15.5.3	+	-	+	-	$ n_1 > n_2 $ $ t_1 = t_2 $	XII	
15.5.4	+	-	+	-	$ n_1 > n_2 $ $ t_1 > t_2 $	XIII	
15.5.5	+	-	+	-	$ n_1 > n_2 $ $ t_1 < t_2 $	XIII	
15.5.6	+	-	+	-	$ n_1 < n_2 $ $ t_1 = t_2 $	XII	

Table A.2 continued:

15.5.7	+	-	+	-	$ n_1 < n_2 $ $ t_1 > t_2 $	XIII	
15.5.8	+	-	+	-	$ n_1 < n_2 $ $ t_1 < t_2 $	XIII	
15.6	+	-	-	+		XIII	
15.7.0	+	-	-	-	$ t_1 = t_2 $	XII	
15.7.1	+	-	-	-	$ t_1 > t_2 $	XIII	
15.7.2	+	-	-	-	$ t_1 < t_2 $	XIII	
15.8.0	-	+	+	+	$ t_1 = t_2 $	XI	
15.8.1	-	+	+	+	$ t_1 > t_2 $	XIII	

Table A.2 continued:

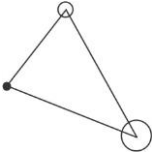
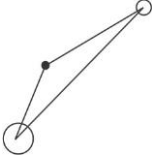


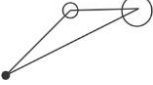
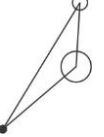
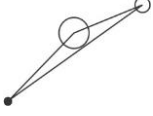
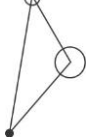

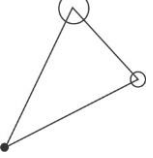



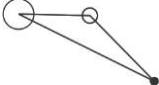
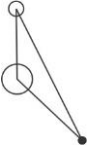

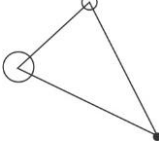
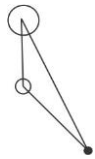
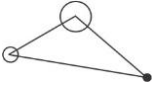
15.8.2	-	+	+	+	$ t_1 < t_2 $	XIII	
15.9	-	+	+	-		XIII	
15.10.0	-	+	-	+	$ n_1 = n_2 $ $ t_1 = t_2 $	V	
15.10.1	-	+	-	+	$ n_1 = n_2 $ $ t_1 > t_2 $	VIII	
15.10.2	-	+	-	+	$ n_1 = n_2 $ $ t_1 < t_2 $	VIII	
15.10.3	-	+	-	+	$ n_1 > n_2 $ $ t_1 = t_2 $	XI	
15.10.4	-	+	-	+	$ n_1 > n_2 $ $ t_1 > t_2 $	XIII	
15.10.5	-	+	-	+	$ n_1 > n_2 $ $ t_1 < t_2 $	XIII	
15.10.6	-	+	-	+	$ n_1 < n_2 $ $ t_1 = t_2 $	XI	
15.10.7	-	+	-	+	$ n_1 < n_2 $ $ t_1 > t_2 $	XIII	

Table A.2 continued:

15.10.8	-	+	-	+	$ n_1 < n_2 $ $ t_1 < t_2 $	XIII	
15.11.0	-	+	-	-	$ n_1 = n_2 $	IX	
15.11.1	-	+	-	-	$ n_1 > n_2 $	XIII	
15.11.2	-	+	-	-	$ n_1 < n_2 $	XIII	
15.12	-	-	+	+		XIII	
15.13.0	-	-	+	-	$ t_1 = t_2 $	XII	
15.13.1	-	-	+	-	$ t_1 > t_2 $	XIII	
15.13.2	-	-	+	-	$ t_1 < t_2 $	XIII	
15.14.0	-	-	-	+	$ n_1 = n_2 $	IX	
15.14.1	-	-	-	+	$ n_1 > n_2 $	XIII	

Table A.2 continued:

15.14.2	-	-	-	+	$ n_1 < n_2 $	XIII	
15.15.0	-	-	-	-	$ n_1 = n_2 $ $ t_1 = t_2 $	V	
15.15.1	-	-	-	-	$ n_1 = n_2 $ $ t_1 > t_2 $	X	
15.15.2	-	-	-	-	$ n_1 = n_2 $ $ t_1 < t_2 $	X	
15.15.3	-	-	-	-	$ n_1 > n_2 $ $ t_1 = t_2 $	XII	
15.15.4	-	-	-	-	$ n_1 > n_2 $ $ t_1 > t_2 $	XIII	
15.15.5	-	-	-	-	$ n_1 > n_2 $ $ t_1 < t_2 $	XIII	
15.15.6	-	-	-	-	$ n_1 < n_2 $ $ t_1 = t_2 $	XII	
15.15.7	-	-	-	-	$ n_1 < n_2 $ $ t_1 > t_2 $	XIII	
15.15.8	-	-	-	-	$ n_1 < n_2 $ $ t_1 < t_2 $	XIII	